# MINERAL DISSOLUTION IN SEDIMENTS

A Thesis
Presented to
The Academic Faculty

by

Minsu Cha

In Partial Fulfillment
of the Requirements for the Degree
Doctor of Philosophy in the
School of Civil and Environmental Engineering

Georgia Institute of Technology
December 2012

# MINERAL DISSOLUTION IN SEDIMENTS

Approved by:


Dr. J. Carlos Santamarina, Advisor
School of Civil and Environmental Engineering
*Georgia Institute of Technology*

Dr. Glenn J. Rix
School of Civil and Environmental Engineering
*Georgia Institute of Technology*

Dr. Susan E. Burns
School of Civil and Environmental Engineering
*Georgia Institute of Technology*

Dr. Christian Huber
School of Earth & Atmospheric Sciences
*Georgia Institute of Technology*

Dr. Paul W. Mayne
School of Civil and Environmental Engineering
*Georgia Institute of Technology*


Date Approved: July 27, 2012

To my parents

# ACKNOWLEDGEMENTS

I would like to express my sincere gratitude to my advisor, Dr. J. Carlos Santamarina, for his guidance, support, generosity, and patience. It was really fortunate to meet him and work with him. I am deeply impressed by his knowledge, endless curiosity, care, and philosophy of life. I would also like to acknowledge his family, especially, Cecilia for her generous support, and Francisco for thoroughly proofreading my thesis.

I want to thank the past and current members of the Particulate Media Research Laboratory for their help, discussions, and encouragement: Hosung Shin, Nicolas Espinoza, Jongwon Jung, Jaewon Jang, Changho Lee, Eunseok Bang, Cesar Pasten, Sheng Dai, Seunghee Kim, Junbong Jang, Song Hun Chong, Shahrzad Roshankhah, Marco Terzariol, Aswathy Sivaram, Efthymios Papadopoulos, and Xingwei Ren, Dr. Norimasa Yoshimoto, Dr. Andrea Mezencevova, and Dr. Cuiying Lu. I am indebted to the members of the GT Geosystems department for their help and being a part of my academic experience. I am grateful to Andrew Udell, Michael R. Sorenson, Mike Anderson and his ISG team for their excellent support.

I gratefully acknowledge my thesis committee members for their helpful comments and suggestions: Dr. Susan E. Burns, Dr. Paul W. Mayne, Dr. Glenn J. Rix, and Dr. Christian Huber. I appreciate Dr. J. David Frost for generously allowing me to use his software. I would like to thank Georgia Institute of Technology for providing a wonderful academic environment, and our sponsors: the Department of Energy Savannah River Operations Office and Dr. Brent J. Gutierrez, the National Science Foundation, and the Goizueta Foundation. I am also thankful to Dr. Gye-Chun Cho for the opportunities

during my Master's degree program and his continued advice, and the Civil Engineering faculty at KAIST and Pusan National University that have prepared me as a scholar.

Finally, I would like to thank my parents for their dedicated support, great trust, and unconditional love for me. They have taught me the virtue of hard work and sincerity through their lives. I also thank my sister and brother, and their families for their sincere guidance and support.

# TABLE OF CONTENTS

# LIST OF TABLES

Page

# LIST OF FIGURES

Page

# SUMMARY

Mineral dissolution is an inherent chemo-hydro-mechanical coupled diagenetic process in sediments. This ubiquitous geological phenomenon affects all properties in sediments, however, its engineering impact remains largely unknown. This research centers on the effects of mineral dissolution on sediment behavior with emphasis on dissolution modes in nature and their engineering implications.

Five different dissolution modes are identified: homogeneous, pressure-dependent, and localized dissolution, and the dissolution of shallow and deep dissolvable inclusions. The consequences of each dissolution mode are investigated through experiments and discrete element methods. While each dissolution mode triggers unique consequences, it is observed that in all cases 1) significant displacement takes places during dissolution, 2) there is a pronounced effect of internal friction and the extent of dissolution on the evolution of the sediment, 3) the sediment has higher compressibility and exhibits a more contractive tendency after dissolution, 4) a porous honeycomb-shaped internal fabric develops accompanied by contact force concentration along dissolved inclusions, and 5) horizontal stress reduction takes place during dissolution and shear localization may develop under zero lateral strain conditions.

Mineral dissolution has important engineering implications, from soil characterization to slope stability and shallow foundations. Pre- and post-dissolution CPT studies show that dissolution decreases the tip resistance proportional to the extent of dissolution. Dissolution in sloping ground induces global settlement as the prevailing deformation pattern, and prominent lateral movements near the slope surface; sudden

undrained shear failure may take place during otherwise quasi-static dissolution. While footings experience larger settlements during post-dissolution loading, subsequent dissolution beneath a previously loaded footing causes displacements that are greater than the sum of dissolution-induced and load-induced settlements.

# CHAPTER 1

# INTRODUCTION

Sediments experience mineral dissolution in most natural settings and engineered processes. Furthermore, there are often dissolution-like phenomena that affect ground behavior such as solifluction, organic matter decomposition, thawing, and gas hydrate dissociation.

The consequences of dissolution are often overlooked in geoengineering. However, an increasing body of evidence shows that dissolution can have a profound effect on the performance of engineered systems (including fly ash and mine tailing ponds), and geotechnical components in the field of energy geotechnology (such as nuclear waste repositories, $CO_2$ geostorage and methane hydrate). A thorough understanding of the consequences of mineral dissolution on sediment behavior and system response is needed.

This research investigates the effect of mineral dissolution on sediment behavior through combined laboratory experiments and particle-scale numerical simulations using the discrete element method DEM. The choice of the discrete element method highlights the inherently particle-scale nature of dissolution.

Chapter 2 investigates the sediment response during the dissolution of evenly distributed dissolvable grains, i.e., homogeneous dissolution. Post-dissolution $k_0$-loading and simple shear loading complete the study. Mineral dissolution is simulated by gradually reducing the size of randomly distributed soluble grains in a 3D packing of spherical particles.

Chapter 3 models pressure-dependent dissolution whereby every grain contracts proportionally to the force it carries. We monitor the evolution of the internal fabric,

equivalent horizontal stress and vertical displacement, and contact-level information during pressure solution at constant vertical stress and zero-lateral strain.

Chapter 4 explores localized dissolution, which may result from hydro-chemo-mechanical coupling, using experiments and complimentary numerical simulations. We observe dissolution localization in calcareous sands subjected to flow of a high acidity solution. The simulation using discrete elements is performed by placing the soluble grains along a pre-designated pipe geometry.

The effect of shallow dissolvable inclusions on the overlying sediments is studied in Chapter 5. The detailed analysis of DEM results shows correlation between the emergent contact force networks and the evolution in local porosity, the significance of the initial soil density and friction angle, and the governing effect of geometric considerations such as depth-to-inclusion size ratio.

Chapter 6 investigates the mechanical effect of dissolvable deep inclusions on the surrounding soil under a constant vertical stress condition. Variables include friction angle, soluble fraction in inclusions, and inclusion size. Both 2D and 3D simulation results show the evolution of deformation, contact force chains, displacements, and global stress ratio.

Chapter 7 reports results of an experimental program designed to investigate the effect of dissolution on penetration resistance in view of in situ characterization. Pre-dissolution and post-dissolution cone penetration tests were conducted with a laboratory-scale CPT device and a spring-loaded calibration chamber. Variables include the initial sediment density and the amount of soluble grains.

Chapter 8 explores the effect of mineral dissolution on slope stability, using DEM simulations complemented with an experimental validation phase. We observe the evolution of slope displacements, sediment fabric, and implications on global stability.

Chapter 9 explores the effect of gradual grain dissolution on the load-settlement response of shallow foundations. Study results include the footing load vs. settlement response on sediments that experience dissolution before or after loading.

Finally, Chapter 10 summarizes the main conclusions of this study.

# CHAPTER 2

# DISSOLUTION OF RANDOMLY DISTRIBUTED SOLUBLE GRAINS – POST DISSOLUTION $K_0$-LOADING AND SHEAR

## 2.1 Introduction

Mineral dissolution is a common, diagenetic process. Typically, the time scale is long and mineral dissolution is disregarded in most engineering designs. However, this may not be the case in minerals such as carbonates, or when acid fluids are injected in the ground. Furthermore, some engineering projects are designed for long times, such as nuclear waste disposal and $CO_2$ geostorage.

Particle-scale dissolution affects large- and small-strain properties: there are marked differences in fabric and a distinct "honeycomb fabric" emerges (Shin et al. 2008, Shin and Santamarina 2009), normalized vertical displacement and void ratio increase (Fam et al. 2002, Shin et al. 2008, Shin and Santamarina 2009, Truong et al. 2010), the value of $k_0$ decreases often to $k_a$ before it recovers (Shin and Santamarina 2009), shear wave velocity decreases and attenuation increases (Fam et al. 2002, Truong et al. 2010), and the peak friction angle decreases (Fam et al. 2002).

In this study, we investigate the behavior of coarse-grained sediments during dissolution, post-dissolution $k_0$-loading, and post-dissolution simple shear loading using the discrete element method in 3D. We note that there are various possible modes of dissolution; this study is relevant to evenly distributed dissolvable components (Note: other dissolution conditions are explored later in this Thesis).

## 2.2 Simulation Approach

We use the PFC-3D discrete element code for this simulation study (Cundall and Strack 1979). Dissolution is performed in a numerical cell with zero-lateral strain side-walls.

The packing of spherical particles with a uniformly distributed grain size distribution ($R_{min}$=1mm, $R_{max}$=1.5mm - Table 2.1) is formed by randomly placing smaller grains in the cube and gradually expanding them under zero gravity and zero interparticle friction to attain the target porosity of a sediment n≈0.38. Then, after turning on friction and gravity, the specimen is incrementally loaded in the vertical direction to 100 kPa under zero lateral strain conditions. Different soluble fractions SF (i.e., number of soluble particles with respect to the total number of particles) are simulated: SF= 0%, 2%, 5%, and 10%. The soluble particles are randomly distributed in the medium (See Figure 2.1). Basic model properties and the simulation environment are shown in Table 2.1.

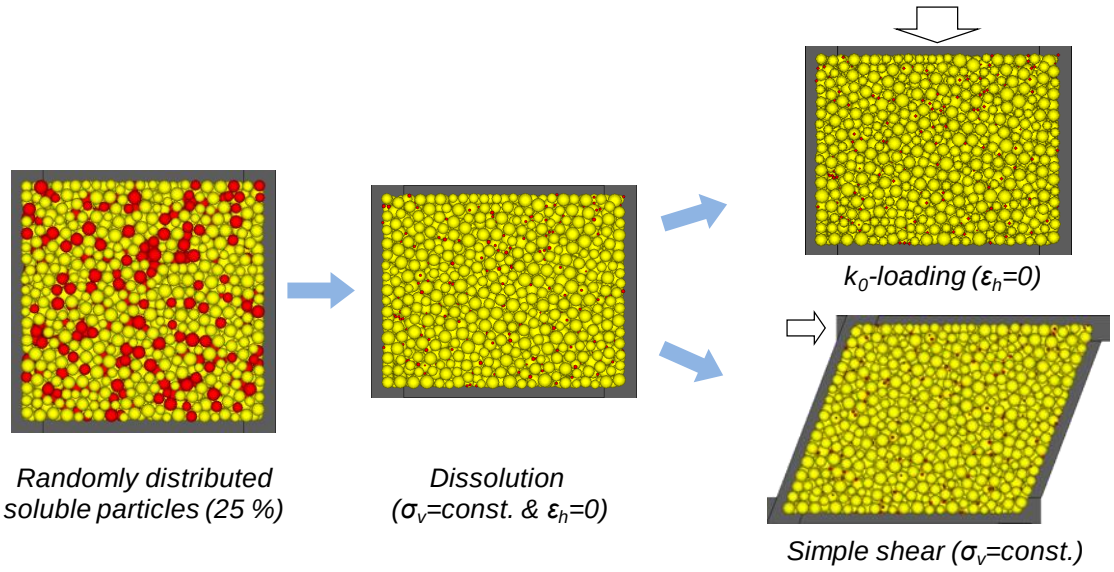


Figure 2.1 Simulation sequence in DEM 3D model (images shown for a soluble fraction SF=25%).

Table 2.1 Model properties and simulation environment

| | Properties | Values |
|---|---|---|
| Ball | Initial radius of balls | Uniform size distribution ($R_{min}$=1mm, $R_{max}$=1.5mm) |
| | Number of balls | 9167 |
| | Mass density of balls | 2650 kg/$m^3$ |
| | Hertzian contact model | Shear modulus = $2.9\times10^9$ Pa |
| | | Poisson's ratio = 0.3 |
| | Inter-particle friction | 0.5 |
| Boundary conditions | Initial cell size | (Height × Width × Length) 5cm × 5cm × 5cm |
| | Vertical load | 100 kPa (during dissolution) |
| | Zero lateral strain | |
| | Particle-to-wall friction | 0 |

Summary of parametic study:
Solube particles (Fraction) SF=0, 2, 5, and 10%
Hindered rotation (Fraction) HR=0, 40, and 80%
Main control variable: Size reduction of soluble particles $\Delta R/R_0$

Dissolution under constant vertical stress (servo-controlled) and zero lateral strain $\varepsilon_h$=0 is simulated by gradually reducing the radius of all the soluble particles at the same rate (Figure 2.1). The ratio of the mean unbalanced force to the mean contact force is always smaller than 0.001 to ensure stable conditions throughout the dissolution processes. After dissolution, the specimen is either loaded at zero-lateral strain to assess stiffness or subjected to simple shear to evaluate the shear resistance and volume change (Figure 2.1).

*Particle rotation and angularity.* Spherical particles are used in this study. Spherical particles rotate more freely than non-spherical particles found in real sediments where interlocking inhibits rotation. While particle rotation has limited effect on elastic

properties (Bardet 1994, Mohamed and Gutierrez 2010), it has a significant effect on shear resistance and volume change (Bardet and Proubet 1991, Bardet 1994, Iwashita and Oda 1998).

The inter-particle friction cannot fully compensate for particle angularity (Skinner 1969). While particle shape can be numerically captured (Rothenburg and Bathurst 1993, Thomas and Bray 1999, Mirghasemi et al. 2002), more efficient alternatives are either to control particle rotation (Iwashita and Oda 1998, Iwashita and Oda 2000) or to hinder particle rotation (Bardet 1994, Suiker and Fleck 2004). In this study, we hinder rotation on a preselected percentage of particles HR% as a numerical proxy for angularity. We successfully compared results from this approach against experimental data in *Shin and Santamarina* (2009) and *Shin et al.*, (2008).

## 2.3 Results

A total of 45 simulations were completed, for 5 fraction of soluble particles SF%, 3 fractions with hindered rotation HR% and 3 loading stages. Results are presented next for the three simulation stages: dissolution, post-dissolution $k_0$-loading, and post-dissolution simple shear loading.

***Sediment evolution during dissolution ($\sigma_v$=constant; $\varepsilon_h$=0)***

The four specimens in Figure 2.2 were simulated without hindered rotation, HR=0%. The evolution of vertical displacement, porosity, and equivalent global stress ratio $k_0$ during dissolution are reported as a function of the size reduction of soluble particles $\Delta R/R0$ experienced by the dissolving particles for sediments with different fraction of soluble particles SF.

*Normalized vertical displacement.* The sediment contracts and settles during dissolution (Figure 2.2a). Settlements during early stages of dissolution, i.e., low $\Delta R/R_0$ or for

sediments with low percentage of soluble particles SF are very small as particle-level forces arch form to accommodate the force relinquished by dissolving particles. On the other hand, significant vertical displacements arise for high soluble fraction SF≥10% and during later stages of dissolution as force arches collapse and reform.

*Porosity.* Porosity increases as dissolution progresses $\Delta R/R_0\uparrow$ and as the soluble fraction SF increases (Figure 2.2b). The increase in porosity tends to an asymptotic value for each sediment type SF.

*Equivalent global stress ratio k.* All specimens show an increase in equivalent global stress ratio k during dissolution towards an asymptotic value that is characteristic for each SF (Figure 2.2c): the final k as $\Delta R/R_0 \rightarrow 100\%$ increases with increasing fraction of soluble particles SF.

Some experimental results with Ottawa sand and salt mixtures show that $k_0$ may reduce to $k_a$ during dissolution, and it may eventually recover if dissolution continues (Shin et al. 2008, Shin and Santamarina 2009). We compared and calibrated the numerical simulation to match the experimental trend by changing the percentage of particles with hindered rotation HR. The case of HR=80% simulates the previous experimental results most accurately (Figure 2.3). Figure 2.4 shows the angle of repose versus hindered rotation HR at an interparticle friction $\mu$=0.5; these values were gathered using DEM 2D and compared against previously reported DEM data. The trend between the angle of repose and the hindered rotation HR is almost linear. The rest of this study is conducted without hindered rotation HR=0% to focus on the phenomena of dissolution in the absence of numerical proxies.

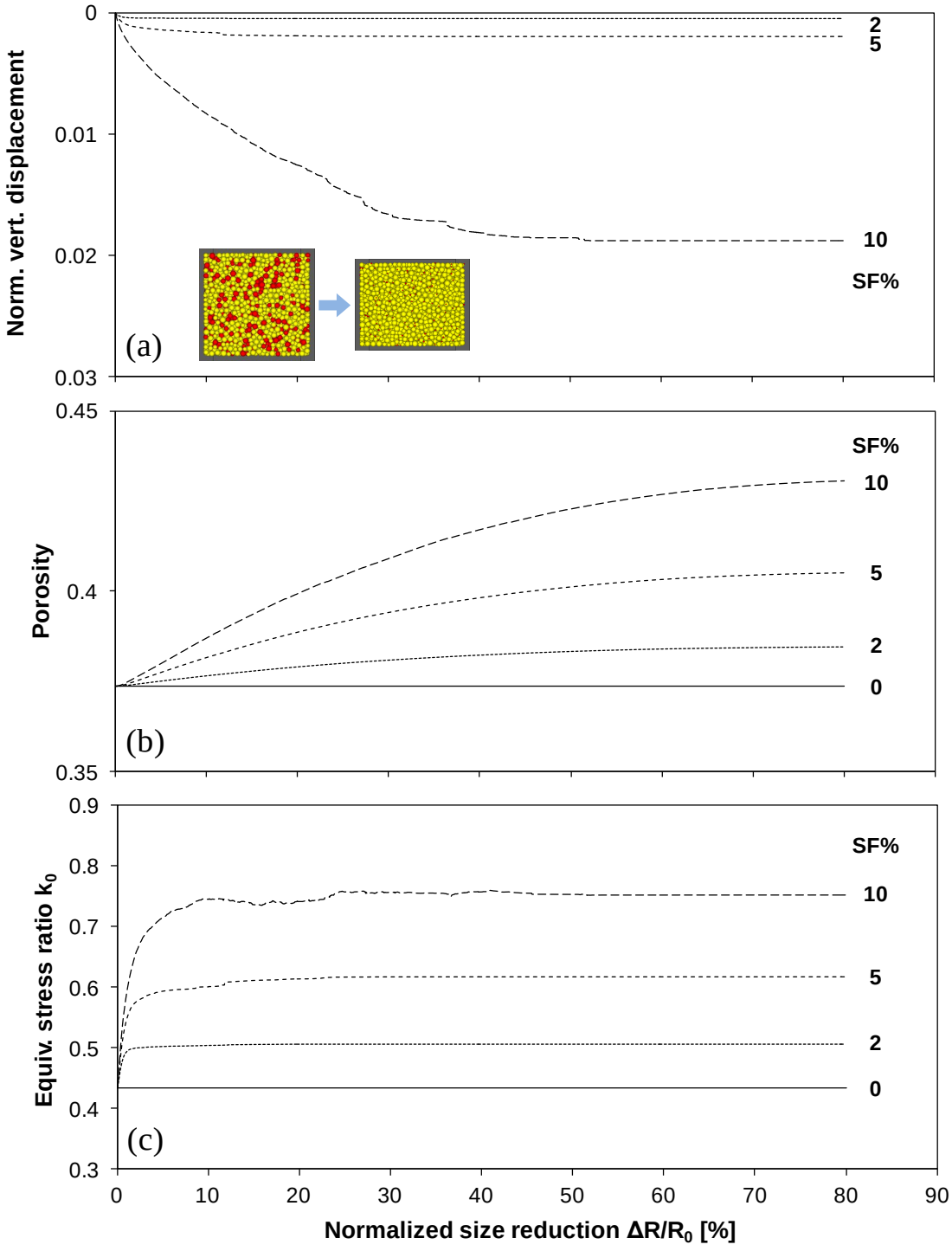


Figure 2.2 Sediment response during dissolution (hindered rotation HR=0%). (a) Normalized vertical displacement. (b) Porosity. (c) Equivalent global stress ratio $k_0$ under zero lateral strain condition. Trends shown for different soluble fractions SF.

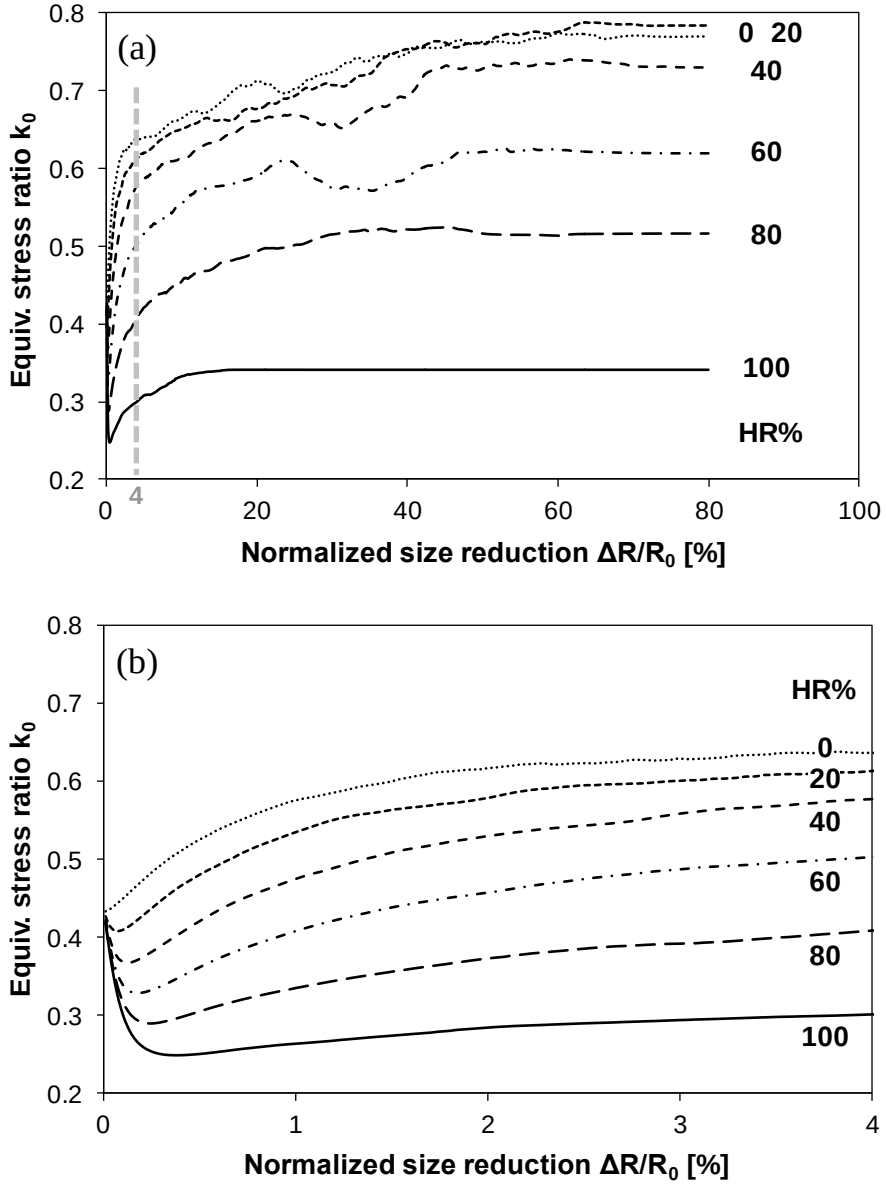


Figure 2.3 The effect of hindered rotation HR during dissolution (soluble particles SF=25%). The evolution of the equivalent stress ratio $k_0$ as a function of dissolution in terms of size reduction $\Delta R/R_0$ and hindered rotation HR. (a) Overall. (b) Early part.

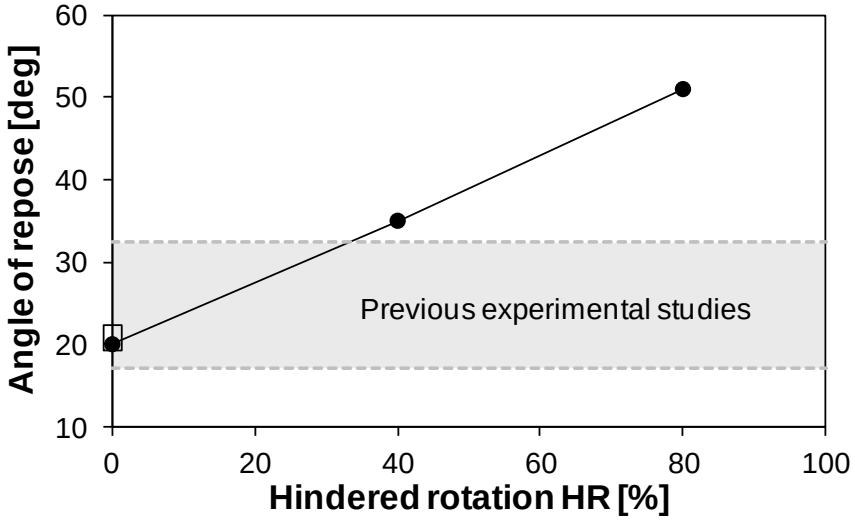


Figure 2.4 Angle of repose vs. hindered rotation HR – DEM 2D. Note: the symbol □ shows the range of constant volume friction angles reported from previous DEM studies for interparticle friction μ=0.5 (2D: Kruyt and Rothenberg 2006, 3D: Thornton 2000). The shaded area shows the range of published results (Rowe 1969, Skinner 1969).

***Post-dissolution vertical loading ($\varepsilon_h$=0)***

The post-dissolution sediment response to vertical loading under zero lateral strain $\varepsilon_h$=0 is investigated to assess changes in compressibility. Results shows:

1) The vertical displacement is higher for specimens that experienced a higher dissolution loss (Figure 2.5a).
2) Porosity decreases with increasing vertical stress, although the magnitude of volume contraction is relatively small compared to the gain in porosity during dissolution; a looser fabric remains even after an order of magnitude increase in stress (Figure 2.5b).
3) In fact the internal sediment structure is relatively unaffected by post-dissolution $k_0$-loading.
4) The equivalent global stress ratio $k_0$ decreases and reaches a stable value upon loading (Figure 2.5c).

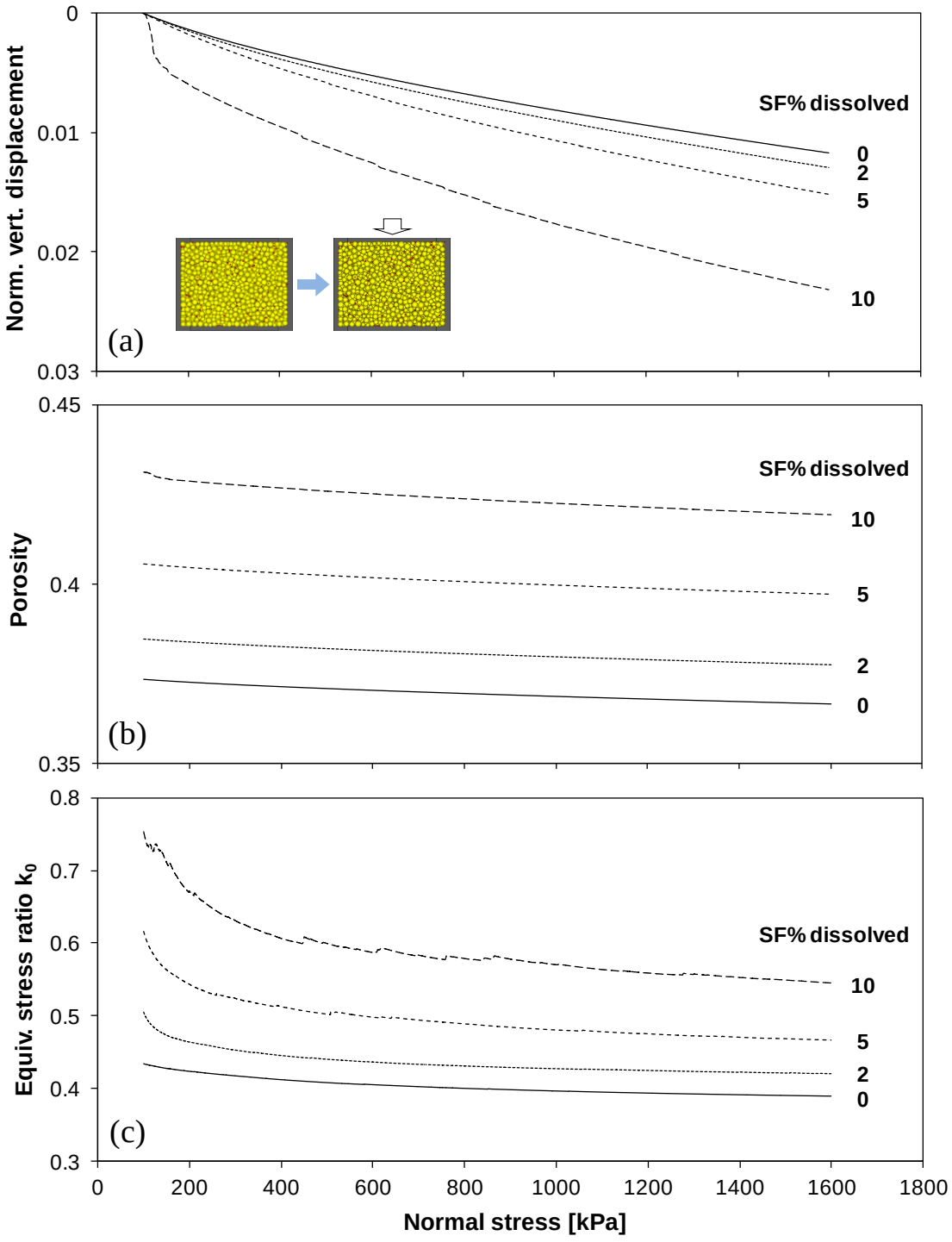


Figure 2.5 Post-dissolution response to additional $k_0$-loading (hindered rotation HR=0%). (a) Normalized vertical displacement. (b) Porosity. (c) Equivalent global stress ratio $k_0$ under zero lateral strain condition. Trends shown for different soluble fractions SF.

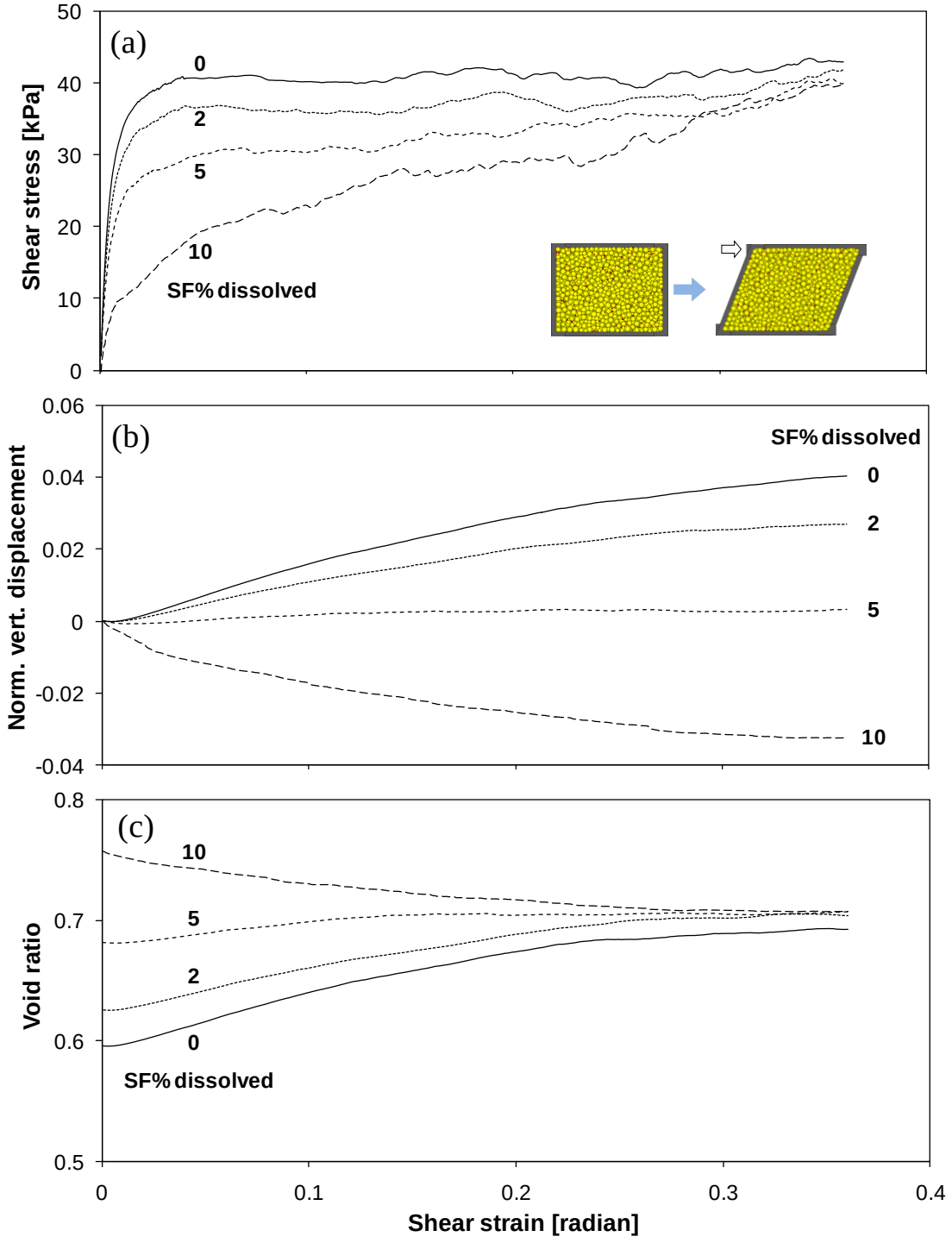


Figure 2.6 Post-dissolution response to simple shear loading (hindered rotation HR=0%). (a) Shear stress. (b) Normalized vertical displacement. (c) Void ratio. Trends shown for different soluble fractions SF.

***Post-dissolution simple shear loading***

The same sediments are subjected to post-dissolution simple shear ($\sigma_v$=const.) under constant vertical stress. Numerical results shows:

1) There is a pronounced decrease in shear stiffness with the increase in soluble fraction SF (Figure 2.6a).
2) Void ratio and the large strain shear resistance converge to a common "critical state" value for all specimens (Figure 2.6c).
3) The initially dilative sediment becomes more contractive as the soluble fraction SF increases (Figure 2.6b).

## 2.4 Particle-level Observations

*Coordination number*. The coordination number is a measure of fabric stability and it parallels porosity trends (Santamarina et al. 2001). The coordination number decreases as dissolution $\Delta R/R_0$ progresses and the initial soluble fraction SF increases (Note: this observation applies whether all contacts or only "real" contacts are considered - Details in Appendix A) (Figure 2.7). The coordination numbers evolve to a single value at large shear strains for all sediments, i.e., a "critical state" fabric.

*Histogram of contact forces.* Histogram of contact forces before and after dissolution are compared in Figure 2.8 for quasi-horizontal (±30° from horizontal axis) and quasi-vertical (±30° from vertical axis) contact forces. After dissolution, the total number of contacts decreases. Yet higher contact forces are mobilized both in vertical and horizontal directions, while the number of contacts with lower contact forces decreases.

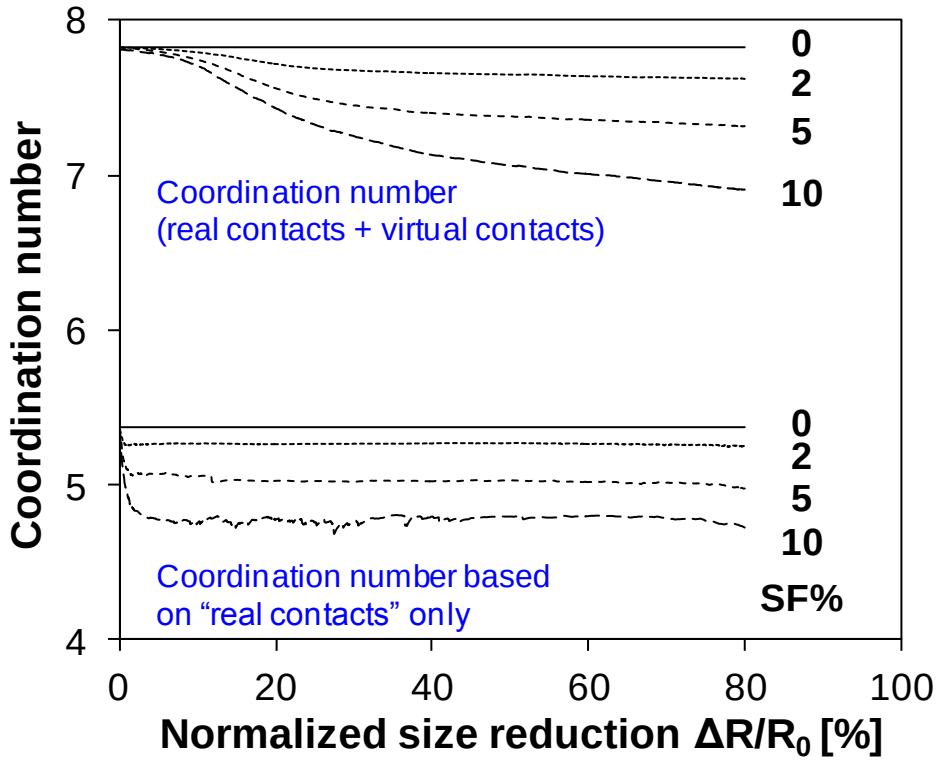


Figure 2.7 Evolution of coordination number during dissolution.

*Internal micromechanical histograms*. Figure 2.9 shows micromechanical polar plots. More contacts are aligned in the horizontal direction after dissolution (Figure 2.9a). The mean normal contact force diagram develops more horizontally and the mean tangential contact force decreases after dissolution; this trend becomes more prominent with a higher soluble fraction SF (Figure 2.9b&c). On the other hand, dissolution on highly interlocked sediments (HR≥40%) show that both the mean contact force and the mean tangential contact force increase after dissolution (Figure 2.10); Clearly, sediments with minimal interlocking or internal friction experience structural rearrangement that is not possible in interlocked sediments.

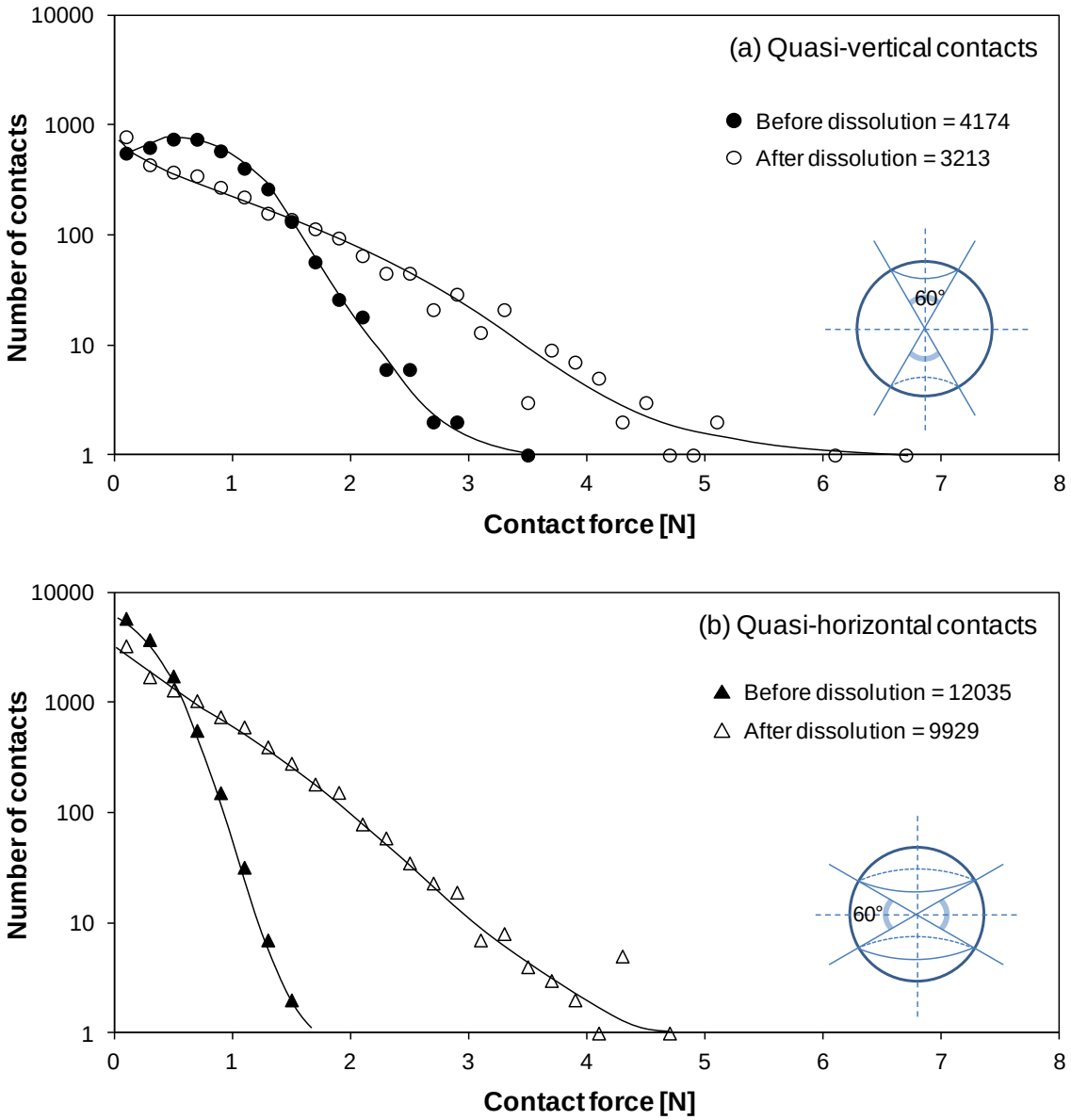


Figure 2.8 Histogram of contact forces before and after dissolution for quasi-vertical (±30° from vertical) and quasi-horizontal contacts (±30° from horizontal) - Soluble fraction SF=10%; hindered rotation HR=0%.

| | Before dissolution | At the end of dissolution | |
|---|---|---|---|
| | | SF=2% | SF=10% |
| (a) Contact density | 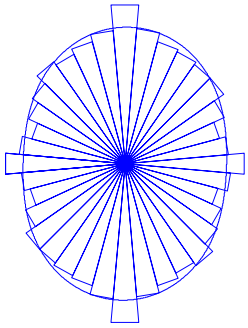 | 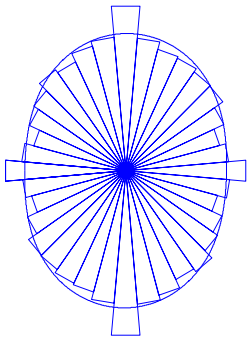 | 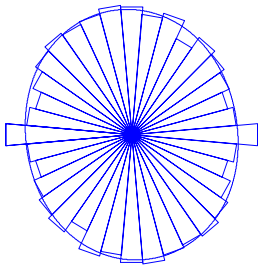 |
| (b) Mean normal contact force<br><br>(Scale=1) | 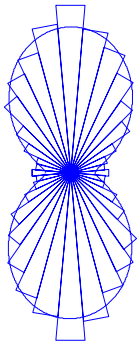 | 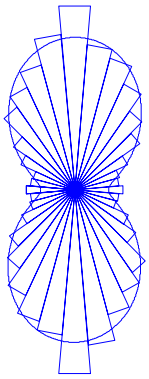 | 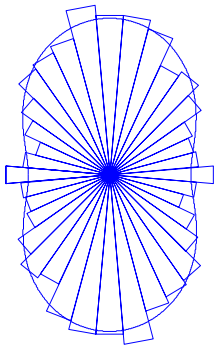 |
| (c) Average tangential contact force<br><br>(Scale=0.16) | 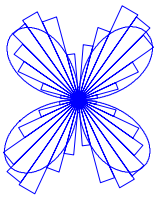 | 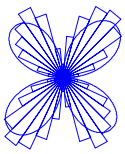 |  |
| Equivalent global stress ratio k | 0.43 | 0.50 | 0.75 |

Figure 2.9 Polar plots of internal micromechanical parameters before and after dissolution **(HR 0%)**. (a) Contact density histogram. (b) Mean normal contact force. (c) Mean tangential contact force. Note that the contact histograms are captured along bands between consecutive parallels and normalized by areas.

| | Before dissolution | During dissolution at minimum k | At the end of dissolution |
|---|---|---|---|
| (a) Number of contacts | 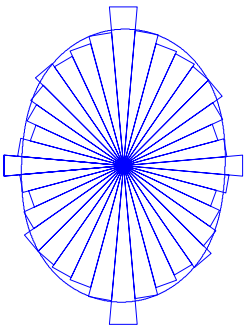 | 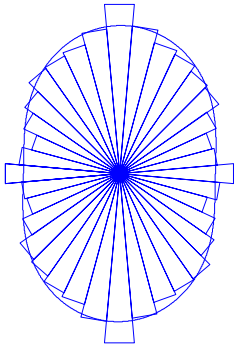 | 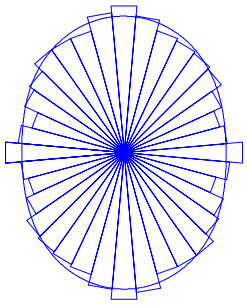 |
| (b) Average normal contact force<br><br>(Scale=1) | 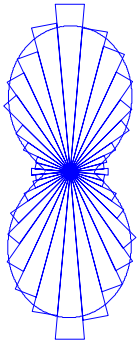 | 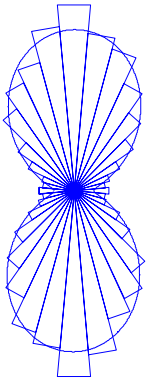 | 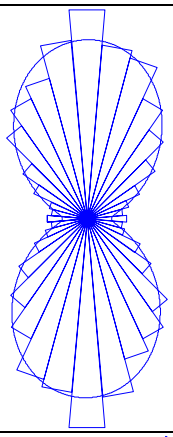 |
| (c) Average tangential contact force<br><br>(Scale=0.15) | 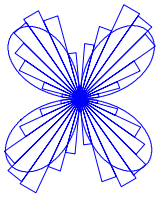 | 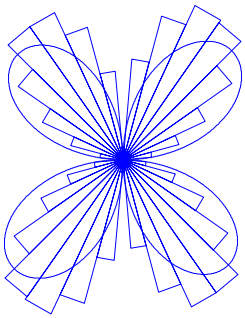 | 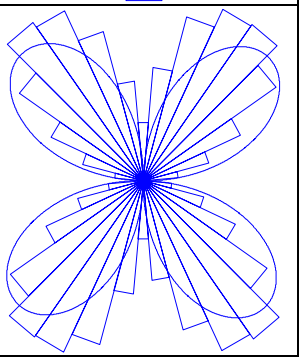 |
| Equivalent global stress ratio k | 0.43 | 0.35 | 0.36 |
| | Free rotation | HR=80% | |

Figure 2.10 Polar histograms of internal micromechanical parameters before dissolution, at minimum k, and after dissolution **(HR=80% and SF=10%)**. (a) Contact density histogram. (b) Mean normal contact force. (c) Mean tangential contact force. Note that the contact histograms are captured along bands between consecutive parallels and normalized by areas.

Mass loss at constant volume implies gain in porosity ($\Delta n$):

$$\frac{\Delta n}{n_0} = \frac{1-n_0}{n_0}\left(\frac{M_{S0}-M_{Sd}}{M_{S0}}\right) \tag{2.1}$$

where $n_0$ is an initial void ratio, $M_{S0}$ is an initial solid mass, and $M_{Sd}$ is a solid mass after dissolution. Indeed plots of porosity vs. mass loss superimpose with the line for dissolution at constant volume for low fraction of soluble particles SF (Figure 2.11a), suggesting the development of internal arching to effectively accommodate mass loss with minimum vertical displacement. Arch formation depends on factors such as interparticle friction and particle angularity. Indeed, sediments with hindered rotation HR=80% tend to experience mineral dissolution at constant volume even for relatively high fraction of soluble particles SF (Figure 2.11b).

## 2.5 Discussion - Implications

Mineral dissolution is one of the main chemical weathering diagenetic processes in geological systems. Dissolution and reprecipitation change volcanic ash from a sediment with a void ratio e=0.8~1.5 and specific surface $S_S$= 0.1~1$m^2$/g to a sediment with e=2~7 and $S_S$=50~200$m^2$/g (Herrera et al. 2007). Furthermore, dissolution may cause the formation of polygonal faults observed in marine basins (Cartwright and Dewhurst 1998, Shin et al. 2008).

Mineral dissolution can accelerate piping erosion, increase uplift pressure, and compromise the stability of dams (Dreybrodt et al. 2002, Pearson 2002, Gutiérrez et al. 2003, Jarvis 2003, Payton and Hansen 2003, Craft 2005, Craft et al. 2006). Therefore, the dissolution of soluble minerals is a crucial factor when assessing dam sites and construction materials (Unay et al. 1982, Johnson 2003a, Johnson 2003b, Johnson 2008).

Non-mineral solid phases may also vanish, such as ice in frozen ground or methane hydrate in marine sediments or beneath the permafrost (Rothwell et al. 1998, Vogt and Jung 2002, Sultan et al. 2004a, Freij-Ayoub et al. 2007).

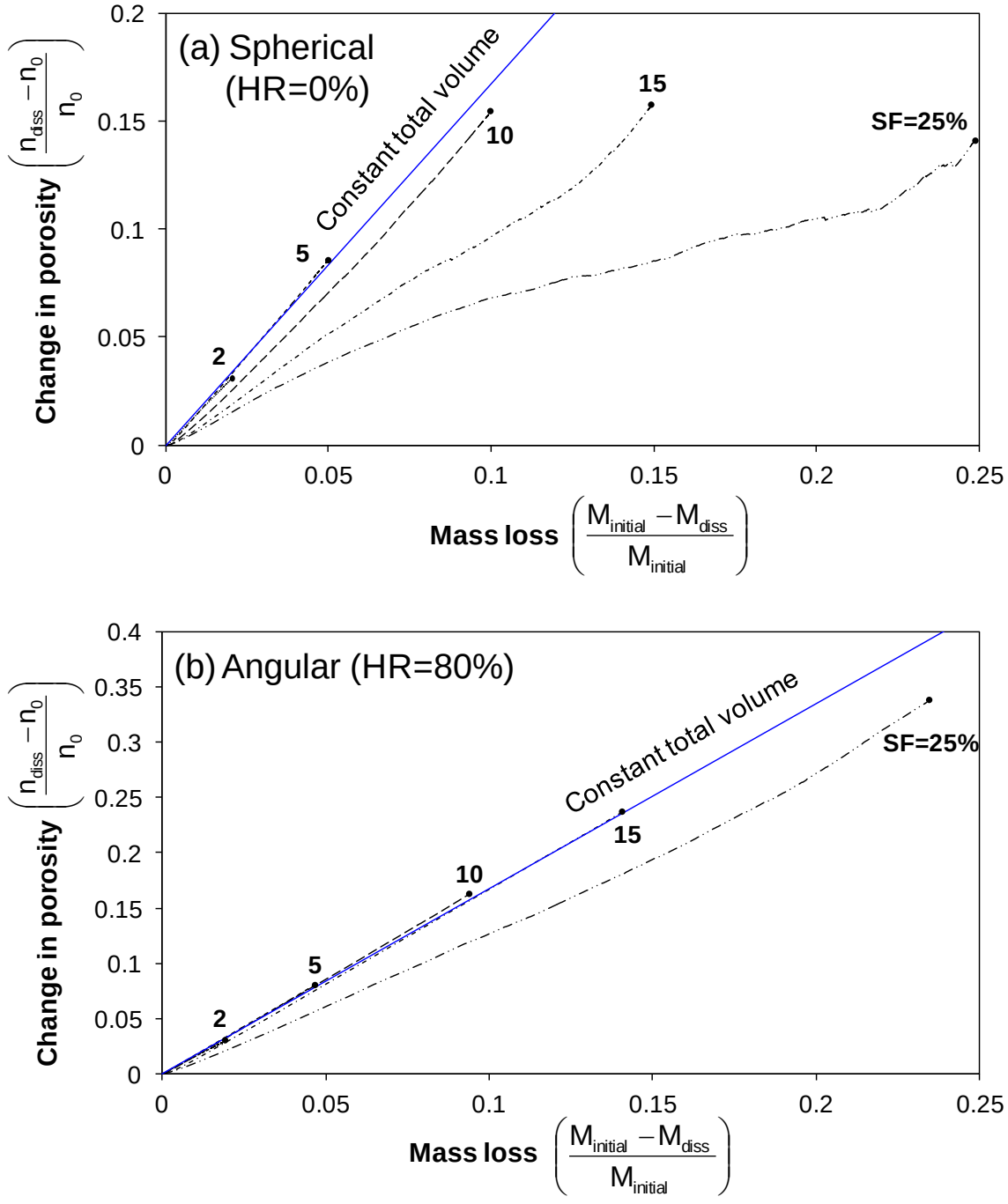


Figure 2.11 Change in porosity $\Delta n/n_0$ versus mass loss $\Delta M/M_0$. (a) hindered rotation HR=0%. (b) hindered rotation HR=80%.

The geological storage of $CO_2$ is of particulate interest in this context: $CO_2$ dissolves in water and acidifies it to pH≈3 where most minerals tend to dissolve (Cowan and Weintritt 1976, Montes-Hernandez et al. 2007, Espinoza et al. 2011). The ensuing hydro-chemo-mechanical coupling can lead to porosity and mineralogy changes, settlement, tensile fracturing of the caprock, piping, and shear failure in compression (He et al. 2003, Watson 2004, Renard et al. 2005, Le Guen et al. 2007, Espinoza et al. 2011). Therefore, the analysis of geological storage sites must consider the possible consequences of mineral dissolution.

## 2.6 Conclusions

Mineral dissolution is a common digenetic process. Furthermore, solid phase loss can take place within the design life of some engineered systems. The loss of solid mass has important particle and macroscale implications. Numerical results obtained in this study show that:

- Grain dissolution at zero lateral strain affects the equivalent global stress ratio $k_0$. Its evolution depends on the degree of particle interlocking. While the equivalent global stress ratio $k_0$ increases in rounded particles, the value of $k_0$ may decrease to $k_a$ during mineral dissolution of sediments made of angular particles.
- While there is vertical settlement, there is also increase in porosity during dissolution.
- The coordination number decreases and preponderant interparticle force chains develop in the sediment.
- The post-dissolution vertical loading at zero-lateral strain shows that sediments after dissolution are more compressible than the original sediment before dissolution. The increase in compressibility correlates with the extent of dissolution the sediment has experienced.

- Post-dissolution simple shear loading encounters lower shear stiffness and higher contractive tendency in sediments that have experienced more pronounced dissolution. Therefore, post dissolution sediments will be more vulnerable to liquefaction when sheared under undraind condition.
- Regardless of the extent of dissolution, all specimens evolve to the same critical state strength and void ratios at large strain.

# CHAPTER 3

# PRESSURE-DEPENDENT MINERAL DISSOLUTION -IMPLICATIONS ON SOIL FORMATION

## 3.1 Introduction

Pressure solution is a salient diagenetic process in sediments under high stress levels. It involves the preferential dissolution of minerals at grain contacts followed by diffusive mass transfer to the surrounding pore. The dissolved species either deposited onto nearby stress-free surfaces (Rutter 1983, Fowler and Yang 1999), or are advectively transported away (Etheridge et al. 1984).

Pressure solution contributes to sediment compaction and porosity reduction (Angevine and Turcotte 1983, Tada and Siever 1989, Croize et al. 2010). It is an important mechanism in soil and rock creep (Kuhn and Mitchell 1993, McDowell and Khan 2003), and for ductile rock deformation in the upper crust (Durney 1972, Elliott 1973, Groshong 1975, Rutter 1983, Lehner 1995). Furthermore, pressure solution facilitates fault healing and strength recovery between seismic events (Angevine et al. 1982, Sibson 1986, Yasuhara et al. 2005, Niemeijer et al. 2008).

Pressure solution results from differences in surface chemical potential between the mineral at contacts and the stress-free mineral (Lehner 1995, Shimizu 1995, Gratier et al. 2009). Consequently, pressure solution responds to effective stress. The proportionality between stress and pressure solution rate is either linear (De Boer et al. 1977, Raj 1982, Rutter 1983, Hellmann et al. 1998), or an exponential function of effective stress (Dewers and Hajash 1995, Gratier et al. 2009).

Because solubility and diffusion are involved, pressure solution is favored at high temperature (Rutter 1983) and fluid pressure (Sprunt and Nur 1977), and in minerals that

are thermodynamically unstable, such as calcite. The decrease in grain size or the increase in specific surface increases solubility and pressure solution rate (De Boer 1977, Sprunt and Nur 1977, Raj 1982, Niemeijer et al. 2009).

In this study, we explore pressure-dependent mineral dissolution at the grain scale by means of the discrete element method to gain insight into the underlying processes and possible emergent phenomena. The methodology is described first.

## 3.2 Methodology

The PFC discrete element code is used to conduct 2D and 3D simulations (Cundall and Strack 1979). Table 3.1 describes the properties of the simulation environment for 2D and 3D cases, and Table 3.2 summarizes the five sets of simulations performed in this study. Zero lateral strain boundaries are imposed in all cases. The vertical boundary is either constant stress or a free surface. The 2D circular disks or 3D spheres (uniform size distribution – Table 3.1) are generated at random locations in a closed container, and allowed to grow to their final size under zero gravity and zero grain friction. The confined sediment is gradually compacted to a nominal vertical stress of 100kPa (zero-lateral strain). In the free surface condition, after the upper boundary is removed, interparticle friction is applied and gravity is gradually turned. We simulate granular interlocking due to grain angularity by hindering rotation on a preselected fraction of randomly distributed particles HR.

Table 3.1 Discrete element simulation environment.

| | Properties | DEM 2D | DEM 3D |
|---|---|---|---|
| Particle properties | Initial radius of particles | Uniform size distribution ($R_{min}$=0.4mm, $R_{max}$=0.6mm) | Uniform size distribution ($R_{min}$=1mm, $R_{max}$=1.5mm) |
| | Number of particles | 10567 disks | 9167 spheres |
| | Density of particles | 2650 kg/m$^3$ | |
| | Contact model | Linear contact model<br>-Normal stiffness $k_n$ =10$^8$ N/m<br>-Shear stiffness $k_s$ = 10$^8$ N/m | Hertzian contact model<br>-Shear modulus = 2.9×10$^9$ Pa<br>-Poisson's ratio = 0.3 |
| | Inter-particle friction | 0.5 | |
| | Hindered rotation HR | 1) 0% and 2) 80% | 0% |
| Boundary conditions | Initial cell size | (Height × Width)<br>10 cm × 10 cm | (Height × Width × Length)<br>5cm × 5cm × 5cm |
| | Vertical load | 1) 100 kPa<br>2) Self weight (open surface) | 100 kPa |
| | Lateral boundaries | Zero strain | |
| | Particle-to-wall friction | 0 | |
| Dissolution rate vs. contact force | 1) Dissolution rate = A (contact force)$^1$<br>2) Dissolution rate = A (contact force)$^2$ | | |

Table 3.2 Simulation sets.

| Dimensions | Vertical boundaries | Hindered rotation | Dissolution rate vs. force |
|---|---|---|---|
| 2D | Confined | 0% | Linear ($dR/dt = \alpha \cdot F_N$) |
| | | | Quadratic ($dR/dt = \alpha \cdot F_N^2$) |
| | | 80% | Linear ($dR/dt = \alpha \cdot F_N$) |
| | Open surface | 0% | Linear ($dR/dt = \alpha \cdot F_N$) |
| 3D | Confined | 0% | Linear ($dR/dt = \alpha \cdot F_N$) |

Pressure solution is simulated through multiple particle size reduction steps, each followed by an equilibration stage. Each grain is shrank proportionally to the contact force. We use three different dissolution rate functions $dR/dt=\alpha(\Sigma F_N)^\beta$ in terms of the contact force (Figure 3.1): linear ($\beta=1$), quadratic ($\beta=2$), and cubic ($\beta=3$). For each time step, the updated particle size $R_{i+1}$ is computed from its previous size $R_i$ as $R_{i+1}=R_i-\alpha(\Sigma F_N)^\beta$. The proportionality constant $\alpha$ is selected so that size changes in any time step are small enough to ensure gradual size reduction and prevent numerical instability. The parameters $\alpha$ and $\beta$ are the same for all particles and constant throughout a given simulation. The internal macro-scale evolution of the sediment is recorded throughout the simulation. Reprecipitation is not modeled in this study, thus, we assume that dissolved species are transported out of the model boundaries. Note that particles remain circular or spherical throughout the simulation, yet grains change shape in natural pressure solution.

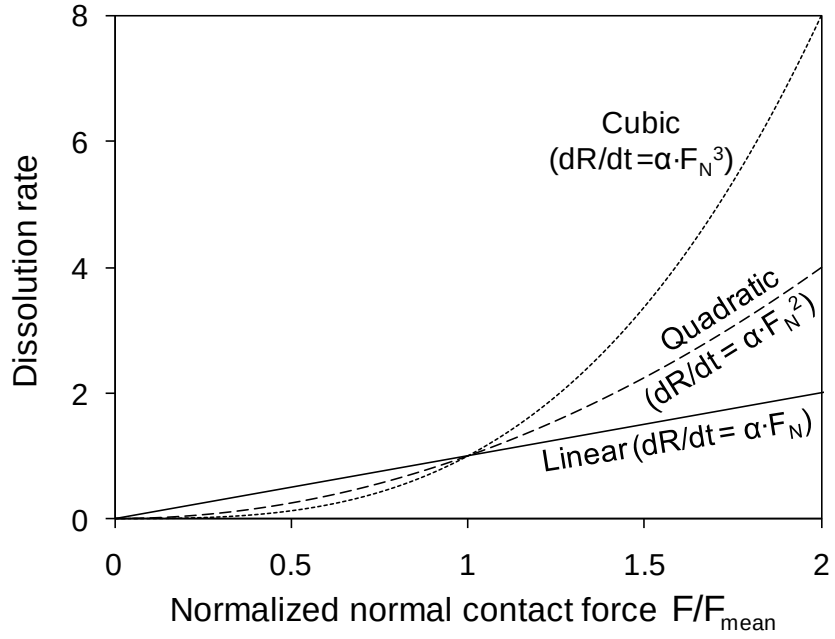


Figure 3.1 Different relationships between normal contact force and dissolution rate (Linear and quadratic relationships are employed in our simulations).

### 3.3 Results and analyses

Particle- and macro-scale simulation results are presented versus the normalized change in solid volume

$$\frac{\Delta V}{V_0} = \frac{\sum V_{initial} - \sum V_{current}}{\sum V_{initial}} = \frac{\sum R^2_{initial} - \sum R^2_{current}}{\sum R^3_{initial}} \quad (\text{for 2D disks}) \tag{3.1}$$

and

$$\frac{\Delta V}{V_0} = \frac{\sum V_{initial} - \sum V_{current}}{\sum V_{initial}} = \frac{\sum R^3_{initial} - \sum R^3_{current}}{\sum R^3_{initial}} \quad (\text{for 3D spheres}) \tag{3.2}$$

***Shear localization***

Contact forces align preferentially in the vertical direction, i.e., the principal stress direction, before dissolution (zero lateral strain condition; equivalent stress ratio $k_0$=0.48). (Figure 3.2). As force-dependent dissolution progresses, a shear band develops spontaneously.

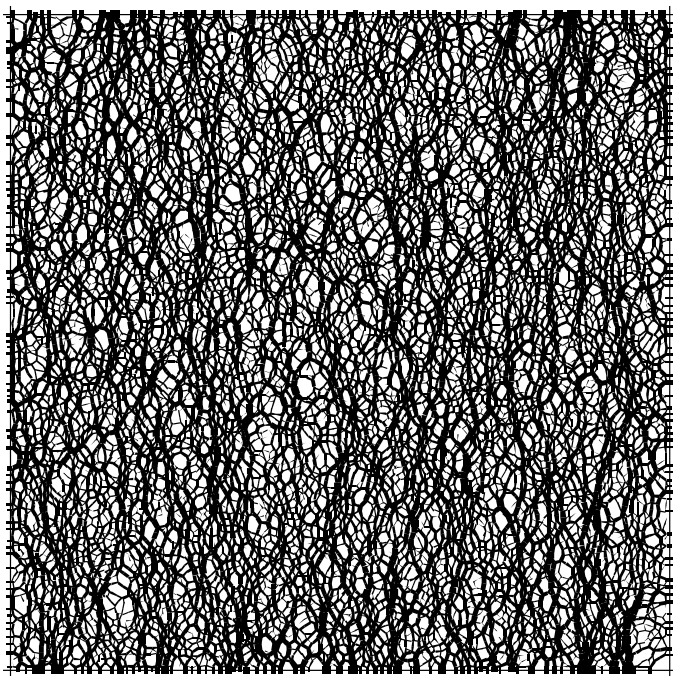

Figure 3.2 Contact force chains after zero-lateral strain loading- Initial condition (Case: 2D confined).

The shear band is 12~15 particles in thickness. Marked force chains form inside the shear bands at a characteristic angle of about 56° with the shear band (in the case of $dR/dt=\alpha \cdot F_N$ & HR=0% - Figure 3.3a). These strong force chains form and buckle during the simulation. Force chain formation and force-dependent dissolution combine to create the positive feedback dissolution that promotes the emergence of shear bands and sustains them.

Displacement localization occurs along shear bands (Figure 3.3b) and particles tend to move in wedges, even though dissolution does take place inside the wedges. The equivalent strain field shows a similar trend (Figure 3.3c). The inherent emergence of shear localization in pressure solution is a remarkable result from this simulation.

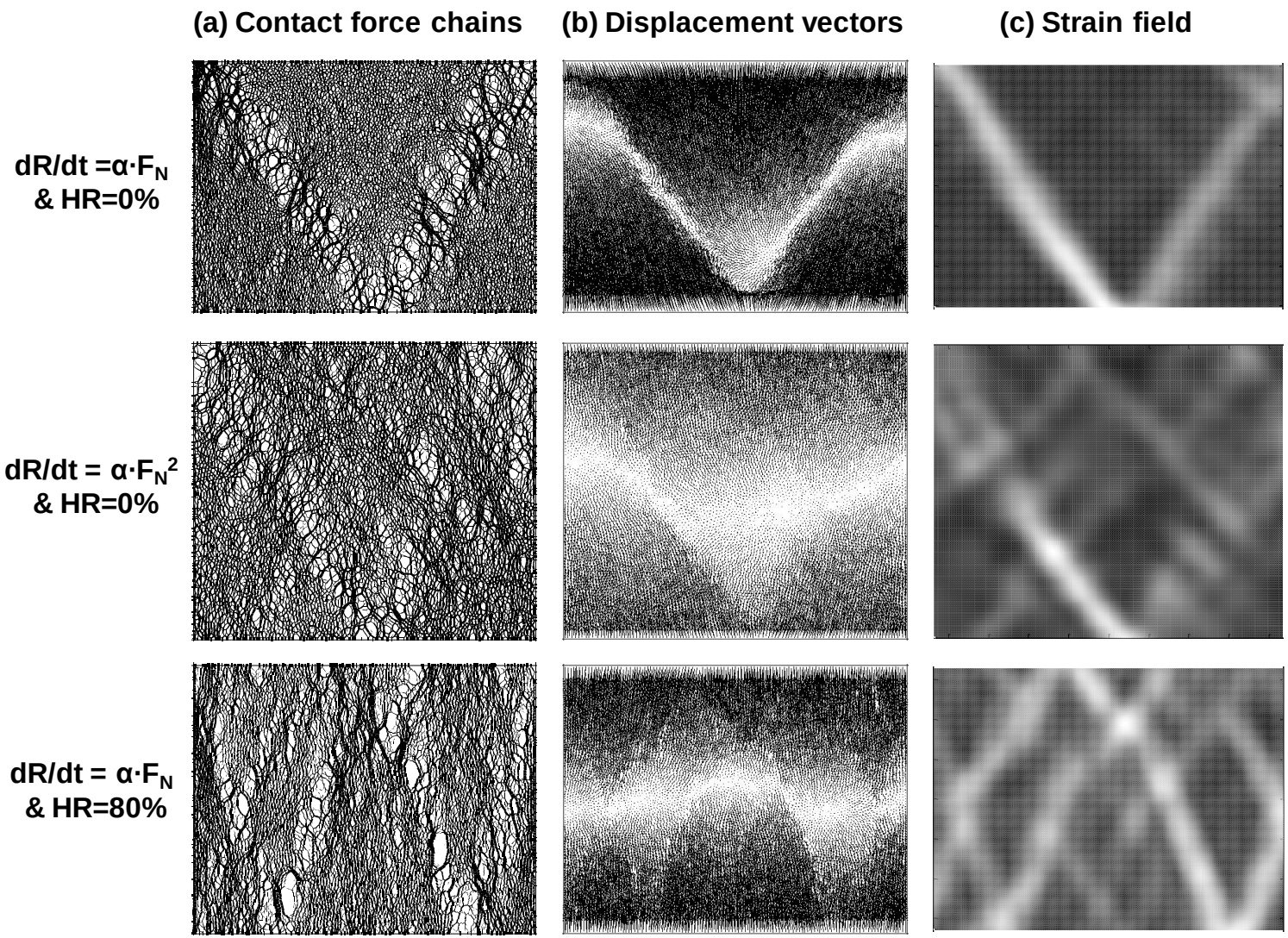


Figure 3.3 Shear strain localization at the end of the simulation (Cases: 2D confined). Note that displacements and strain fields are from the beginning and to the end. (a) Contact force chains. (b) Displacement vectors. (c) Strain field.

***Vertical displacement and porosity***

The vertical displacement increases almost linearly with the normalized change in solid volume (Figure 3.4). Higher sediment interlocking in terms of the fraction of particles with rotational frustration HR hinders vertical displacement. The pre-dissolution 2D porosity is n=0.165 globally; after dissolution, the porosity of the area outside the shear band contracts to n=0.147, while the porosity increases to n=0.187 inside the shear band (Case: 2D confined, $dR/dt= \alpha \cdot F_N$ and HR=0%).

***Equivalent global stress ratio k***

In all cases, the horizontal stress decreases as pressure solution begins (Figure 3.4b), reaches a minimum value and gradually recovers, similar to the case observed in homogeneous dissolution with interlocking (Chapter 2). The minimum stress ratio takes place just before the initiation of the shear band. Granular interlocking hinders stress transfer to the horizontal direction and $k_0$ values are lower (Figure 3.4b). Fluctuations in the equivalent global stress ratio $k_0$ after full recovery may indicate cycles of force chains formation and buckling inside shear bands (Figure 3.4b).

***Coordination number***

The coordination number increases at the beginning of pressure solution begin in all cases (Figure 3.4), as grain sizes adjust proportional to contact force. However as pressure solution progresses, the global coordination number of sediments with high interlocking decreases (HR=80% - Figure 3.4c), in part because of the thick relative area involved in shear bands in these small size experiments.

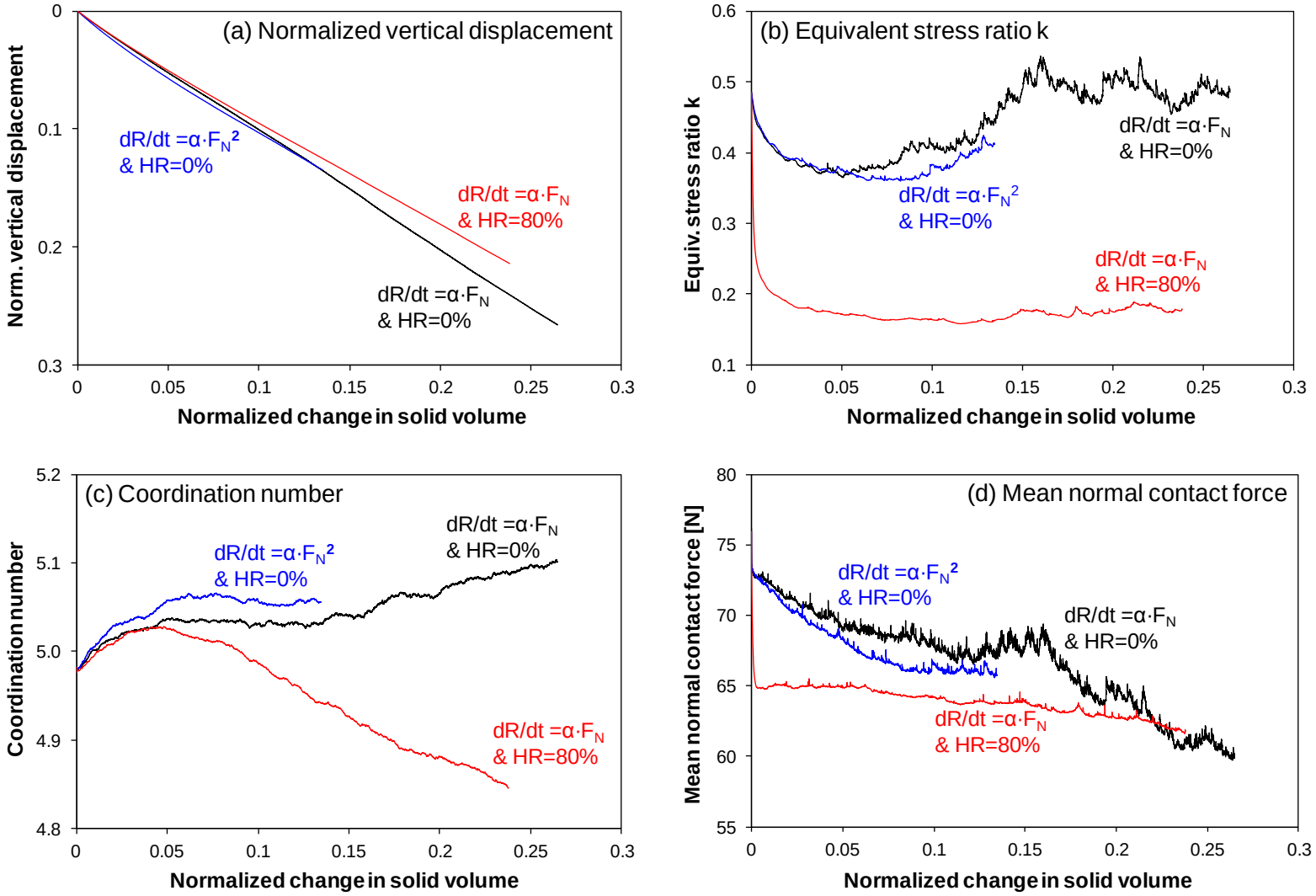


Figure 3.4 Evolution of macroscale and grain-scale parameters during pressure-dependent dissolution (Cases: 2D confined).

***3D simulations***

Macroscale and particle-scale parameters in 3D simulations follow similar trends to the corresponding 2D simulation results (Figure 3.5). Similar to the case of 2D quadratic force-dissolution relation, the global porosity and coordination number start to decrease after reaching the minimum k.

***Pressure solution under open upper boundary condition***

In open-surface gravity-dominated conditions, shear localization is more pronounced at depth than near the free surface because higher contact forces favor pressure solution. The localization becomes fuzzy and fades away towards the surface (Figure 3.6). Yet, grain- and macro-scale parameters show similar global trends to 2D confined cases.

***Evolution of grain size distribution***

The initial grain size distribution is uniform before pressure solution in all cases. As pressure dissolution progresses, the size distribution shifts to smaller sizes and evolves towards a Gaussian distribution (Figure 3.8b).

***Polar plots of internal micromechanical parameters***

High contact densities along strong contact force chains inside the shear band are captures in the histograms of contact density at the minimum $k_{min}$ and the end of simulation (Figure 3.10b&c). Contact density and normal contact forces become most anisotropic when the global equivalent stress ratio reaches $k_{min}$ (Figure 3.10). Average tangential contact forces decrease as pressure solution progresses due to emergence of shear localization.

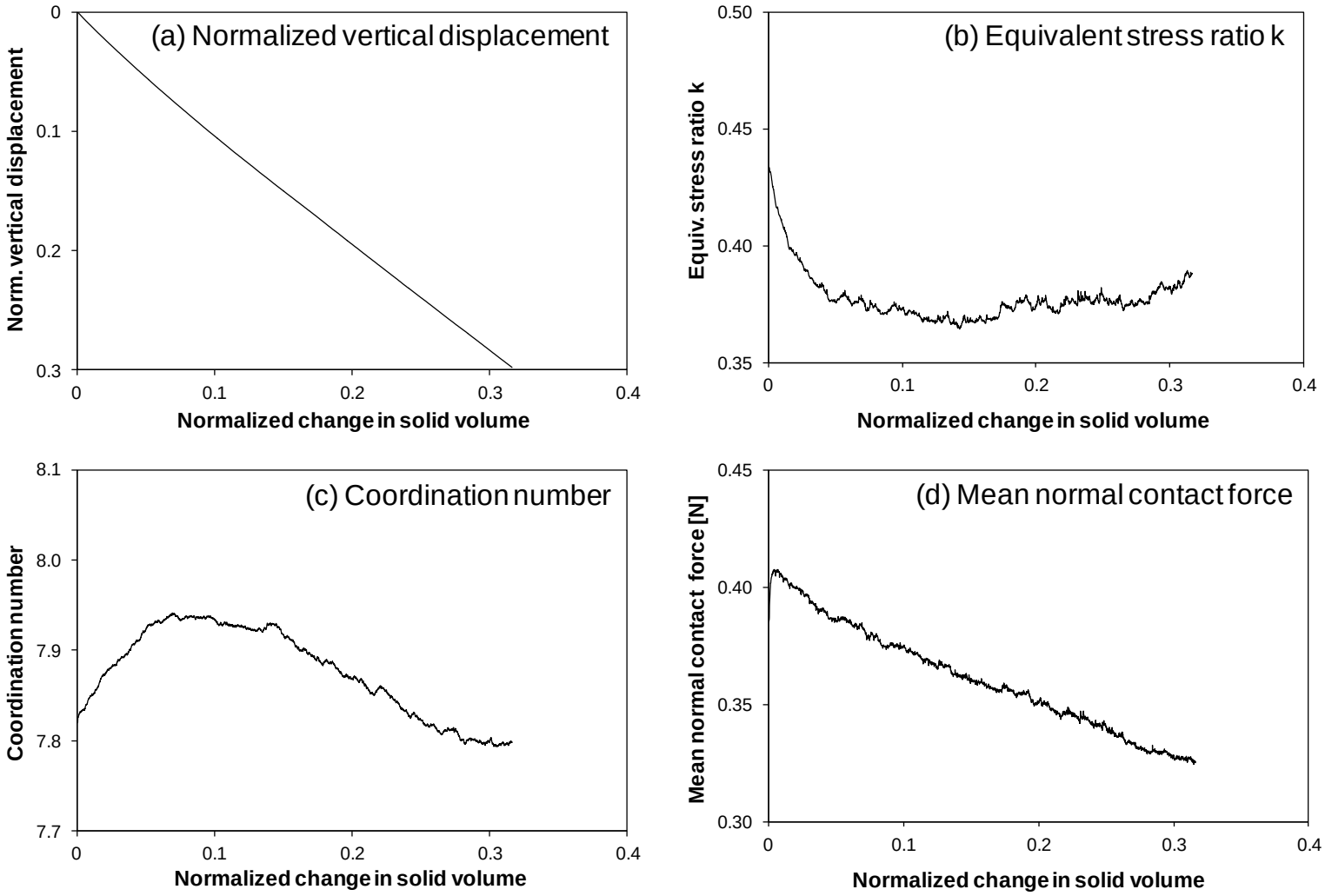


Figure 3.5 Evolution of macroscale and grain-scale parameters during pressure-dependent dissolution (Case: 3D confined, $dR/dt = \alpha \cdot F_N$, and HR=0%).

(a) Contact force chains (b) Displacement vectors (c) Strain field

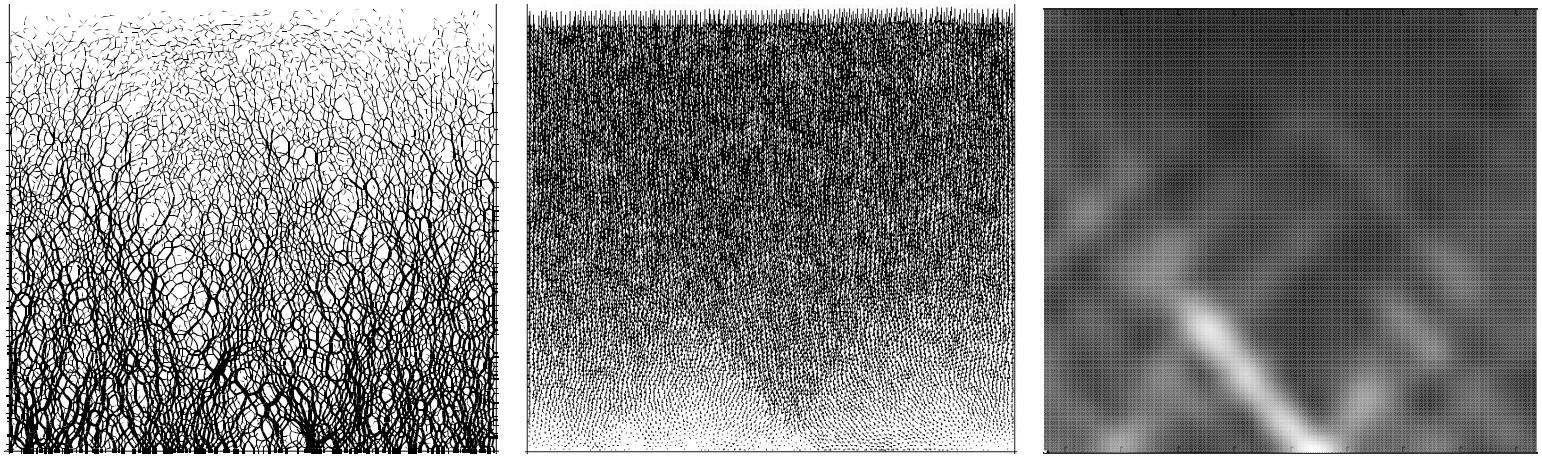

Figure 3.6 Shear band visualization at the end of the simulation (Cases: 2D near surface, $dR/dt = \alpha \cdot F_N$, and HR=0%). Note: displacement and strain fields are from the initial condition before dissolution. (a) Contact force chains. (b) Displacement vectors. (c) Strain field.

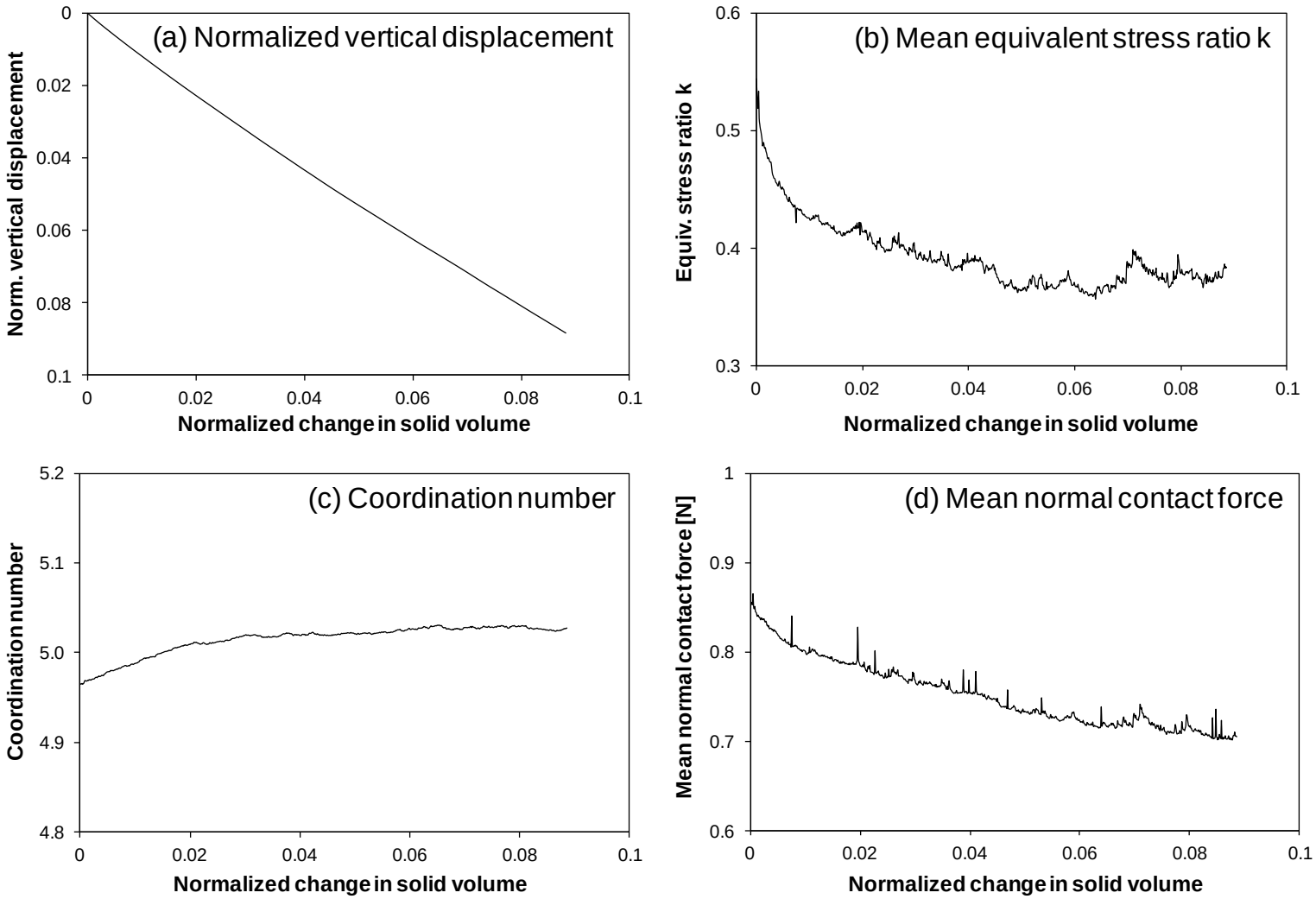


Figure 3.7 Evolution of macroscale and grain-scale parameters during pressure-dependent dissolution (Case: 2D near surface, $dR/dt = \alpha \cdot F_N$, and HR=0%).

## 3.4 Discussion and implications

Dissolution in the absence of re-precipitation implies increase in porosity and sediment weakening. On the contrary, pressure solution–precipitation contributes to sediment densification. In fact, low-grade metamorphosis heavily involves pressure solution (Elliott 1973, Lehner 1990).

Homogeneous dissolution without precipitation, studied in Chapter 2, tends to happen in low-stress near-surface sediment (<1km), in advection-dominant conditions. On the other hand, pressure solution-precipitation is more prevalent in high-stress, deep underground formation under diffusion-dominant conditions.

***Homogenization of normal contact force***

Pressure-dependent dissolution promotes contact force homogenization at the beginning of dissolution. Once the shear localization is triggered, force homogenization remains within blocks or wedges, but it becomes polarized within bands (Figure 3.3a).

Figure 3.8a compares normal contact force histograms before and after dissolution (case: 2D confined, $dR/dt=\alpha \cdot F_N$, and HR=0%). Normal contact forces show a lower spread, i.e., more homogeneous, after dissolution.

***Coordination number and interparticle forces***

The increase in coordination number and the homogenization of contact forces during pressure solution is explained by replacing grains for springs in Figure 3.9. Initially, only a few large springs contribute to load carrying. If a homogenous dissolution mechanism is applied, all particles or springs dissolve at the same rate, thus, the total number of contacts and contact forces do not change. However, if dissolution is "force" dependent, heavily loaded particles or springs will shorten first and shed force to other springs; in fact, new springs will come in contact.

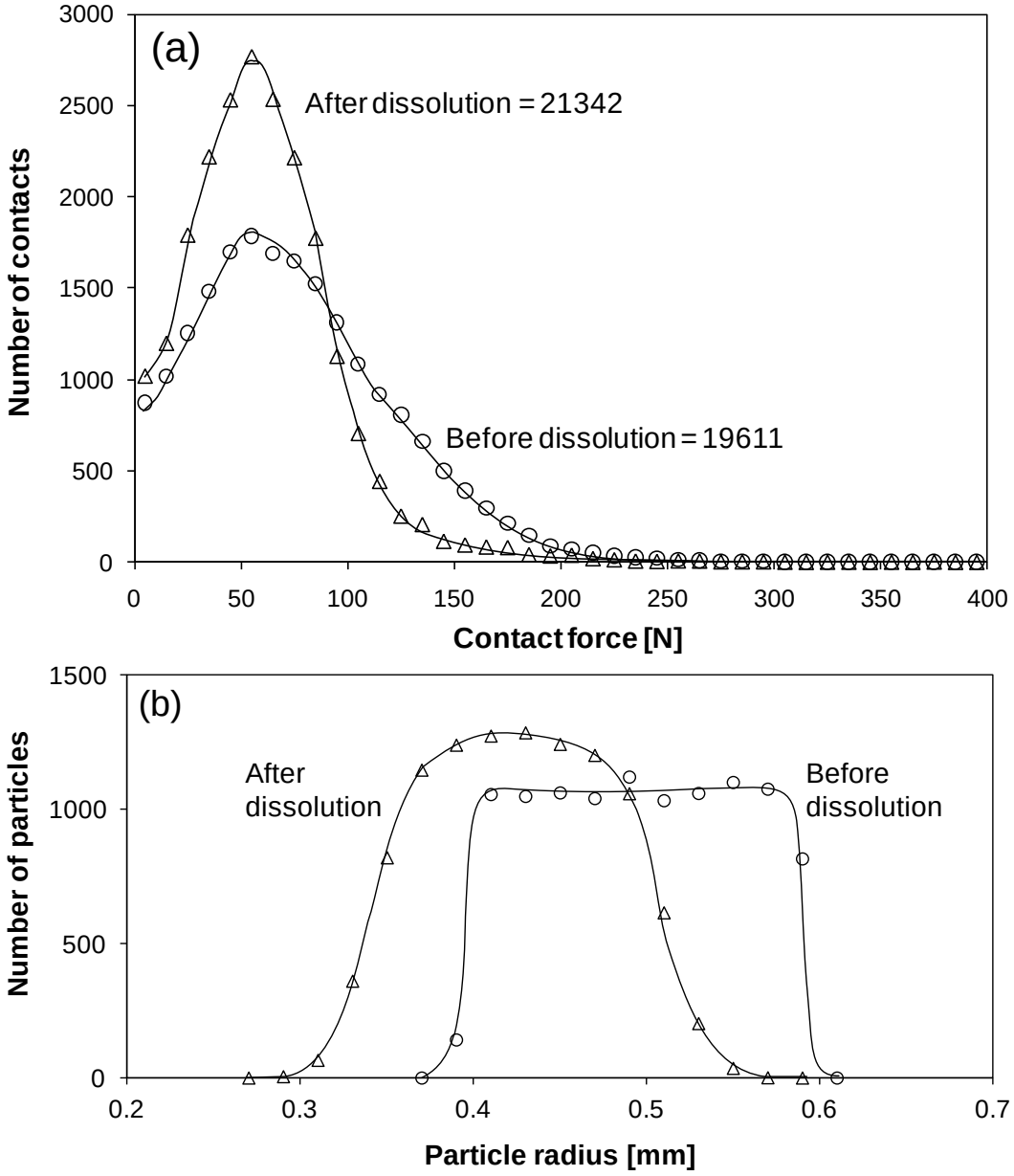


Figure 3.8 Histograms of (a) contact normal force and (b) particle size before and after dissolution (Case: 2D confined, $dR/dt = \alpha \cdot F_N$, and HR=0%).

***Polygonal faults***

Extensive polygonal fault systems are found in seafloor sediments in the absence of tectonism (Cartwright et al. 2003). Dissolution mechanisms have been suggested as one of the potential causes for the formation of polygonal faults (Hibsch et al. 2003, Shin et al. 2008, Shin et al. 2010). Results presented in this chapter confirm that shear localization can emerge in normally consolidated sediments that experience pressure solution under zero-lateral strain boundary conditions. In agreement with numerical results, the angle of polygonal faults increases as depth decreases as shown in Figure 3.6 (Lawrence and Cartwright 2009, Cartwright 2011). The V-shaped polygonal fault topology is also observed in shear bands that form during pressure solution in granular systems (Figure 3.3&6).

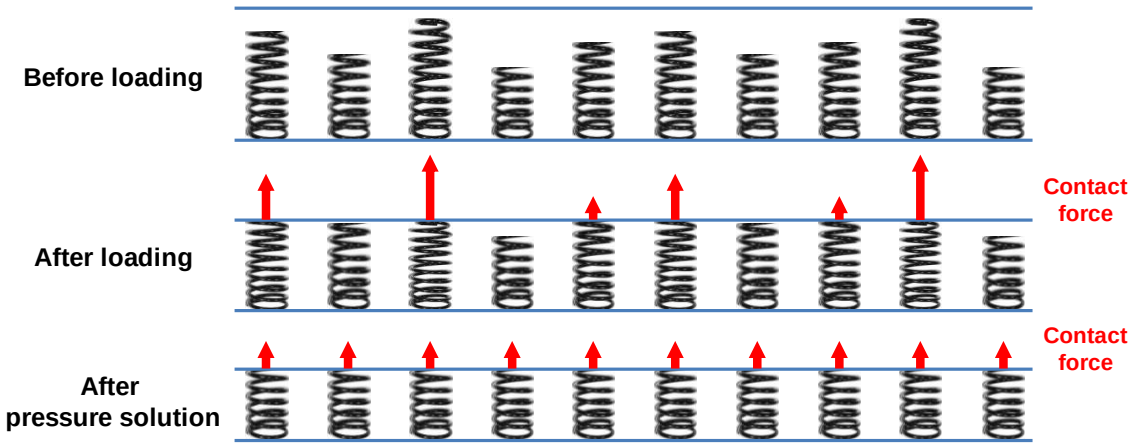


Figure 3.9 Changes in coordination number and contact forces: Physical explanation. A single layer of springs of different height is loaded by a flat plate. Thereafter, springs experience force-dependent size reduction.

| | (a) | (b) | (c) |
|---|---|---|---|
| | Before dissolution | At minimum $k_{min}$ | At the end of simulation |
| Contact density | 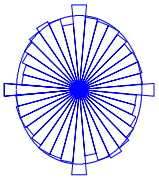 | 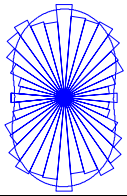 | 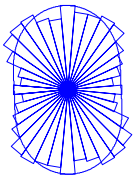 |
| Average normal contact forces (Scale=1) | 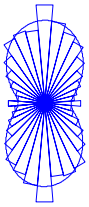 | 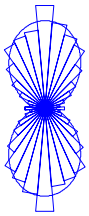 |  |
| Average tangential contact forces (Scale~0.1) | 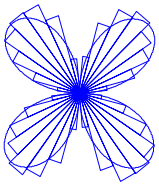 | 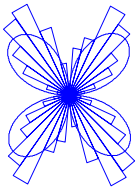 | 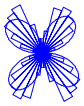 |
| Equivalent global stress ratio k | 0.49 | 0.36 | 0.49 |

Figure 3.10 Polar plots of internal micromechanical parameters before dissolution, at minimum equivalent global stress ratio $k_{min}$, and at the end of dissolution (Case: 2D confined, $dR/dt = \alpha \cdot F_N$ and HR=0%).

### 3.5 Conclusions

Pressure solution in sediments was simulated using the discrete element model by gradually decreasing the particle size proportional to the contact forces. Salient findings follow:

- Strong force chain formation/buckling and higher porosity inside the localization band, displacement discontinuities along the band, and temporal $k_0$ drop and recovery indicate the localization is a shear localization band accompanied by shear failure.

- A stronger contact force chain along the localization band may lead to more pressure solution along the shear localization.
- Among particles outside of the shear localization zone, a homogeneous fabric of contact force chains begins to form as the shear localization becomes visible.
- The $k_0$ decreases as dissolution progresses. After reaching its lowest value, $k_0$ gradually recovers. Shear localization starts to be visible when $k_0$ starts to recover.
- The coordination number increases and the mean contact force decreases during pressure solution simulation.
- Shear localization and horizontal stress reduction/recovery are observed various simulation conditions (i.e., 2D vs. 3D, constant stress vs. under near surface condition, different dissolution rates, and different degree of sediment friction), which indicate that this phenomena is an inherent self-leading event, not influenced by geometric conditions.

# CHAPTER 4

# HYDRO-CHEMO-MECHANICAL COUPLING: LOCALIZED MINERAL DISSOLUTION

## 4.1 Introduction

Mineral dissolution and re-precipitation play important roles in the chemical weathering of soils and rocks, and typically involve changes in mineralogy towards a more stable composition within a given geologic environment. Layering and discontinuities, state of stress, changes in fluid chemistry and gravity-dominated flow contribute to the development of preferential flow paths in sediments and rocks (Gillieson 1996, Criss et al. 2008, Boggus and Crawfis 2009). Vertical tubes are initiated by infiltration, while horizontal tubular cavities result from underground water flow (Ford and Williams 2007). Geological strata that contain carbonates, evaporates, and salts are particularly prone to dissolution in a high fluid advection system. Dissolution is relatively slow in nature, however, human activity can suddenly move natural systems far from quasi-equilibrium; for example, injected fluids can dramatically change the natural pH and pumping can accelerate advective transport (Veni et al. 2001, Hunt 2007).

Dissolution is the cause of sinkholes and settlements in karst regions and calcareous terrains (Waltham 2009). Accelerated dissolution rates caused by high hydraulic gradients undermine the performance of dams by increasing uplift pressure and accelerating seepage and piping (Dreybrodt et al. 2002, Gutiérrez et al. 2003, Payton and Hansen 2003). The dissociation of load-bearing gas hydrate leads to instability in sediments and has been considered the cause of marine landslides (Rothwell et al. 1998, Vogt and Jung 2002, Sultan et al. 2004a, Freij-Ayoub et al. 2007). Geologically-stored $CO_2$ will acidify pore water and cause mineral dissolution, which may lead to porosity

and mineralogy changes, settlement, and tensile fracturing of the cap rock (He et al. 2003, Watson 2004, Renard et al. 2005, Le Guen et al. 2007, Espinoza et al. 2011). Finally, the consequence of dissolution extend beyond geosystems; for example, dissolution is one of the main causes of natural deterioration of engineering materials, such as cement concrete by acid rain (Okochi et al. 2000, Xie et al. 2004), and demineralization makes bones porous and vulnerable to brittle fractures (Marcus et al. 2009).

Dissolution patterns vary. Homogeneous dissolution prevails in systems where the rate of advective transport exceeds the reaction rate. Previous studies reveal that particle-scale homogeneous dissolution affect both the small and large-strain properties of sediments (Chapter 2): a distinct "honeycomb fabric" emerges (Shin et al. 2008, Shin and Santamarina 2009), vertical displacement and void ratio increase (Fam et al. 2002, Shin et al. 2008, Shin and Santamarina 2009, Truong et al. 2010), the value of $k_0$ decreases often to $k_a$ before it recovers (Shin and Santamarina 2009), shear wave velocity decreases and attenuation increases (Fam et al. 2002, Truong et al. 2010), and the peak friction angle decreases (Fam et al. 2002).

Preferential or localized dissolution may be triggered by pre-existing discontinuities and the heterogeneous distribution of soluble materials. It can also emerge as a coupled hydro-chemo-mechanical effect in systems that experience high reaction rates (Daccord et al. 1993, Fredd and Fogler 1998). The geomechanical implications of localized dissolution in sediments have not been investigated. The following sections explore localized dissolution in sediments using a combined experimental and numerical research approach.

### 4.2 Experimental study

Dissolution tests are performed by flowing 1 molar solution of acetic acid $CH_3COOH$ through a calcareous sandy sediment from the Atlantic coastal plains in Georgia, USA ($D_{10}$=0.25mm; $D_{50}$=0.8mm; passing sieve #10 and retaining on sieve #100. Composition: 52% calcite, 47% quartz, and trace of clay minerals. Note: preliminary tests performed with hydrochloric acid and EDTA were abandoned due to gas generation, changes in soil behavior, or corrosiveness). The sediment is compacted in a zero-lateral strain cell (n=0.7; Stainless steel cell, ID=100mm - Figure 4.1). The reactive fluid is kept in the inlet tank at a fixed pressure. Inlet and outlet boundaries have a dense groove pattern beneath porous stones to ensure even 1D flow. Bender elements are installed in the bottom plate and top cap to record shear wave propagation and an LVDT is used to measure the top cap settlement.

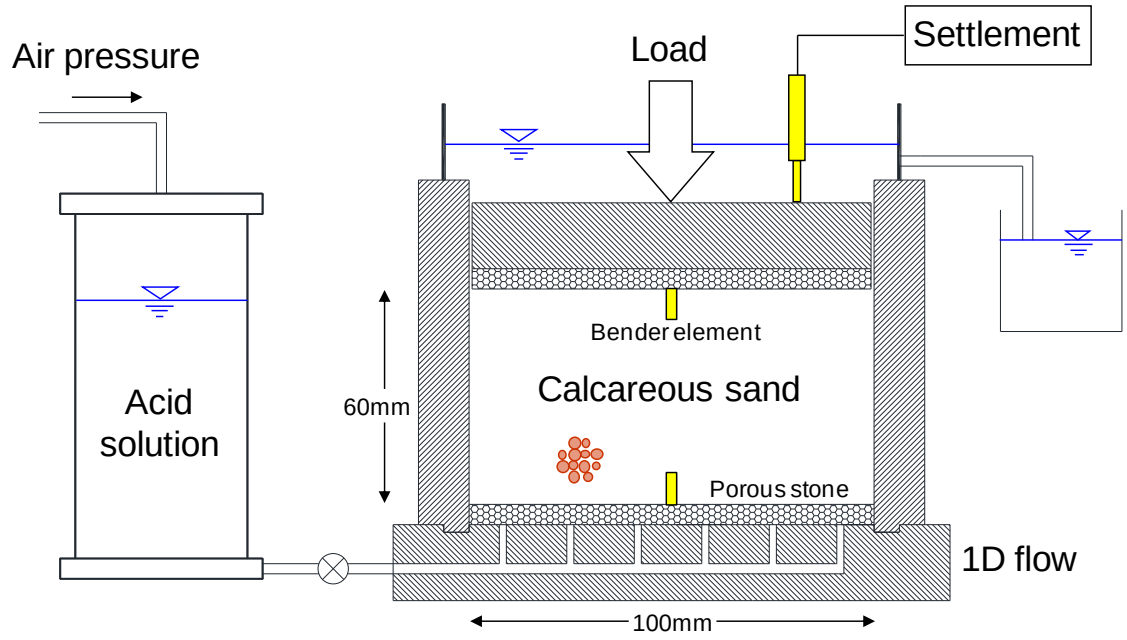


Figure 4.1 Study of dissolution in modified oedometer instrumented with bender elements. 1D flow-through enforced at constant inlet fluid pressure.

*Procedure.* After placing the dry calcareous sand in the cell, 20 pore volumes of tap water are passed through the sediment under a 400 kPa load. The sediment is allowed to equilibrate under the 400kPa vertical load for 72 hours. The acidic solution is injected from the bottom port at a constant inlet pressure of 20 kPa; effluent is collected from the top cap. After 25 pore volumes of acid flow, the test is terminated by flushing the sediment with fresh water (15 pore volumes). Additional loading is applied to explore the post dissolution compressibility. Finally, the sediment is carefully extruded from the cell and subject to visual inspection, tomographic imaging, and mineral analysis.

*Preliminary observation: Changes in waveforms.* The cascade of shear wave signals gathered during dissolution at constant vertical stress ($\sigma_v$=400kPa) is presented in Figure 4.2a. Shear waves propagate vertically and are horizontally polarized. There are gradual changes in overall waveforms, both in polarity of the first arrival as well as coda content. This indicates significant structural changes inside the sediment at the wavelength scale which in this case is in the order of centimeters. Shear wave velocities are computed and plotted in Figure 4.2b using arrival times from signals in Figure 4.2a and travel length from the recorded settlement data. The S-wave velocity initially increases as early dissociation enhances coordination number; eventually interparticle coordination drops as dissolution progresses and so does the S-wave velocity.

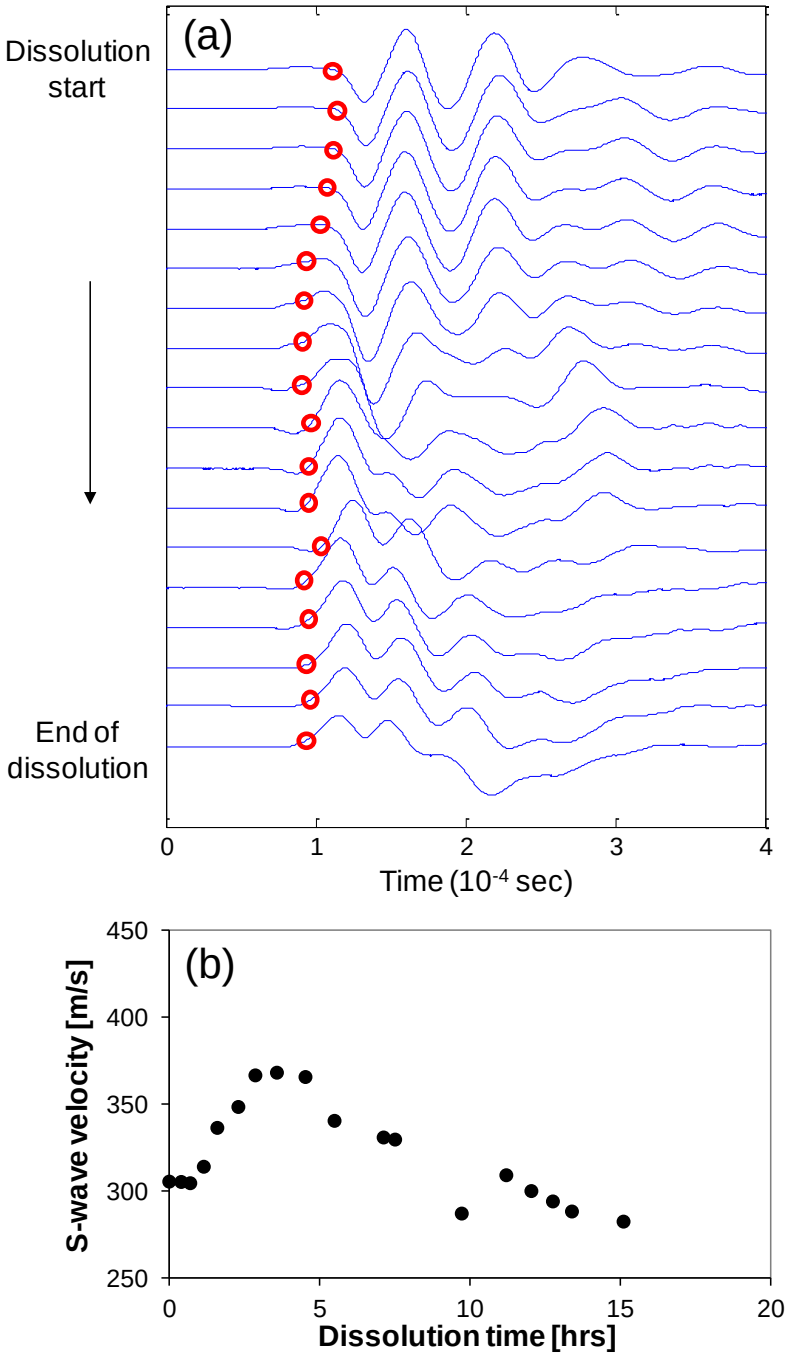


Figure 4.2 Evolution of shear wave signals during dissolution at constant vertical stress ($\sigma_v$=400kPa). (a) Cascade of shear wave signals during dissolution (Note the change in polarity). (b) Shear wave velocities computed using signals in pane-a versus dissolution time.

*Post-test Inspection: Dissolution Localization.* The extruded sediment at the end of the test exhibits light cementation and preserves its structure. High resolution 3D tomographic imaging (Siemens Biograph TruePoint PET-CT – Emory) and a 1D top-down X-ray plate (Dage X-Ray XD7600NT – GT) reveal the presence of low-density vertical fingers or tubes within the sediment (Figure 4.3). Some are fully formed from inlet to outlet, while others appear as abandoned paths. There are significant density differences between pipes and stable parts (2-to-1 X-ray absorption ratio).

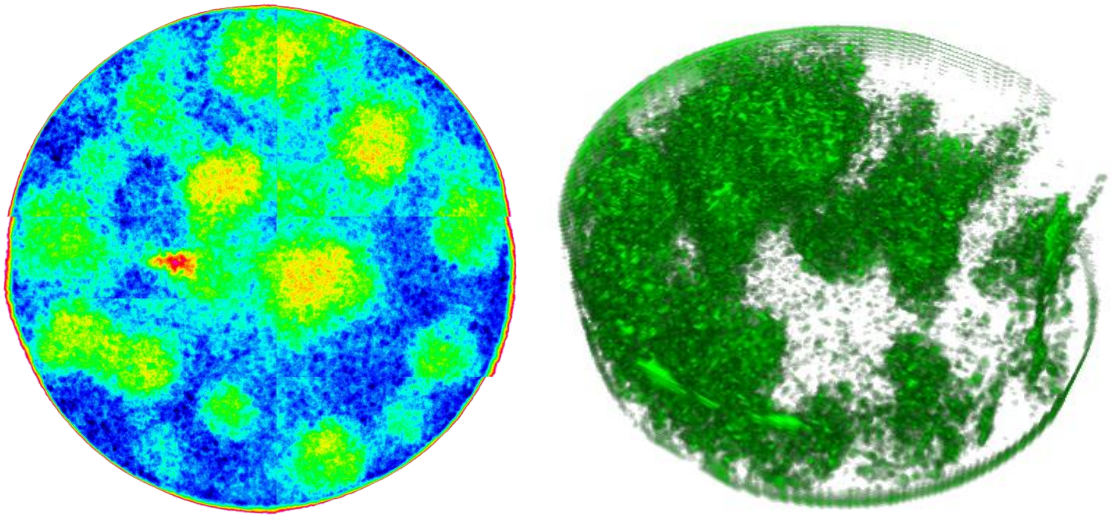

(a) (b)

Figure 4.3 Post-dissolution imaging. (a) 2D X-ray image. (b) 3D X-ray tomographic image. Both images show localized dissolution of the calcareous sand.

The localized dissolution structure is confirmed by gradually shaving sediment layers from the top. Dark color patches in Figure 4.4 correspond to fingers which are surrounded by light colored sediment. Extensive dissolution occurred near the inlet boundary at the bottom of the sediment (Figure 4.4f). Dissolution localizes in the form of pipes away from the inlet port; the number of pipes decreases towards the top, and only two dissolution pipes reach the outlet (Figure 4.4a).

(a) Top (b) 30mm from bottom

(c) 23mm from bottom (d) 15mm from bottom

(e) 10mm from bottom (f) Bottom

Figure 4.4 Specimen dissection by successive layer removal. Slices at various depths show localized dissolution of carbonate. Note: Light color is the sand with both carbonate and quartz. The dark color shows the non-soluble quartz grains that remain after dissolution.

*XRD Analyses: Selective Dissolution.* Samples gathered from the pipes and the surrounding medium are analyzed using X-ray diffraction. The mineralogy of pipes is mainly quartz (Figure 4.5a), while the background medium consists of quartz and calcite (Figure 4.5b). The absence of calcite in pipes is further confirmed by sampling pipe materials followed by acid dissolution loss test: calcite component is completely removed from the matrix along the pipes. In contrast, most of the calcite content is preserved in the stable part, where the calcite content changed from the initial value of 52% to 47% after the dissolution test.

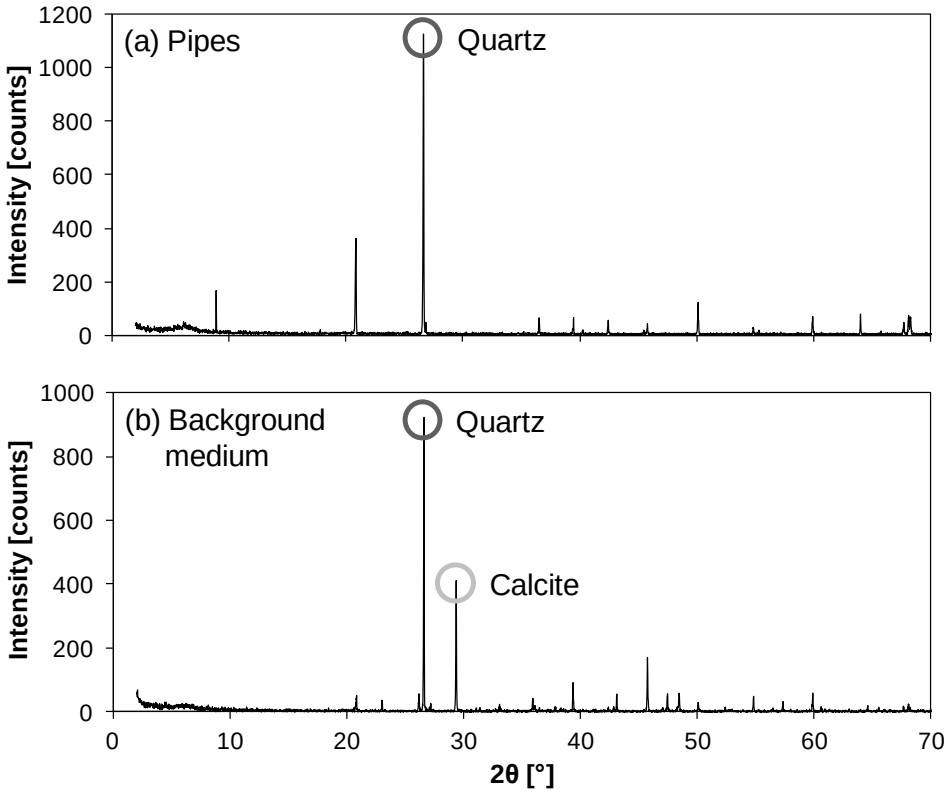


Figure 4.5 Mineral composition - XRD spectra for (a) non-soluble quartz grains remain in pipes after acid flow, and (b) the carbonate sand.

### 4.3 Discrete Element Simulation

The discrete element code PFC is used to study the geo-mechanical implications of localized dissolution both in 2D and 3D conditions (Cundall and Strack 1979). The simulation environment, summarized in Table 4.1, is based on a two dimensional packing of 11272 disks in 2D, and 9167 spheres in 3D. In both cases, grains are held under zero lateral strain conditions $\varepsilon_h=0$ with no friction against lateral boundaries. Rotational resistance is applied by hindering the rotation of randomly selected grains to simulate particle angularity. The vertical stress is kept constant during dissolution using numerical servo-control function. The position and size of vertical pipes are predefined in the sediment (Figure 4.6). Dissolution is simulated by gradually decreasing the size of soluble particles over time. The parametric study considers 2D and 3D configurations. The amount of soluble particles within the pipes is SF=50%, and the ratio of particles with hindered rotation is either HR=0% or 80%.

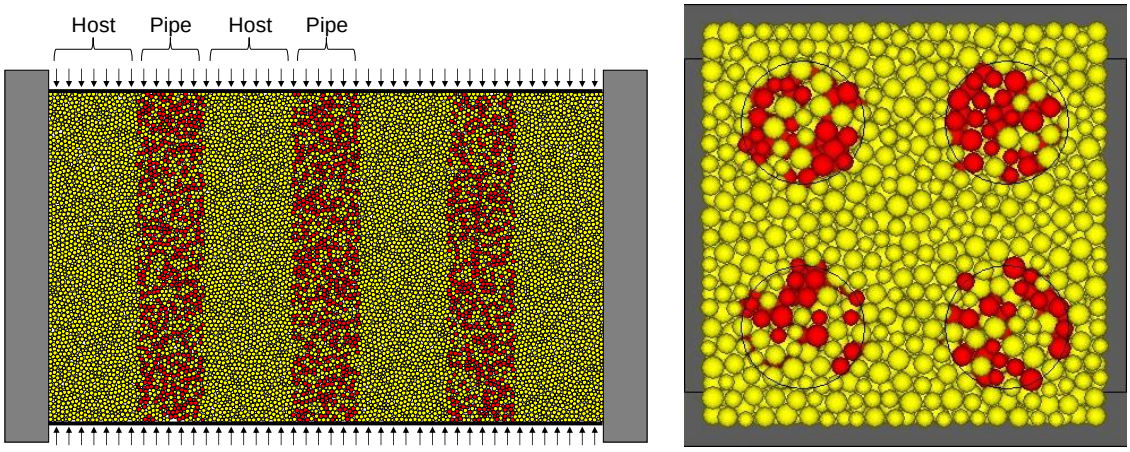


(a) 2D: Side view (b) 3D: Top view

Figure 4.6 DEM simulation study – 2D and 3D configurations. Dissolvable particles (dark color) are randomly distributed within parallel pipes (fraction of soluble particles in pipes SF=50%).

Table 4.1 DEM simulation environment

| | Properties | 2D | 3D |
|---|---|---|---|
| Particle properties | Particle size distribution | Uniform size distribution ($R_{min}$=0.3mm, $R_{max}$=0.45mm) | Uniform size distribution ($R_{min}$=1 mm, $R_{max}$=1.5 mm) |
| | Number of particles | 11272 disks | 9167 spheres |
| | Particle density | 2650 kg/$m^3$ | 2650 kg/$m^3$ |
| | Contact model | Linear contact model<br>-Normal stiffness kn =$10^8$ N/m<br>-Shear stiffness ks = $10^8$ N/m | Hertzian contact model<br>-Shear modulus = $2.9\times10^9$ Pa<br>-Poisson's ratio = 0.3 |
| | Inter-particle friction | 0.5 | 0.5 |
| | Hindered rotation HR | 0% and 80% | 0% and 80% |
| Boundary conditions | Initial cell size | (Height × Width)<br>6 cm × 10 cm | (Height × Width × Length)<br>5cm × 5cm × 5cm |
| | Vertical load | 100 kPa (during dissolution) | 100 kPa (during dissolution) |
| | Lateral boundaries | Zero strain | Zero strain |
| | Particle-to-wall friction | 0 | 0 |

Table 4.2 Parametric study

| Simulation dimensions | Fraction of soluble particles in the pipes SF | Hindered rotation HR |
|---|---|---|
| 2D | 25% | 0% and 80% |
| | 50% | 0% and 80% |
| 3D | 50% | 0% and 80% |
| | 100% | 0% and 80% |

*Normalized vertical displacement*. While dissolution takes place in pipes only, sediments settle fairly linearly with the normalized size reduction $\Delta R/R_0$ of soluble grains SF, at least during the early stages of dissolution until the normalized size reduction reaches $\Delta R/R_0$ =50% (2D and 3D simulations - Figure 4.7a&d and Figure 4.8a&d). Sediments with high interlocking, i.e., HR=80%, experience lower vertical displacement. Differences in vertical displacement due to hindered rotation HR are more significant in 3D simulations possibly due to higher coordination. A higher soluble fraction SF in pipes leads to larger settlements.

*Porosity.* Porosity increases during dissolution particularly within pipes (Figure 4.7b&e and Figure 4.8b&e). Sudden collapse events in "angular" systems are accompanied by changes in porosity (HR=80%) (Figure 4.7e). Interlocked sediments settle less and experience higher increase in porosity.

*Equivalent global stress ratio* $k_0 = \sigma_h/\sigma_v$. The horizontal stress increases in rotation-free sediments (HR=0%) (Figure 4.7c&f and Figure 4.8c&f). However, the equivalent global stress ratio $k_0$ decreases in highly interlocked sediments (HR=80%) during early stages of dissolution, and recovers after reaching a minimum value, which is a trend similar to homogeneous dissolution results (Chapter 2). The soluble fraction in pipes affects the global stress ratio $k_0$: it remains low after dissolution when the soluble fraction is small but it may recover when the soluble fraction is large (Figure 4.8c&f).

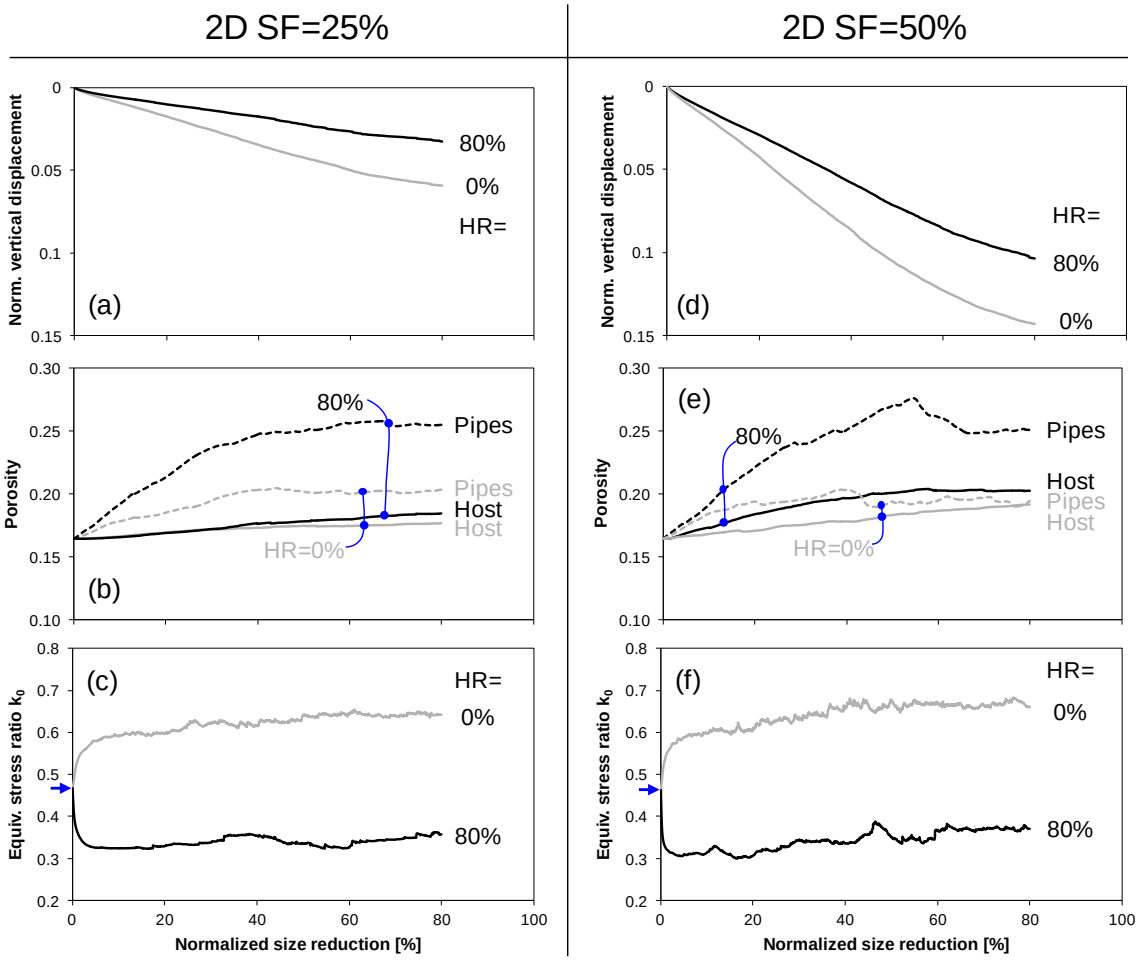


Figure 4.7 Sediment response during localized dissolution under zero lateral strain – 2D simulations. (a)&(d) Normalized vertical displacement. (b)&(e) Porosity. (c)&(f) Equivalent global stress ratio $k_0$. Note: grains in the "host" medium experience no dissolution while SF=25% and 50% of grains in pipes dissolve.

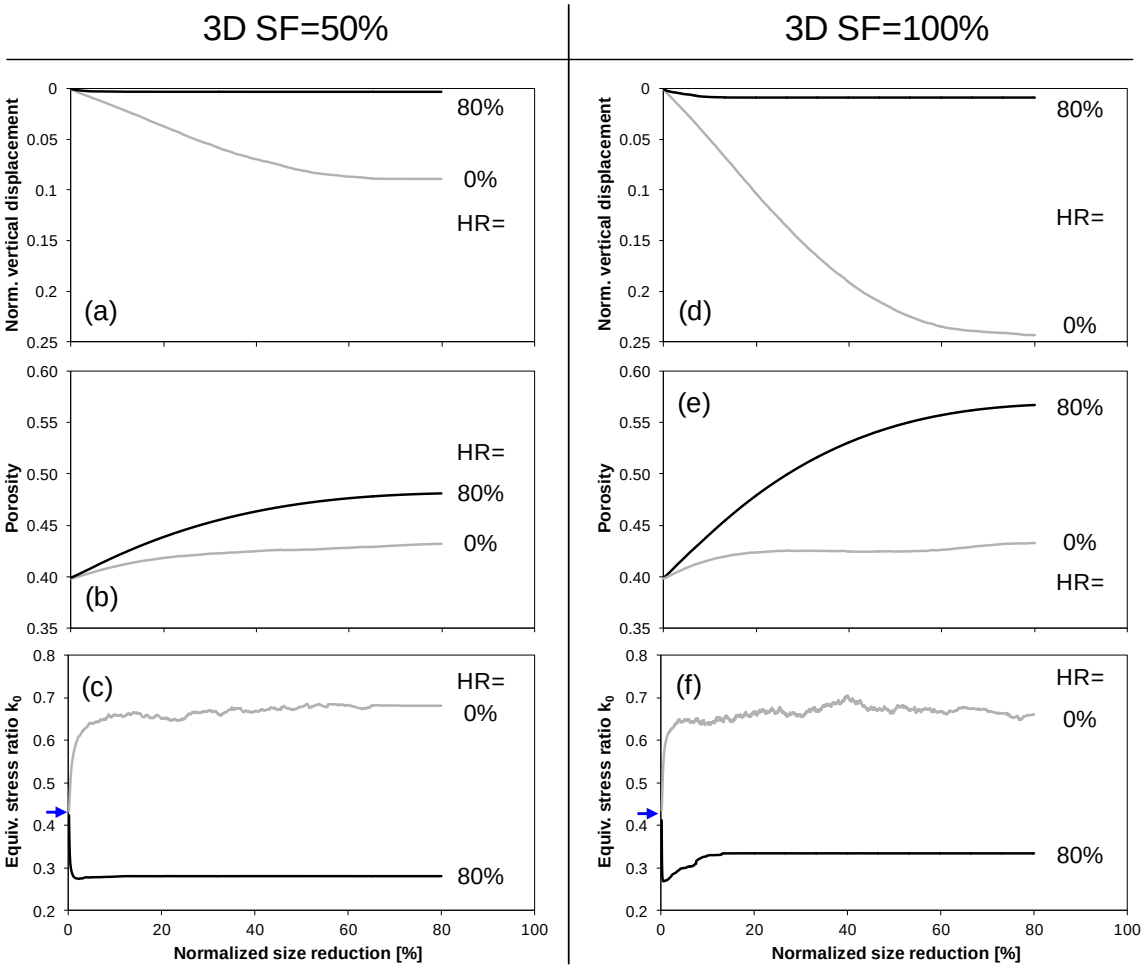


Figure 4.8 Sediment response during localized dissolution under zero lateral strain 3D simulations. (a)&(d) Normalized vertical displacement. (b)&(e) Global porosity. (c)&(f) Equivalent global stress ratio $k_0$. Note: grains in the "host" medium experience no dissolution while SF=50% and 100% of grains in pipes dissolve.

*Contact force chains*. Marked force chains are preferentially vertical away from pipes (Figure 4.9b), yet, they are preferentially horizontal within pipes. In fact, horizontal contact forces inside pipes prevent the buckling of granular columns in the surrounding stable zones. At large dissolution, stable zones collapse towards the softer pipes, and structural differences between the two zones become less prominent (Figure 4.9c).

*Horizontal and vertical (equivalent) stress changes in pipes and in the host sediment.* Vertical forces increase rapidly in the host medium when dissolution starts in pipes as the vertical load is transferred to the host medium (Figure 4.10). In the meantime, there is principal "equivalent" stress rotation in pipes (Figure 4.10). Note that $\sigma_h|_{pipe} \approx \sigma_h|_{host}$ to satisfy equilibrium. The equivalent stress anisotropy $\sigma_h/\sigma_v$ is higher in pipes and the host medium when rotation is hindered (HR=80%). The peak equivalent global stress ratios reach the Coulomb failure condition in both the pipes and the host medium. The equivalent stresses are calculated within selected regions in pipes and the host medium; global equilibrium with the applied vertical stress 100kPa is verified in all cases.

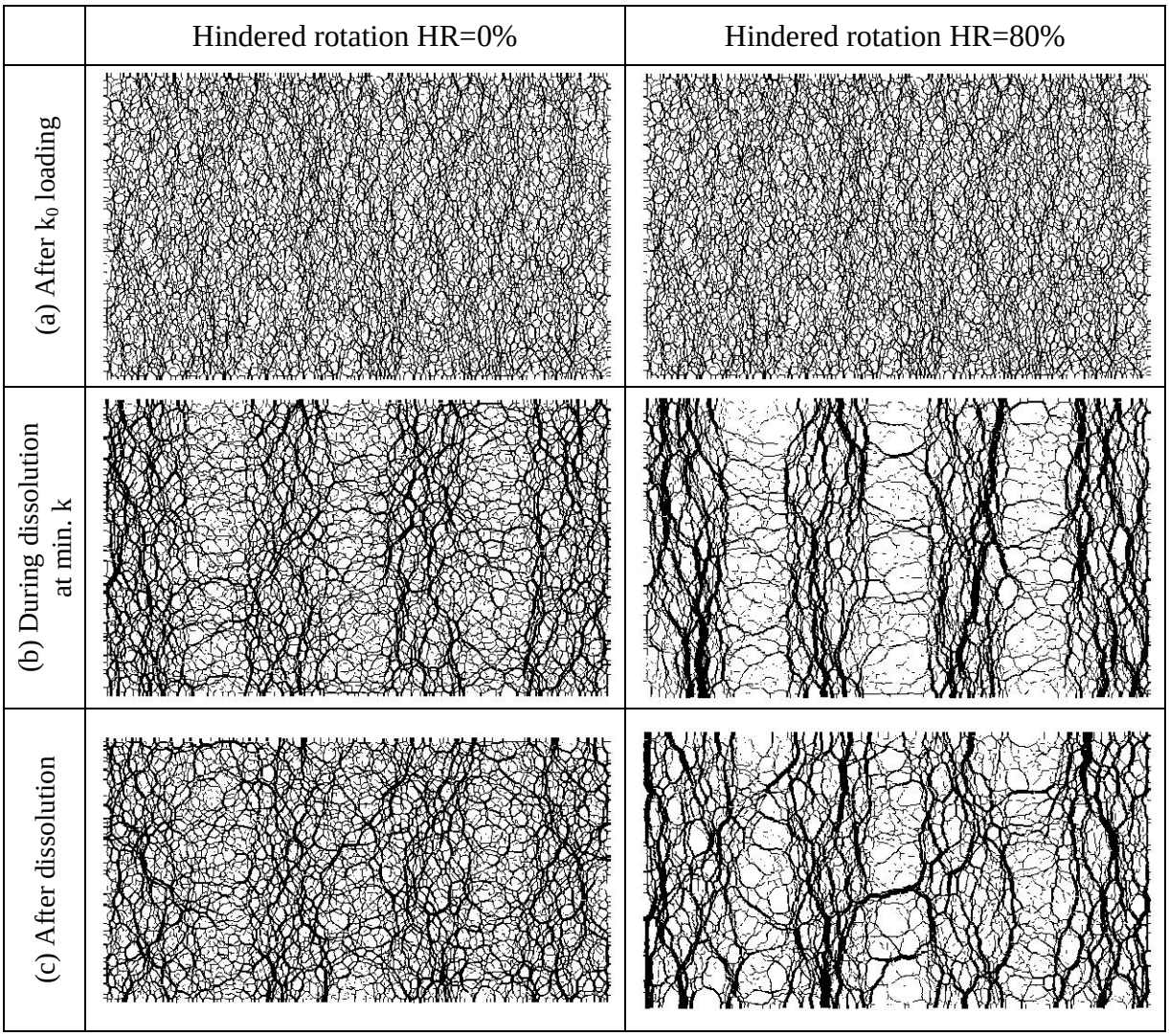


Figure 4.9 Evolution of contact force chains during localized dissolution along pipes (2D and SF=50% within the pipes). (a) After $k_0$ loading and before dissolution. (b) During dissolution at minimum equivalent global stress ratio k. (c) After complete dissolution. Note: network of contact-to-contact lines are drawn with thickness proportional to contact force.

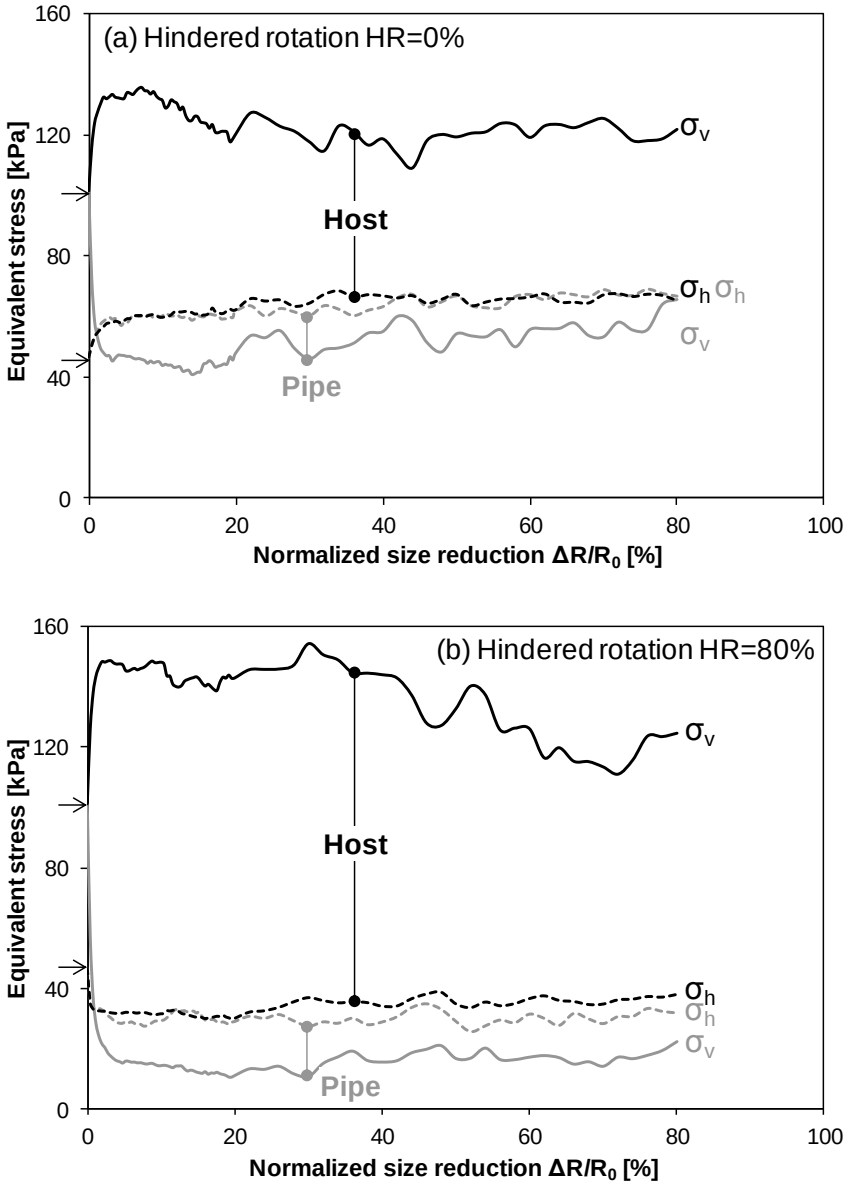


Figure 4.10 Equivalent horizontal $\sigma_h$ and vertical $\sigma_v$ stress changes in pipes and in the host medium during dissolution (2D; SF=50% within the pipes).

### 4.4 Discussion and implications

Sediments are heterogeneous in spatially varying porous media. Therefore, water flow in sediments inherently localizes along the most conductive flow paths even in the absence of chemical reactions (Jang et al. 2011). Inherent flow localization couples with reactive fluid flow to cause pipe formation. Three rates control the evolving topology of dissolution: chemical reaction rate, advective mass transport rate, and diffusive transport rate. The corresponding scales can be compared in two dimensionless numbers Damköhler number Da and Péclet number Pe:

$$\mathrm{Pe} = \frac{\nu l}{D} = \frac{\text{Advective transport rate}}{\text{Diffusive transport rate}} \tag{4.1}$$

$$\mathrm{Da} = \frac{\alpha l}{\nu} = \frac{\text{Reaction rate}}{\text{Advective transport rate}} \tag{4.2}$$

where $v$ [m/s] is the advection flow velocity, $l$ [m] is the characteristic length, $D$ [$m^2$/s] is the chemical diffusion coefficient, and $\alpha$ [1/s] is the mass exchange coefficient. Experimental and theoretical studies reveal the topology of dissolution patterns in terms of Pe and Da numbers (Hoefner and Fogler 1988, Fredd and Fogler 1998, Golfier et al. 2002): (a) compact dissolution is observed at high Da numbers and low Pe numbers (i.e. high reaction rate, low advection rate, and high diffusion rate); (b) uniform dissolution takes place when Da numbers are very low (i.e., the reaction rate is very slow, or the advection rate is very high); (c) Dissolution localization occurs at high Da numbers and high Pe numbers (i.e. high reaction rate, low diffusion rate, and moderate advection rate) and it is the result of positive hydro-chemical feedback. In this study, more compact dissolution was observed when inlet pressure was less than 10 kPa while clear localizations were attained with an inlet pressure 20 kPa (flow rate q=14 ml/min for 1M acetic acid solution.

*Implications: Fluid Pressure.* Localized dissolution pipes increase fluid flow, advance the fluid pressure front towards the outlet and lower the effective stress, increase the hydraulic uplift pressure (Figure 4.11), shorten the seepage length and heighten the vulnerability to piping and boiling. The fluid pressure at the tip of pipes $u_{tip}$ can be estimated as:

$$\frac{u_0 - u_{tip}}{u_0 - u_{exit}} = \frac{1}{1 + \frac{1-\lambda}{\lambda}\left(\alpha \frac{k_P}{k_H} + (1-\alpha)\right)} \tag{4.3}$$

where $u_0$ and $u_{exit}$ are inlet and outlet pressure, the tip is at a distance $\lambda L$ from the left boundary, the cross section of pipes is $\alpha A_T$ of the total area $A_T$, and $k_P$ and $k_H$ are the hydraulic conductivities in the pipe and host medium.

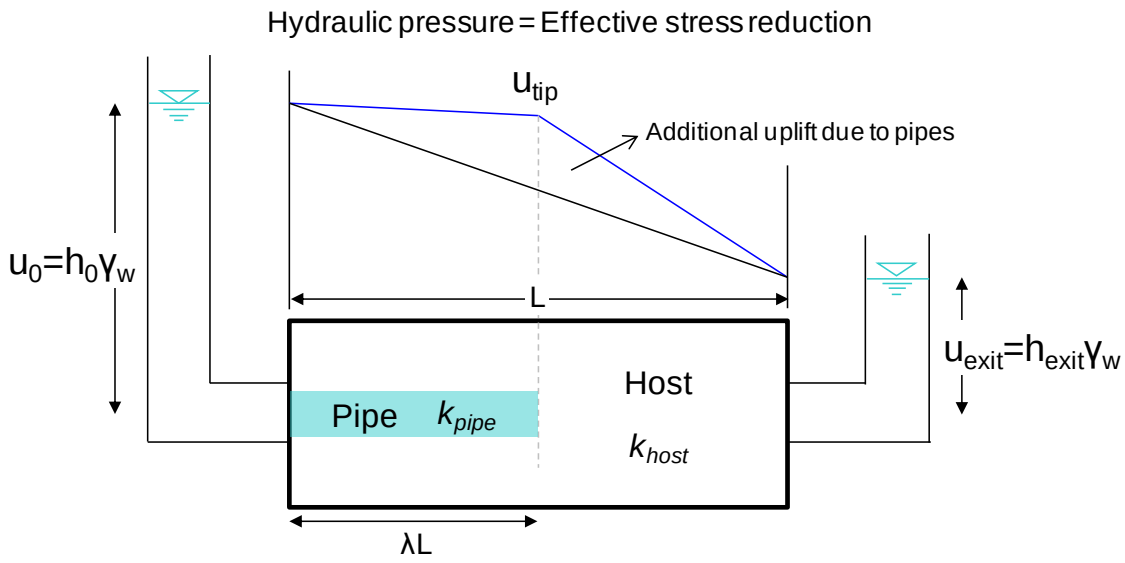


Figure 4.11 Effect of dissolution pipe formation on pore fluid pressure.

*Exclusion distance and pipe density.* The presence of a wormhole alters flow paths and hinders the formation of other wormholes or pipes nearby (see Figure 4.4). The exclusion distance decreases and the pipe density increase with increasing flow rate (Golfier et al. 2002, Cohen et al. 2008). Competition between wormholes for the available fluid means that longer wormholes can reach closer to the outlet and are able to transport more fluid, and thus grow faster than smaller ones (Buijse 2000), leading to the decrease in pipe density towards the outlet boundary as observed in Figure 4.4.

## 4.5 Conclusions

Hydro-chemo-mechanical coupling can lead to dissolution localization in soils, as observed in calcareous sands permeated with a reactive acid solution.

- Concurrent shear wave signals changes captured during dissolution under constant stress indicate the development of pronounced heterogeneity significant inside the sediment.
- Localized dissolution is corroborated through post-dissolution tomographic studies and specimen dissection. The number of pipes at a cross section decreases away from inlet port. While calcite is completely dissolved along pipes, virtually no calcite is dissolved in stable parts around pipes.
- Complementary discrete element simulations show that: the vertical displacement is quasi-linear relation with the progress of dissolution. Hindered rotation, i.e., a proxy for angularity and granular interlocking hinders vertical displacement.
- Porosity increases throughout the medium during dissolution, but it is larger in pipes.
- Similar to the case of homogeneous dissolution, localized pipe dissolution leads to the initial decrease of horizontal stress followed by a gradual recovery in angular-interlocked sediments.

- Marked force chains are preferentially vertical away from pipes, yet, they are preferentially horizontal within pipes. Horizontal contact forces inside pipes prevent the buckling of granular columns in the stable zones.
- Vertical forces increase rapidly in the host medium when dissolution starts in pipes. In the meantime, there is principal “equivalent” stress rotation in pipes. The peak equivalent global stress ratios reach the Coulomb failure condition in both the pipes and the host medium.

# CHAPTER 5

# EFFECT OF SHALLOW SUBSURFACE VOLUME CONTRACTION ON THE BEHAVIOR OF OVERLYING SOILS: DEM SIMULATION

## 5.1 Introduction

Underground construction causes ground loss and stress relaxation and inevitably ground movement (Attewell and Farmer 1974). Similarly, mining and the dissolution of carbonates may trigger ground subsidence, collapse/cave-ins, sinkholes, and subsurface regional softening (Bell et al. 2000, Cui et al. 2000, Li 2008). Ensuing surface and subsurface movements are a function of geometry (size, depth and volume loss) and soil properties. Deeper tunnels cause less surface settlement, but a wider settlement profile (Peck 1969, Ahmed and Iskander 2011). The settlement volume correlates with the ground loss or contracted volume (a "gap parameter" is used in tunneling practice to represent mass loss around tunnels during construction - Rowe et al. 1983, Lee et al. 1992). And, the surface settlement decreases as the soil stiffness increases (Bobet 2001).

Closed-form first-order estimates of surface settlements are based on Green's functions or influence functions for infinitesimal extraction elements (Fares 1987, Ren et al. 1987, Bahuguna et al. 1991, Lin et al. 1992, Sheorey et al. 2000). Empirical methods for the prediction of surface settlement typically assume a Gaussian-shaped settlement profile (Peck 1969, Mair et al. 1993, Fang et al. 1994, Li 2008). Other empirical methods use available data to train neural network models (Kim et al. 2001, Ambrozic and Turk 2003, Neaupane and Adhikari 2006). Numerical finite-element FEM simulations have been used as well to analyze surface and subsurface settlements and lateral soil movements (Lee et al. 1994, Rodriguez-Roa 2002). Compared to FEM, semi-empirical

methods require only a few parameters (Verruijt and Booker 1996, Loganathan and Poulos 1998, Bobet 2001, Park 2005).

Displacements induced by underground volume contraction negatively affects overlying infrastructure and nearby underground structures, for example: piles experience lateral deflection, bending moments, settlement, and abnormal load distribution (Chen et al. 1999, Jacobsz et al. 2004, Huang et al. 2009); lifelines are sheared and disrupted (Klar et al. 2005, Vorster et al. 2005, Klar et al. 2008, Marshall et al. 2010, Wang et al. 2011); buildings develop differential settlements and horizontal displacement (Burland et al. 2001, Yoo and Kim 2003); and adjacent tunnels may rotate and undergo asymmetric settlement (Cooper et al. 2001, Cooper et al. 2002).

This study takes advantage of discrete element simulations to gain particle-level insight on contact forces and local porosity changes around contracting volumes as a function of the sediment density, depth-to-inclusion size ratio, and friction angle.

## 5.2 Methodology

We use a two-dimensional discrete element code (PFC-2D) to create the simulation environment described in Table 5.1. Subsurface volume contraction is simulated by removing an inclusion size D made of grains size $d_0$ that is based in a laterally confined sediment with an open surface boundary (Figure 5.1). We select the linear contact model and assume no friction between grains and walls. Grain angularity and interlocking prevent grain rotation, thus, we capture non-circular particle shape by hindering particle rotation (Bardet 1994, Iwashita and Oda 1998, Suiker and Fleck 2004).

Two different initial densities where the percentage of particles with hindered rotation HR is varied between HR=0% and 80%. The loose packing is formed by air pluviation under 1g gravity, while the dense sediment is made by compaction. The inclusion depth z to diameter D ratio is varied between z/D=2 and 9. After equilibrium is reached, the

grains that fall within the "inclusion" are removed instantly. A total of 18 simulations are performed (Table 5.2).

Table 5.1 Discrete element 2D simulation environment.

| | Properties | Values |
|---|---|---|
| Disk | Radius of disks | Uniform size distribution ($R_{min}$=0.4 mm, $R_{max}$=0.6 mm) |
| | Number of disks | 10567 |
| | Mass density of disks | 2650 kg/m$^3$ |
| | Linear contact model | Normal stiffness $k_n = 10^8$ N/m |
| | | Shear stiffness $k_s = 10^8$ N/m |
| | Inter-particle friction | 0.5 |
| | Hindered rotation HR | 0%, 40%, 80% |
| Boundary conditions | Initial cell size | (Height × Width) 10 cm × 10 cm |
| | Vertical load | 100 kPa |
| | Zero lateral strain | |
| | Particle-to-wall friction | 0 |
| | Gravity | 1g |

Table 5.2 Parametric study.

| Initial density | z/D | Rotational hindrance (to simulate friction angle variance) |
|---|---|---|
| Dense (e=0.184) | 2 | HR= 0%, 40%, and 80% |
| | 5 | HR= 0%, 40%, and 80% |
| | 9 | HR= 0%, 40%, and 80% |
| Loose (e=0.242) | 2 | HR= 0%, 40%, and 80% |
| | 5 | HR= 0%, 40%, and 80% |
| | 9 | HR= 0%, 40%, and 80% |

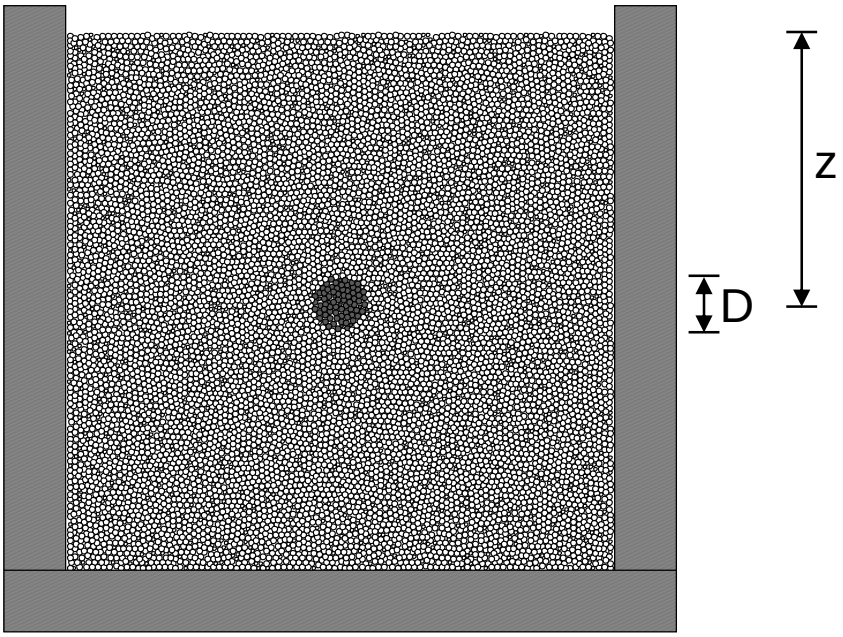


Figure 5.1 Initial model showing the inclusion depth z and size D. Grains in dark color are soluble (Case shown corresponds to z/D=5).

## 5.3 Results and analyses

**Grain flow and internal displacement field**

Grains flow to fill the cavity once the inclusion is removed, in agreement with the cohesionless nature of the sediment (Figure 5.2). Grains flow predominantly in the vertical direction in sediments with hindered rotation i.e., sediments with higher angularity and interlocking; conversely, horizontal flow towards the cavity gains significance when grains rotate freely, i.e. low friction angle. Displacements propagate from the contracted region towards the free surface within a fan-shaped zone above the cavity. As hindered rotation increases, the displacement field is limited to a smaller-angled fan and lower displacement magnitude take place (Figure 5.3). Movies of grain movements show grain flow in the form of porosity waves that propagate upward towards the free surface as a result of gravity and friction.

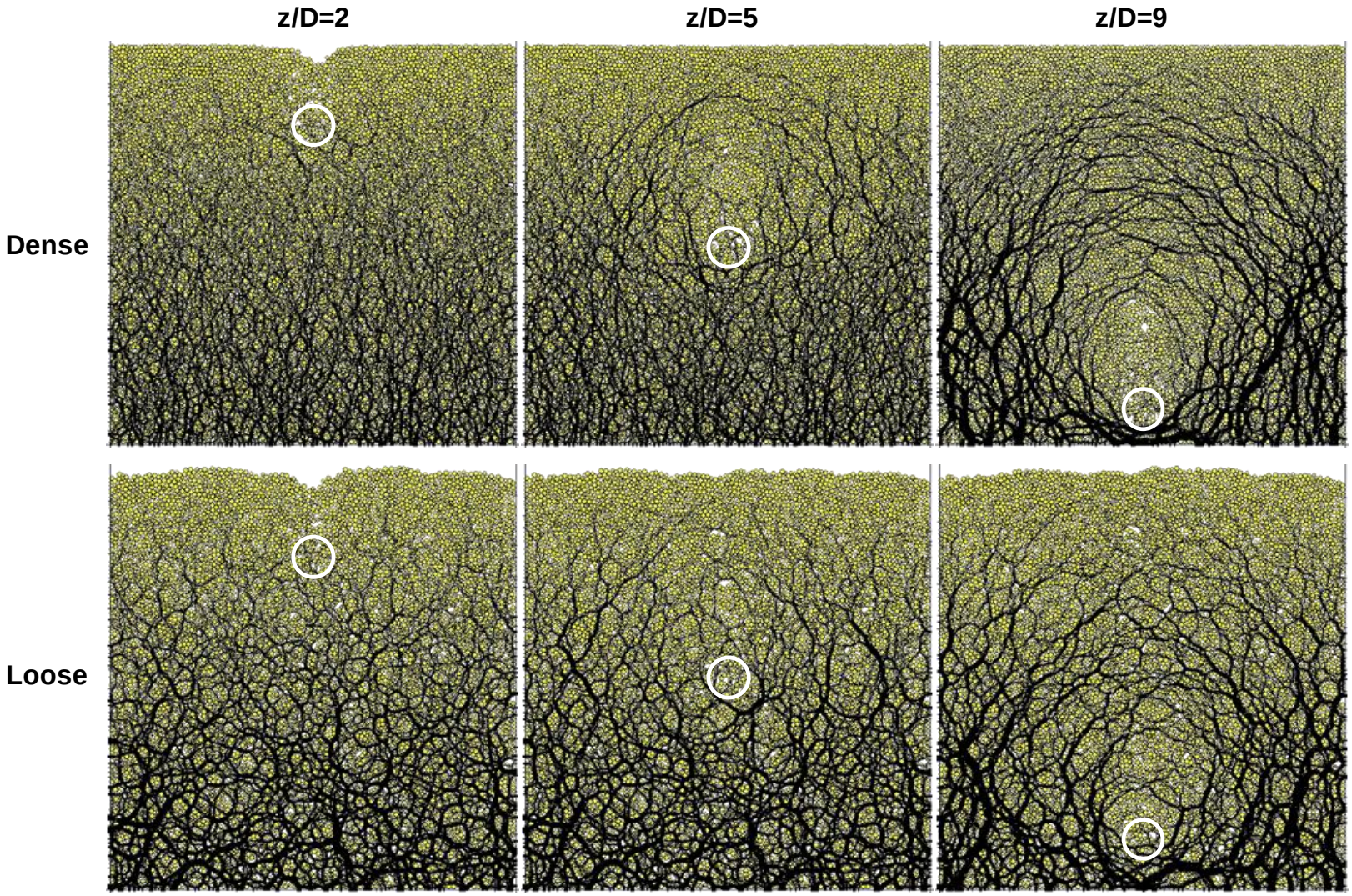


Figure 5.2 Contact force chains after dissolution (Hindered rotation HR=40%). The white circles indicate the original location and size of dissolvable inclusions. Notice large local porosity next to strong force chains.

**Contact force arching and "effective void"**

Grain flow is accompanied by contact force arch formation and collapse. Contact forces concentrate along the sides of the lost region and are most prominent in sediments with higher friction angle.

Grains in the re-filled cavity have small contact forces. Hence, there is a "ghost effective void" that is larger than the original inclusion size. Even small ground loss events mobilize friction/interlocking in the surrounding soil and cause pronounced force reduction within the inclusion.

The effective void is also more prominent for dense materials: they have an initially higher interparticle coordination that inherently leads to rotational frustration (Figure 5.2). While grains inside the effective void carry almost no vertical forces, they do contribute to prevent the buckling of granular arches around the effective void.

Porosity is high inside the effective void (Figure 5.2) especially in sediments with high interlocking (i.e., high hindered rotation HR), because friction hinders particle arrangement as grains flow to fill the void.

Stress arching extends towards the free surface under the gravity-dominated conditions imposed in these simulations. The final global contact force network elongates towards the free surface especially in sediments with higher interlocking.

There is a tendency for higher local porosity next to major force chains (Figure 5.2); indeed, large pores require force chains to arch around.

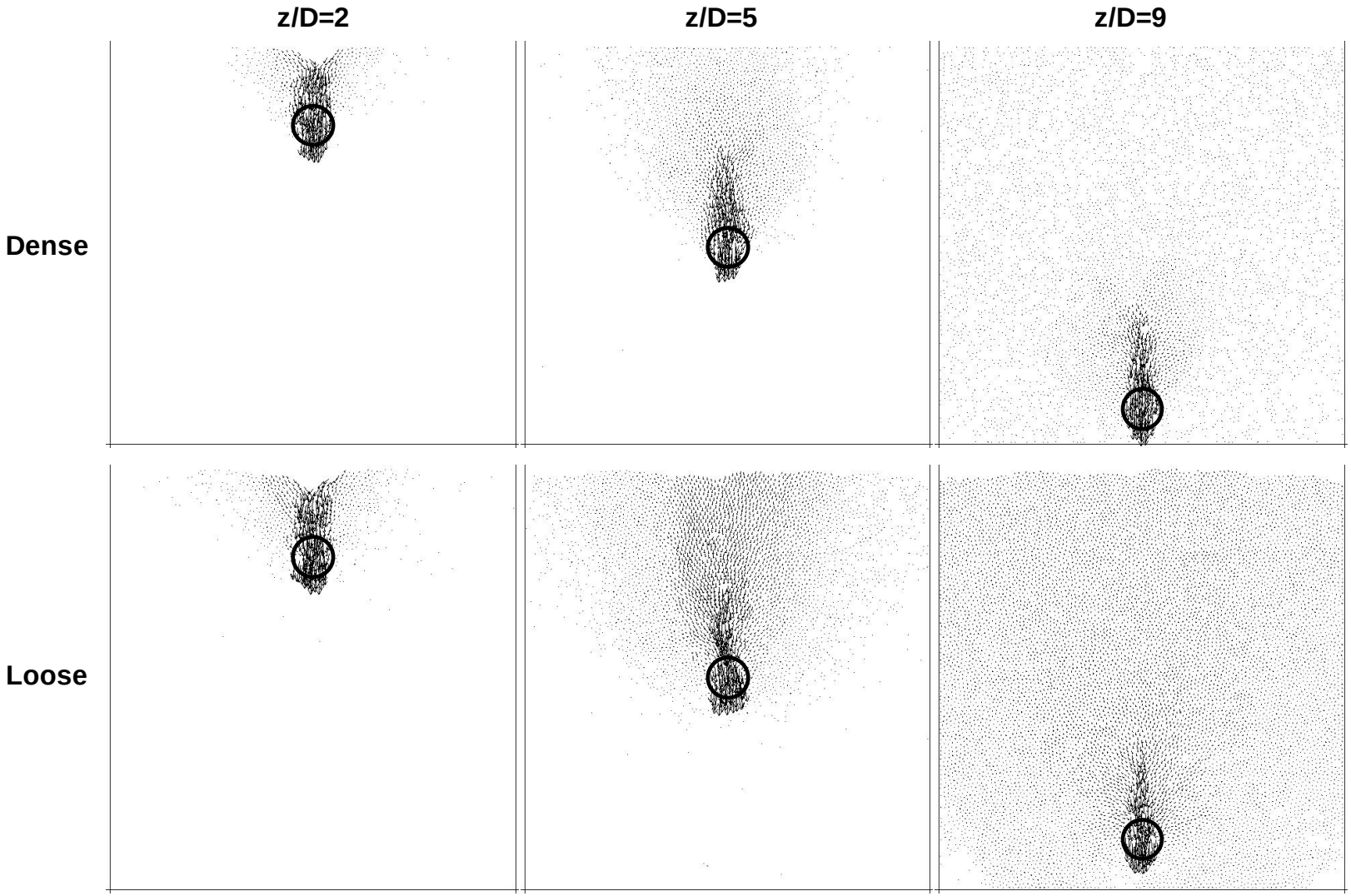


Figure 5.3 Displacement vectors after dissolution (Hindered rotation HR=40%). The black circles indicate the original location and size of dissolvable inclusions.

**Settlement**

A Gaussian function can be fitted to the observed surface settlement profiles, in agreement with large-scale field observation (Peck 1969). Deviations are more pronounced near the inflection (Figure 5.4). The maximum surface settlement $\delta_{max}$ (1) decreases with the depth-size ratio z/D, (2) it is relatively unaffected by interlocking or packing density for shallow inclusions z/D≤2, (3) however, denser or more interlocked sediments lead to lower peak settlement $\delta_{max}$ when inclusions are deep z/D≥5 (Figure 5.6a).

The affected "characteristic width" of the surface settlement profile" W is the standard deviation in the fitted Gaussian function. DEM results show that the effective width W increases with z/D and it decreases with friction/interlocking (Figure 5.3).

It is typically assumed that the volume per unit length or the area of surface settlement $A_S$ in the field is equal to the volume of ground loss $A_V$ around the tunnel. Our simulation results show that the ratio is $A_S/A_V<1$ for dense dilative sediments, and that it decreases with z/D and interlocking (Figure 5.6b); in these cases, there is clear gain in porosity above the ground loss region. On the other hand, contractive sediments with low friction can cause surface settlement volumes higher than the extracted volume $A_S/A_V$ and contraction increases with the normalized inclusion depth z/D (Figure 5.6).

Subsurface displacements at an elevation 1D above the crown of the vanishing volume are plotted in Figure 5.5. The peak vertical displacement $\delta^{1D}_{max}$ decreases slightly with z/D and when there is higher horizontal flow into the cavity, i.e., in deeper, looser, and less interlocked sediments (see displacement vectors in Figure 5.3).

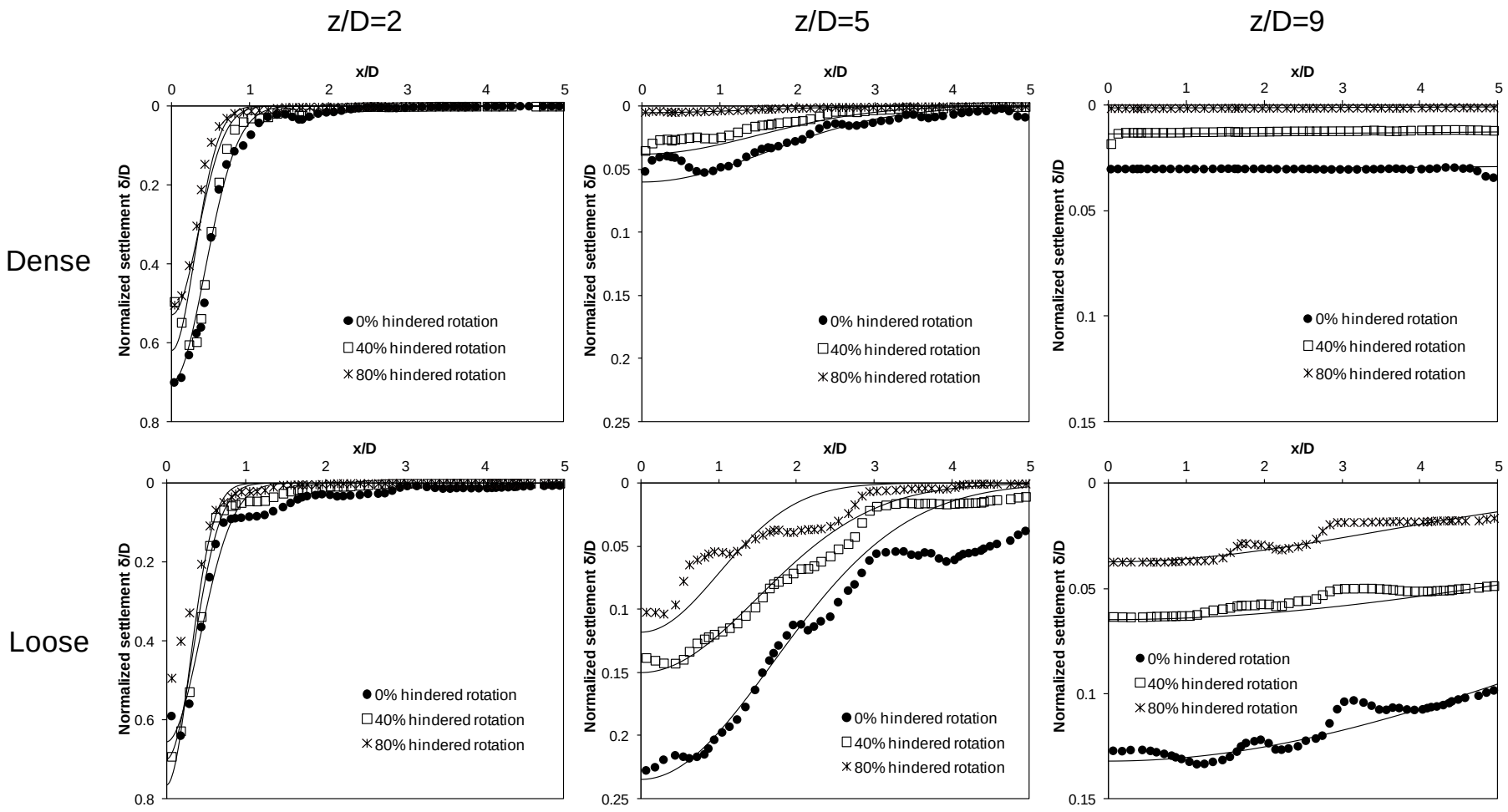


Figure 5.4 Surface settlement after dissolution. Results are folded at the centerline. The data are fitted with a Gaussian function.

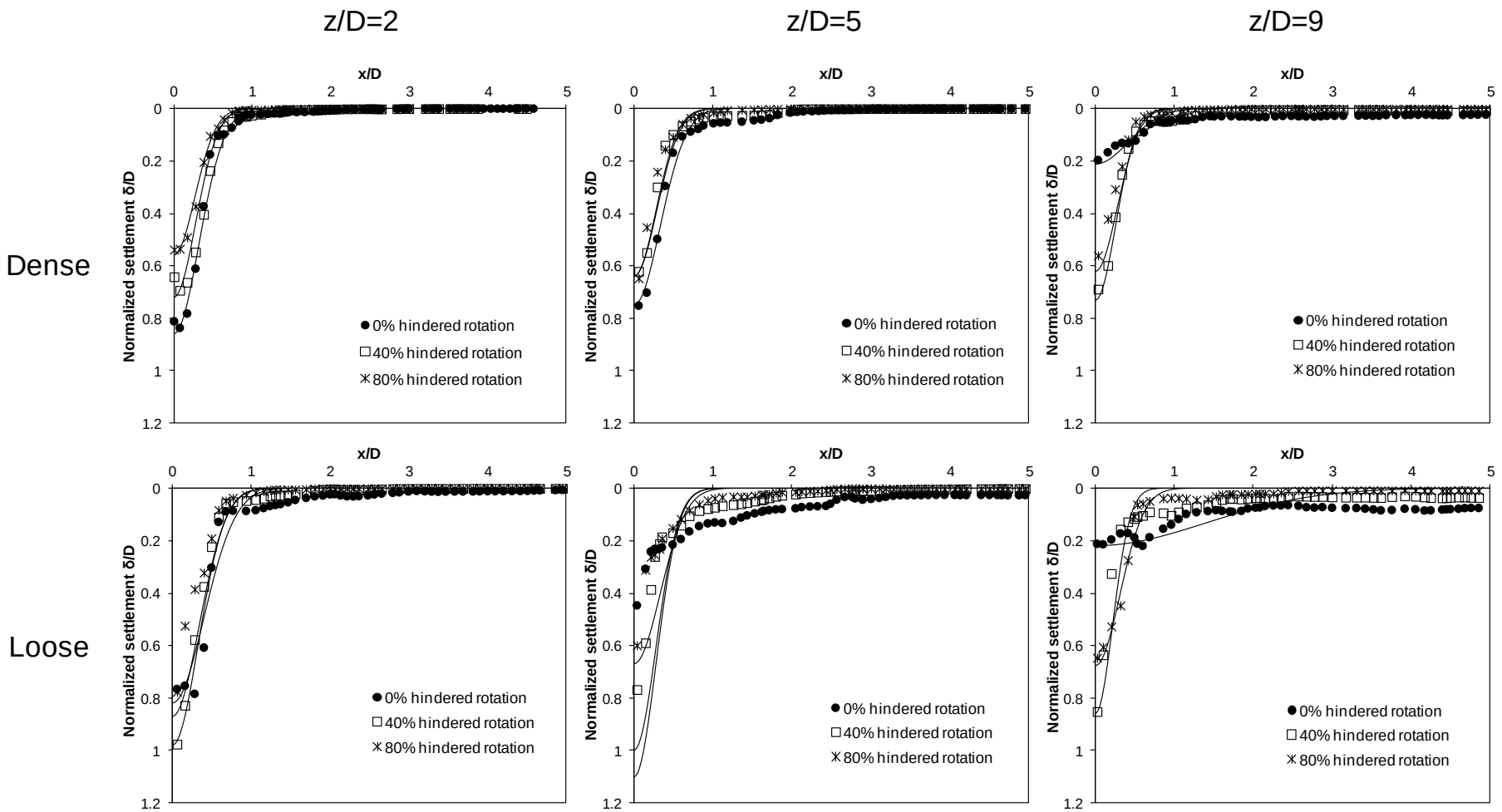


Figure 5.5 Vertical displacement at 1D above crown after dissolution. Results are folded at the centerline. The data are fitted with a Gaussian function.

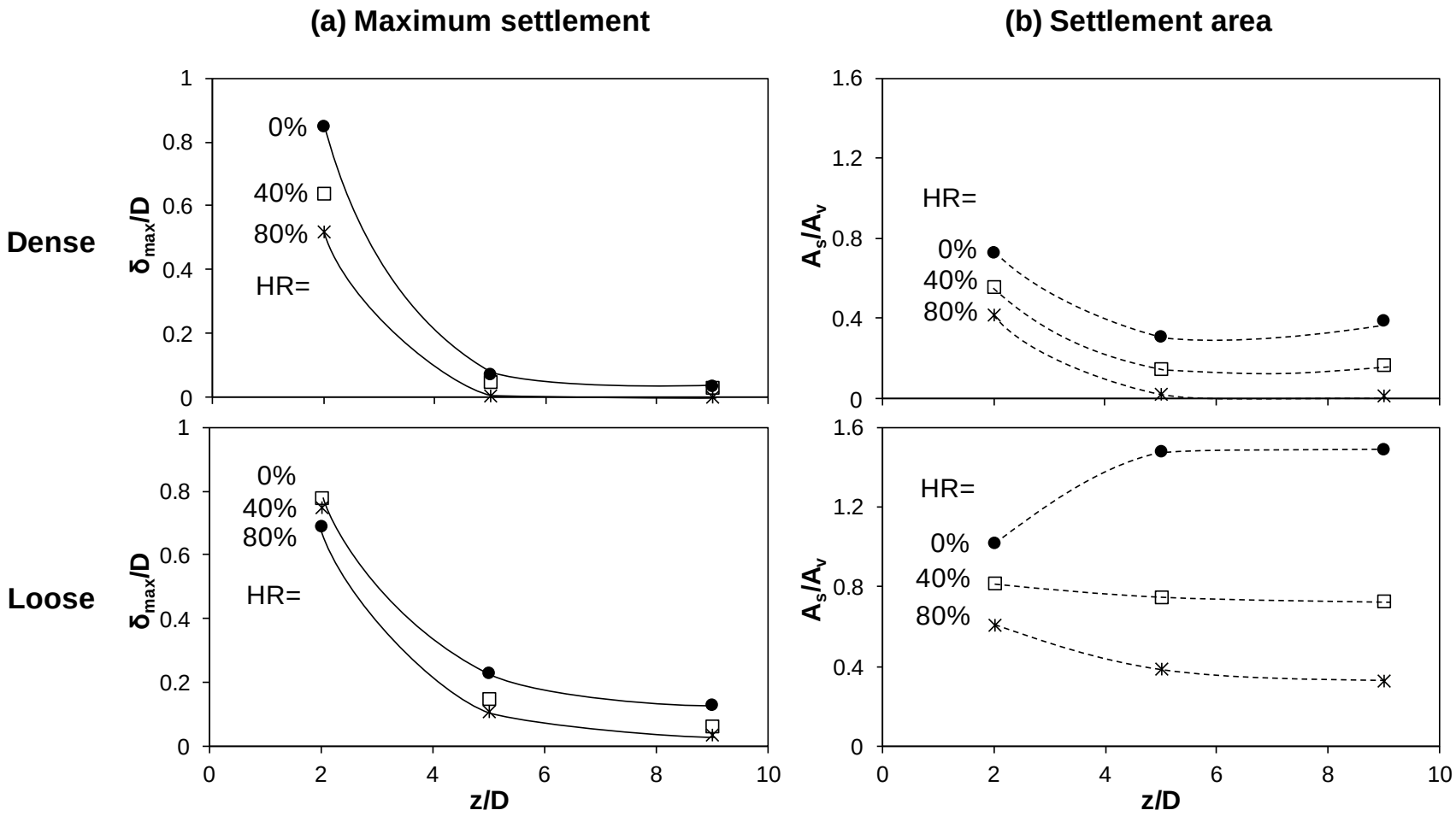


Figure 5.6 Surface settlement for subsurface cavity dissolution in dense and loose sediments. (a) Normalized maximum settlement $\delta_{max}$ to the inclusion diameter D. (b) Surface settlement volume $A_S$ normalized by the lost volume $A_V$.

## 5.4 Conclusions

Shallow subsurface volume contraction or ground loss affects overlying soils. Cavities are readily filled by surrounding grains that flow dominantly from the vertical direction, especially for higher friction/interlocking sediments, while horizontal inflow also becomes also significant for lower friction angle sediments. Sub-surface displacements propagate from the contracted volume to the surface within a fan-shaped region.

Contact forces arch around the contracted region and the new grains that fill the cavity experience very low contact forces. This “effective void” is an inherent consequence of interparticle friction and rotational frustration; in fact, the force arch is more prominent for higher friction and/or denser sediments. The presence of grains in the effective void contributes to preventing the buckling of the surrounding force arches.

The maximum surface settlement decreases with the normalized inclusion depth z/D, density and interlocking, yet, the affected width increases with increasing z/D and decreasing grain interlocking. The surface settlement volume per unit length is smaller than the volume lost in dilative, dense, and more frictional sediments, and porosity increases above the cavity. However, the surface settlement volume may exceed the subsurface volume loss in contractive, loose, and less interlocked sediments. Horizontal flow into the cavity reduces subsurface vertical displacement especially when deeper cavities form in looser and less interlocked sediments.

# CHAPTER 6

# DISSOLUTION AND CLOSURE OF DEEP GRANULAR ZONES – EFFECTS ON ADJACENT SOILS

## 6.1 Introduction

Localized dissolution or volume collapse deep underground may result from decementation/softening driven by geochemical changes (including hydrate dissociation), or structural collapse such as old mines (Berest et al. 2008, Waltham et al. 2011). In particular, advection and high reaction rates may combine to cause localized dissolution in rocks such as in carbonates (Haq et al. 1987, Nystrom et al. 1991, Harris et al. 1997b).

Chapter 5 explored the effect of near-surface local volume contraction on overlying sediments when the dissolvable inclusion size D is shallower than $z/D<10$. This chapter investigates the consequences of localized volume contraction of deep inclusions. We note that available continuum solutions (e.g., Kirsch 1898 and Inglis 1913) apply to materials such as intact rocks (Durelli et al. 1966, Leeman 1971, Goodman 1989). However, there is limited insight into the effects of cavity contraction in uncemented granular materials.

This study explores the consequences of localized granular dissolution using the discrete element model. In these simulations, a zone made of dissolvable grains located at the center of a representative elementary volume REV is subjected to gradual granular dissolution over time. The study includes both 2D (tunnel-shaped cavity) and 3D (domes) simulations.

## 6.2 Numerical simulation

### 6.2.1. Simulation environment

The stress gradient along the inclusion height is negligible when the depth z to inclusion size D ratio is large, say z/D>10. The REV tested in these simulations is subjected to constant vertical stress and zero-lateral strain boundary conditions: strictly speaking, this implies horizontally repetitive conditions (Figure 6.1).

Table 6.1 shows the basic simulation environment and properties used in 2D and 3D simulations. Circular disks (2D) and spheres (3D) have a uniform size distribution. The linear contact model is used in 2D simulations, while the non-linear Hertzian contact model is used in 3D simulations. Granular interlocking due to particle angularity is simulated by hindering the rotation of fraction HR of randomly located particles where HR=0%, 40%, and 80%. The soluble zone has a global circular shape size D and is located at the center of a square or cubic REVs size L (Figure 6.1). Three different contractible zone sizes are tested: the case of D/L=0.2 corresponds to sparsely populated deep inclusions, while the case of D/L=0.6 corresponds to interacting near-neighbor cavities. Finally, the percentage of particles within the contractible zone that experience size reduction is either SF=50% or 100%. Table 6.2 summarizes the parametric study. Results are presented next for SF=50%; results for SF=100% are essentially similar to those presented here.

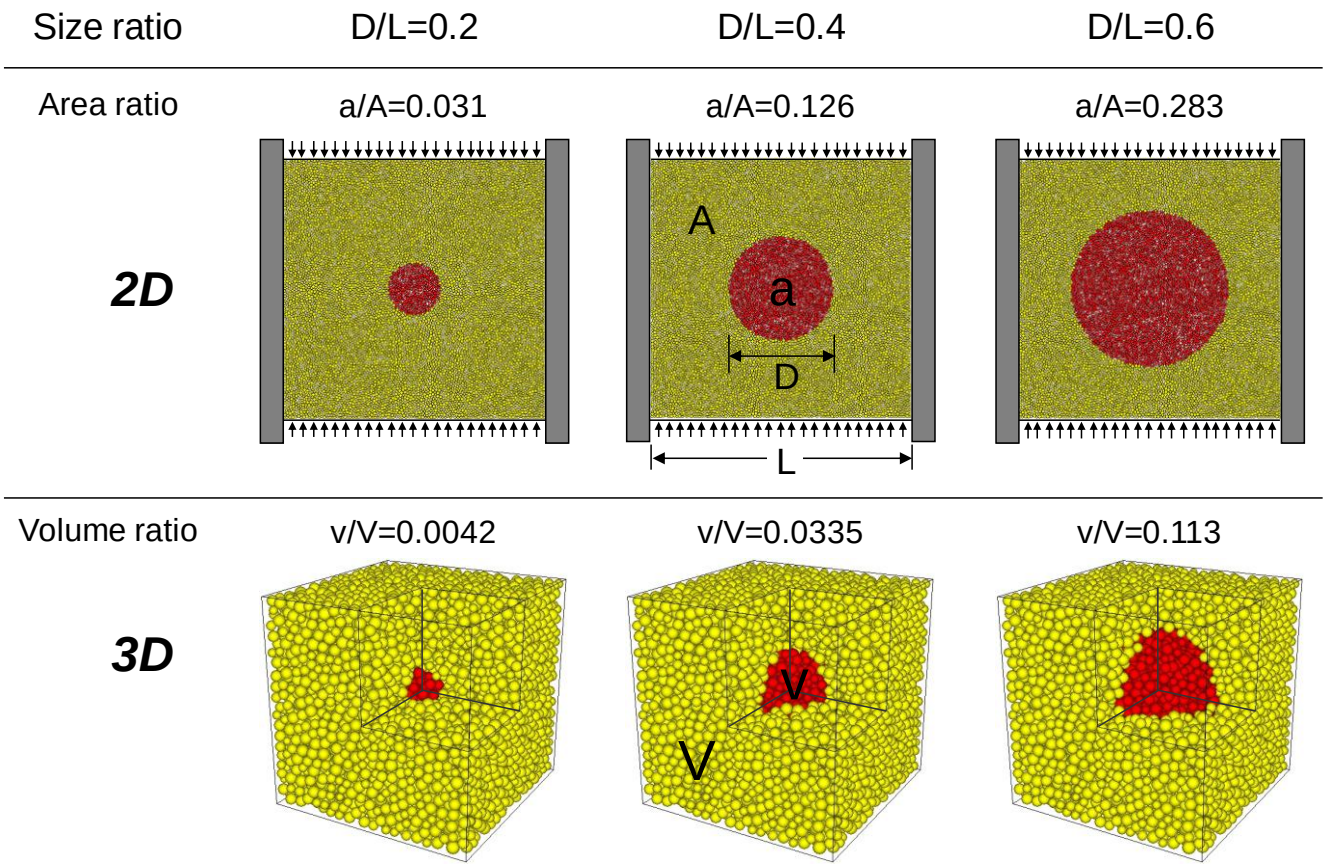


Figure 6.1 Initial size of the dissolvable zones: Red grains are soluble (All cases shown are for SF=100%).

Table 6.1 Discrete element simulation environment.

| | Properties | 2D | 3D |
|---|---|---|---|
| Particle properties | Particle size distribution | Uniform size distribution ($R_{min}$=0.4 mm, $R_{max}$=0.6 mm) | Uniform size distribution ($R_{min}$=1 mm, $R_{max}$=1.5 mm) |
| | Number of particles | 10567 disks | 9167 spheres |
| | Particle density | 2650 kg/$m^3$ | 2650 kg/$m^3$ |
| | Contact model | Linear contact model<br>-Normal stiffness kn =$10^8$ N/m<br>-Shear stiffness ks = $10^8$ N/m | Hertzian contact model<br>-Shear modulus = $2.9\times10^9$ Pa<br>-Poisson's ratio = 0.3 |
| | Inter-particle friction | 0.5 | 0.5 |
| | Hindered rotation HR | 0%, 40%, and 80% | 0%, 40%, and 80% |
| Boundary conditions | Initial cell size | (Height × Width)<br>10 cm × 10 cm | (Height × Width × Length)<br>5cm × 5cm × 5cm |
| | Vertical load | 100 kPa (during dissolution) | 100 kPa (during dissolution) |
| | Lateral boundaries | Zero strain | Zero strain |
| | Particle-to-wall friction | 0 | 0 |

Table 6.2 Parametric study.

| Dimension | Relative zone size D/L* | Soluble fraction SF** | Hindered rotation HR*** |
|---|---|---|---|
| 2D | 0.2 | 50% | 0%, 40%, and 80% |
| | | 100% | 0%, 40%, and 80% |
| | 0.4 | 50% | 0%, 40%, and 80% |
| | | 100% | 0%, 40%, and 80% |
| | 0.6 | 50% | 0%, 40%, and 80% |
| | | 100% | 0%, 40%, and 80% |
| 3D | 0.2 | 50% | 0%, 40%, and 80% |
| | | 100% | 0%, 40%, and 80% |
| | 0.4 | 50% | 0%, 40%, and 80% |
| | | 100% | 0%, 40%, and 80% |
| | 0.6 | 50% | 0%, 40%, and 80% |
| | | 100% | 0%, 40%, and 80% |

Most results shown are for SF=50% soluble fraction in the inclusions. **: Percentage of particles within the cavity that experience size reduction. ***: Percentage of particles with hindered rotation in the REV.

### 6.2.2. Procedure

Particles are generated at random locations and allowed to expand gradually within the 2D square and 3D cubic cells under zero gravity and zero interparticle friction until they reach their target size. Then, friction and gravity are turned on, and the sediment is incrementally subjected to vertical stress to reach 100 kPa under zero lateral strain boundary conditions (Note: there is no friction between grains and walls). The dissolution of particles in the contractible zone is performed simultaneously reducing the radius of all SF soluble particles. Slow size reduction is enforced to prevent numerical instability and dynamic effects. The physical simulation time is ~40 seconds for 2D and

~55 seconds for 3D cases for the physical REV length L=5cm, so that global accelerations are less than $a<10^{-5}$ g.

## 6.3 Results

Simulation results include the evolution of macro- and particle-scale parameters. These are presented as a function of the normalized size reduction NSR ($\Delta R/R_0$) of soluble particles within the contractible zone.

### 6.3.1. Normalized vertical displacement δ/L and porosity

The vertical contraction δ is normalized by the initial REV size L. The δ/L ratio increases with the contractible zone size D/L (Figure 6.2 to 6.4 for 2D and 3D simulations). The normalized vertical displacement decreases and porosity increases for higher sediment friction angles (i.e., interlocking in terms of hindered rotation HR).

### 6.3.2. Equivalent global stress ratio $k_0$

The equivalent global stress ratio is computed by adding all contact forces against lateral walls divided by the "instantaneous sediment height" L*, and dividing by the sum of vertical contact forces against the upper boundary divided by the sediment width L.

$$k_0^{eq} = \frac{\Sigma F^H}{\Sigma F^V} \cdot \frac{L}{L^*} \tag{6.1}$$

In general, the equivalent global stress ratio $k_0$ increases with dissolution to eventually reach a steady value that can be as high as k≈0.7 to 0.8 (higher for lower interlocking HR). An early drop in $k_0$ is measured for packings with high interlocking (e.g., HR=80%) and large contractible zone (e.g, D/L>0.4) (Figure 6.2~6.3). Fluctuations in the equivalent global stress ratio $k_0$ trends hint to successive internal slippages (Figure 6.2).

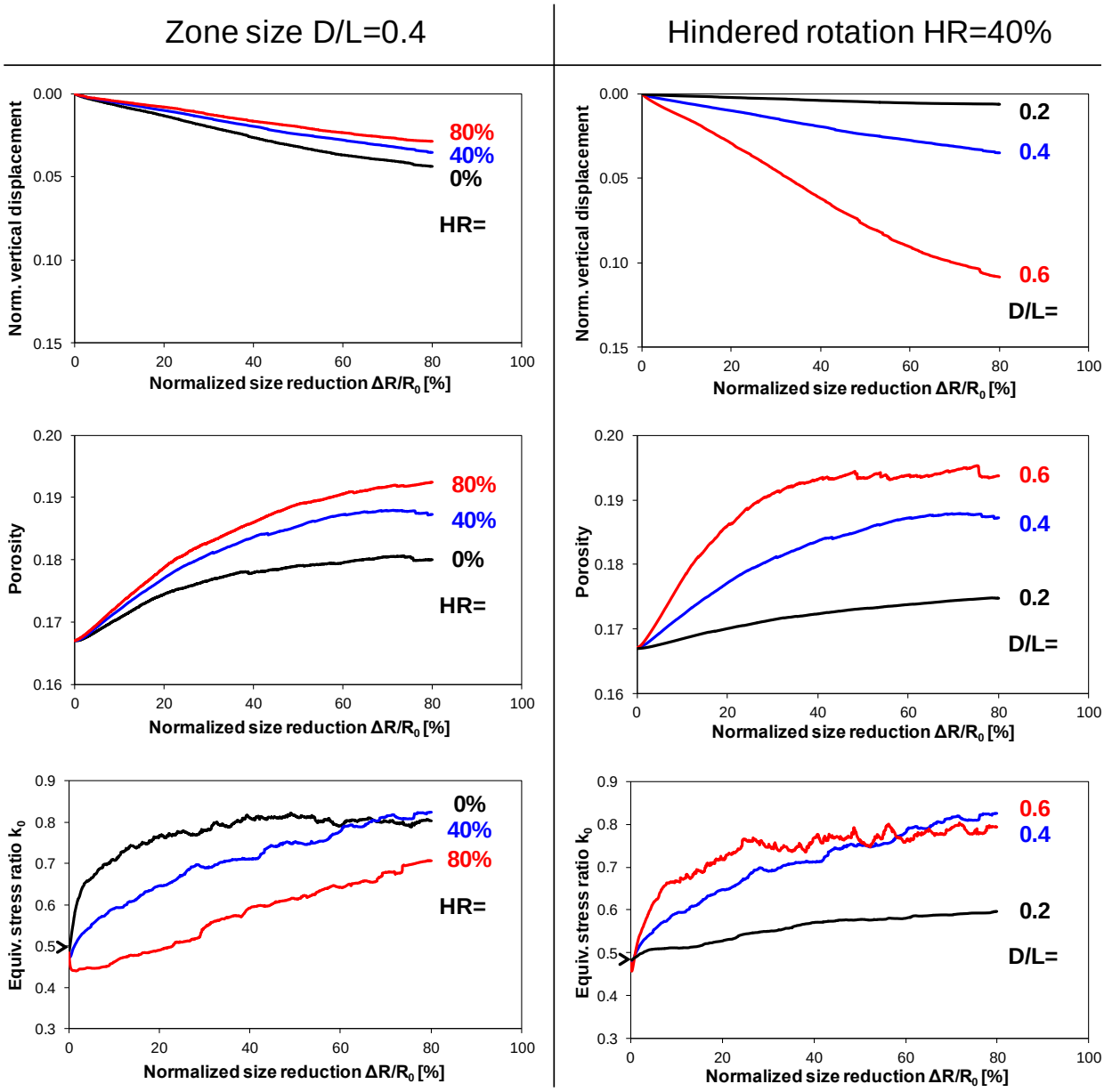


Figure 6.2 Normalized vertical displacement, porosity, and equivalent global stress ratio $k_0$ during regional dissolution. 2D simulations for a SF=50% fraction of soluble particles in the contractible zone.

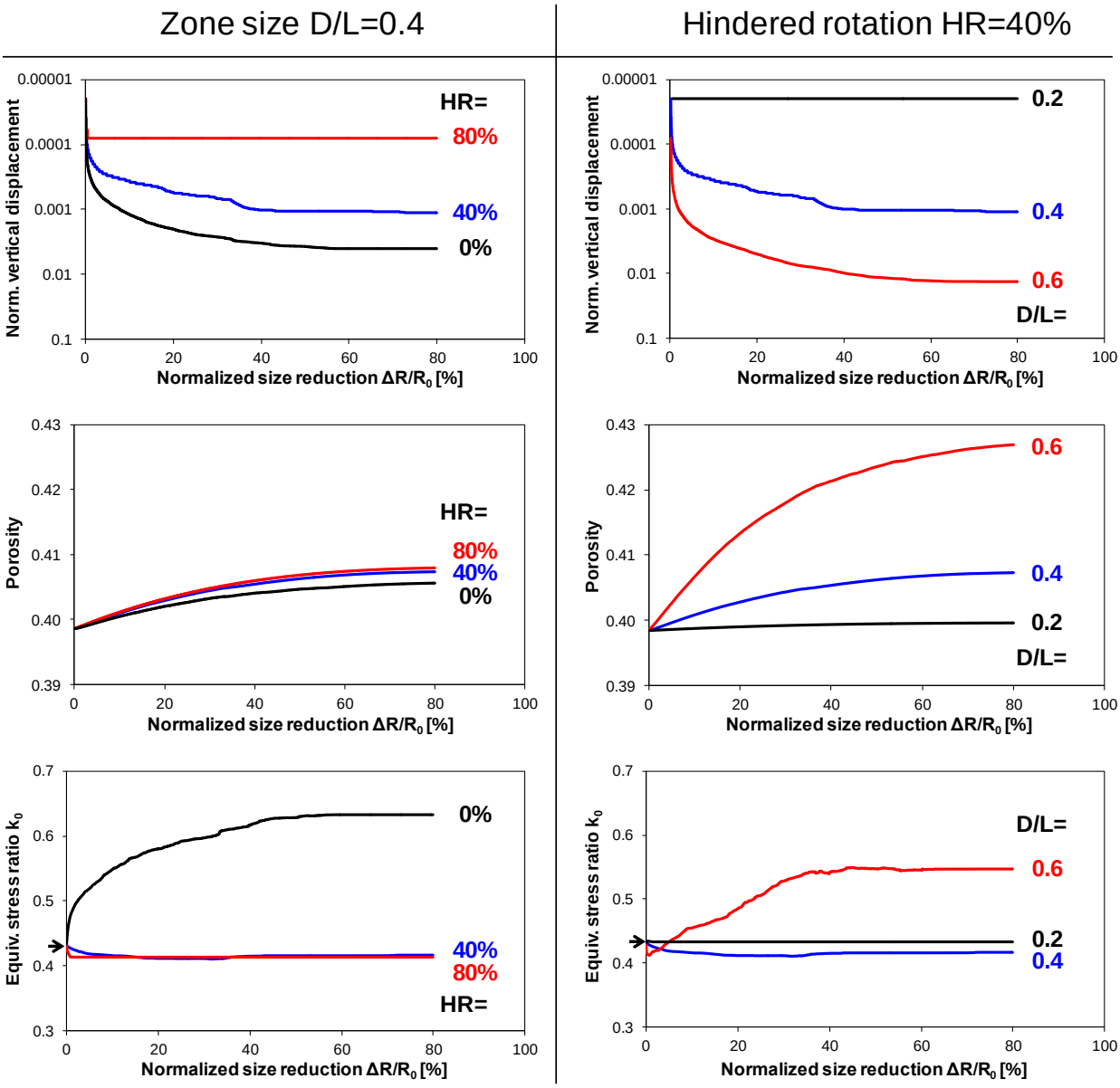


Figure 6.3 Normalized vertical displacement, porosity, and equivalent global stress ratio $k_0$ during regional dissolution. 3D simulations for a SF=50% fraction of soluble particles in the contractible zone.

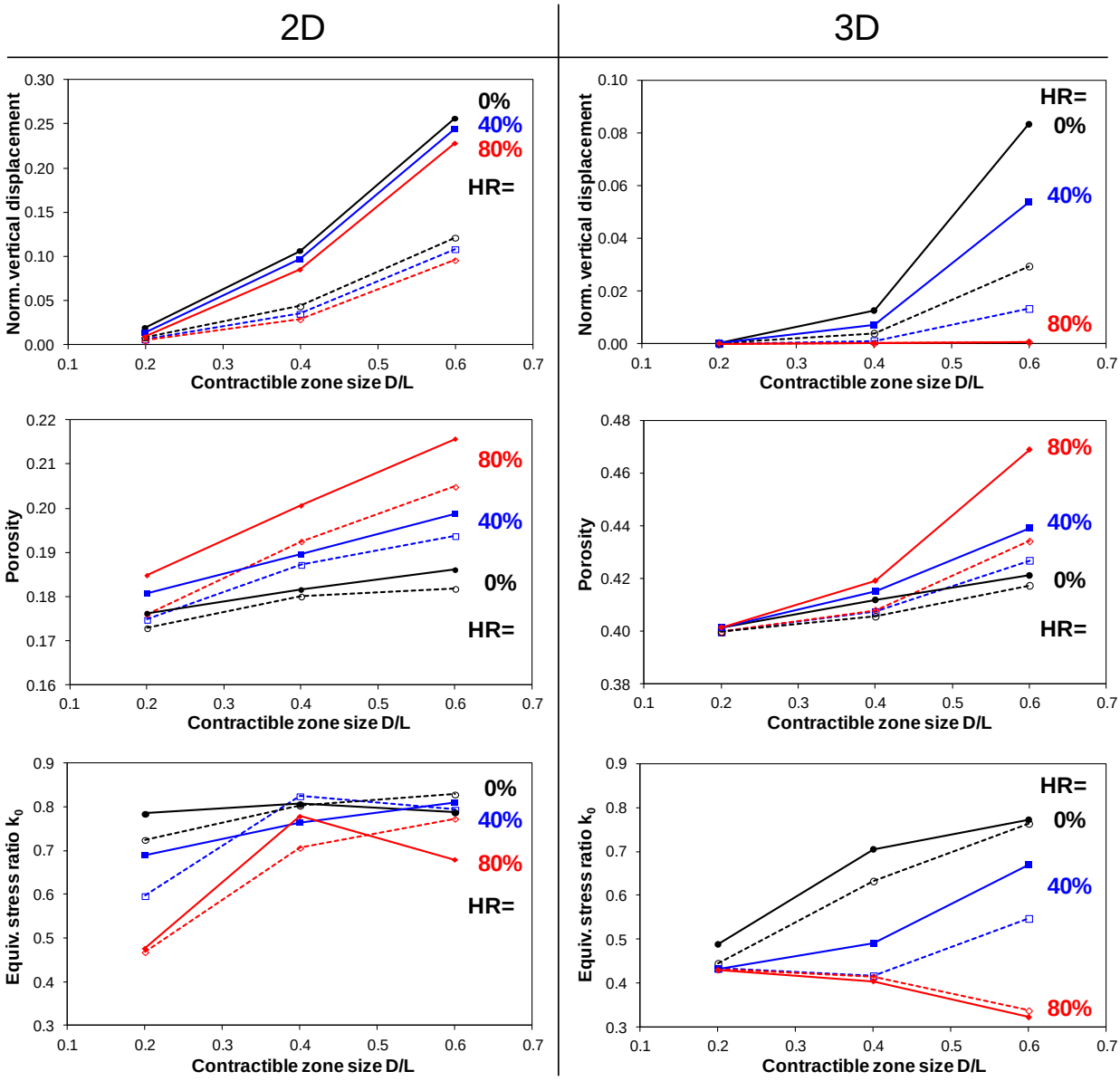


Figure 6.4 Normalized vertical displacement δ/L, porosity, and equivalent global stress ratio $k_0$ according to zone size D/L and HR after $\Delta R/R_0$=80% size reduction. 2D and 3D simulations. Note: Dotted lines for soluble fraction SF=50% inside the dissolvable zone and solid lines for SF=100%.

### 6.3.3. Displacement vectors

Grains adjacent to the contractible zone flow towards the shrinking volume as particles dissolve (Figure 6.5a) and no cavity remains after dissolution in agreement with the cohesionless nature of the sediment.

Horizontal displacements prevail along the side of the contractible zone and is mostly responsible for filling the contractible space (Figure 6.5); vertical displacement is more dominant above and below the zone (Figure 6.5).

### 6.3.4. Contact force arching and "effective void"

An effective void in terms of interparticle contact forces remains after dissolution (Figure 6.5). Forces arch around the contractible zone as a consequence of interparticle friction and rotational frustration, and there are only small transverse forces inside the contracted zone that prevent chain buckling. Force arching is more pronounced and a larger "effective void" forms in sediments with higher friction angle.

The "effective void" forms immediately after dissolvable particles start contracting, especially in highly interlocked sediments. Clearly, even minute radius reductions mobilize internal friction/interlocking of surrounding grains and unloads initial force chains across the contractible zone. As dissolution progresses, the "effective void" size increases toward the boundaries. Eventually, the area strongly influenced by regional dissolution is significantly larger than the initial size of the contractible zone (Figure 6.5). This will affect site characterization interpretation, such as penetration resistance data.

Stresses become most concentrated at the sides of the inclusion during and after dissolution, similar to the case of shallow inclusion (Chapter 5) and in agreement with continuum mechanics, as vertical stress is transferred to the sides. The stress concentration is more pronounced for sediments with higher friction angle. This is

because the vertical stress in the inclusion is transferred to the sides, which leads to a high concentration of contact forces at the sides.

### 6.3.5. Comparison of simulation results: 3D versus 2D

No precise comparisons between 2D and 3D simulations are possible because of geometric differences (2D tunnel shape vs. 3D dome) and inherent differences between 3D spheres and 2D disks (i.e., 3D rods). Yet, most trends are similar in 2D and 3D, in terms of all parameters analyzed in this study, including D/L, HR and $\Delta R/R_0$. This highlights the commonality among governing processes. The effect of varying grain interlocking is more prominent in 3D due to higher coordination and macro-scale parameters such as vertical displacement change dramatically as the contractible zone size increases.

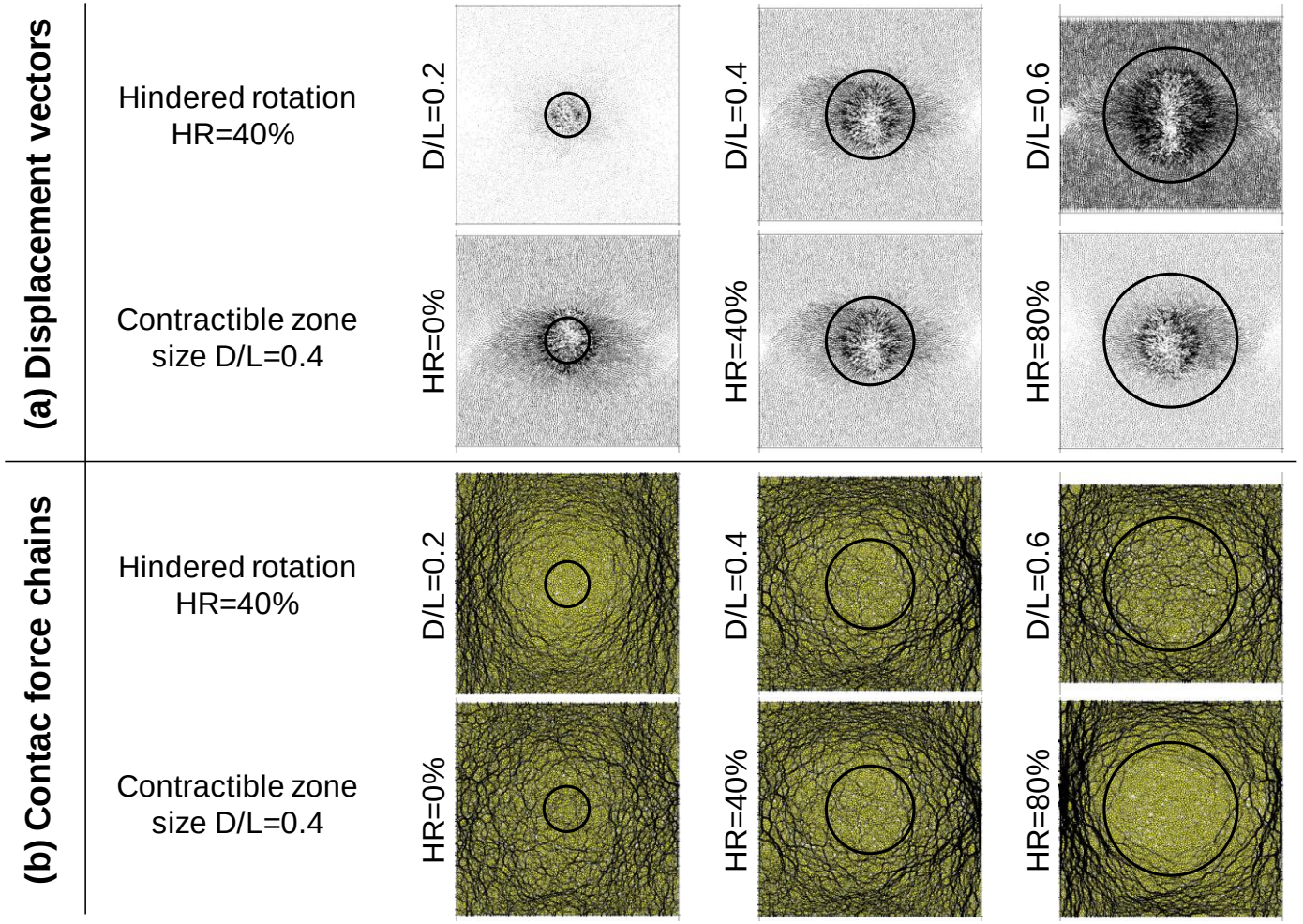


Figure 6.5 Contact force chains and displacement vectors after dissolution. 2D simulations for a SF=50% fraction of soluble particles in the cavity. Note: black circles show the original size of the contractible zone.

## 6.4 Conclusions

The dissolution of deep and concentrated regions affects the surrounding soil properties. Vertical contraction and changes in global porosity increase with the size of the contractible zone D/L. On the other hand, while normalized vertical displacement decreases for higher sediment friction angles (i.e., interlocking in terms of hindered rotation HR), the porosity increases.

The equivalent global stress ratio $k_0$ increases with dissolution to eventually reach a steady value that can be as high as k≈0.7 to 0.8 (lower stress anisotropy for lower interlocking HR). An early drop in $k_0$ is measured for packings with high interlocking (e.g., HR=80%) and large contractible zone (e.g, D/L>0.4). Fluctuations in the equivalent global stress ratio $k_0$ trends hint to successive internal slippages.

Grains adjacent to the contractible zone flow towards the shrinking volume as particles dissolve and no cavity remains after dissolution in agreement with the cohesionless nature of the sediment. Horizontal displacements prevail along the side of the contractible zone and are mostly responsible for filling the contractible space; vertical displacements are more dominant above and below the zone.

Boundary forces arch around the dissolved region as a consequence of interparticle friction, rotational frustration, and virtual forces that prevent chain buckling. Although there are no apparent cavities, the soils that flow into the inclusion carry little load, yet they play a critical role in preventing arch buckling. The area influenced by regional dissolution is significantly larger than the initial inclusion size. This will affect site characterization interpretation, such as penetration resistance data.

# CHAPTER 7

# PRE-DISSOLUTION AND POST-DISSOLUTION PENETRATION RESISTANCE

## 7.1 Introduction

Sediments undergo either dissolution or precipitation in response to changes in hydro-chemical conditions. Particle-scale dissolution is an ubiquitous diagenetic process that contributes to changes in soil structure and properties. Mineral dissolution is triggered by changes in pH and/or pore water chemistry, and continues while the pore water remains chemically under-saturated. Rain and ground water flow are the natural drivers for these changes. Water pumping, imposed thermal changes and various pollutant can increase dissolution kinetics. Karst terrains and ground collapses are remarkable natural examples of mineral dissolution (Waltham et al. 2005, Hunt 2007). Short-term geothermal projects, hydrate dissociation, and long-term dissolution in $CO_2$ storage reservoirs are relevant examples in the energy sector (Le Guen et al. 2007, Espinoza et al. 2011).

The consequences of dissolution on sediment behavior and the characterization of sediments in view of diagenetic dissolution remain largely uninvestigated. In this chapter, we explore the effects of initial density and the lost mass fraction on dissolution-driven changes in density and penetration resistance for normally-loaded uncemented sands. A review of available information about the consequences of mineral dissolution is presented first.

### 7.2 Previous studies on mineral dissolution

Selective or differential mineral dissolution reflects differences in mineral solubilities and reaction kinetics (Stumm and Morgan 1996). Minerals that form at higher temperatures and pressures are less stable under shallow, near surface conditions (Goldich 1938). Dissolution is often accompanied by precipitation; in particular, the weathering of many rocks yield clay minerals (Eggleton et al. 1987, Schlesinger 1991, Polyak and Güven 2000); for example, kaolinite precipitates when feldspar is weathered and metal ions are leached away (Zhu and Lu 2009). The dissolution of grains in sediments affects the sediment physical properties. Results from previous studies and related observations in this thesis are summarized next.

*Void ratio, coordination number, and compressibility*. Normalized vertical displacement and void ratio increase during grain dissolution (Fam et al. 2002, Truong et al. 2010). The normalized vertical displacement and changes in void ratio are proportional to the initial mass fraction of dissolvable grains (Shin and Santamarina 2009, Truong et al. 2010). The coordination number decreases after dissolution and compressibility increases during post-dissolution zero lateral strain loading (Chapter 2, 4, 5, and 6).

*G or Vs*. Shear wave velocity decreases (Fam et al. 2002, Truong et al. 2010) and material attenuation increase after dissolution (Fam et al. 2002). The changes in shear wave velocity are proportional to the initial mass fraction of dissolvable grains (Truong et al. 2010). Similarly, the elastic modulus (E, M, K, or G) decreases in hydrate bearing sediments after hydrate dissociation (numerically: Holtzman et al. 2008 and Jung et al. 2012; experimentally: Espinoza and Santamarina 2011). The dissolution or softening of cementing bonds in soils can increase compressibility or lead to the sediments collapse (Abduljauwad and Al-Amoudi 1995, Ismael and Mollah 1998, Rinaldi et al. 1998, Mansour et al. 2008, Mansour et al. 2009).

*Friction angle*. The peak friction angle decreases after dissolution and initially dilative soils may become contractive as the extent of dissolution increases (Fam et al. 2002; Chapter 2).

*Fabric - Microstructure changes*. Distinct force chains and a "honeycomb fabric" characterize sediments after selective mineral dissolution increases (Chapter 2 and 3 - Shin et al. 2008, Shin and Santamarina 2009). Load carrying grain arches develop around the dissolving particles and the local porosity increases (also Chapters 4, 5 and 6).

*Equivalent global stress ratio $k_0$.* The evolution of the equivalent global stress ratio $k_0$ between the horizontal and vertical effective stresses during dissolution under zero lateral strain conditions has been investigated experimentally, analytically, and numerically. Results show that mineral dissolution causes a decrease in the coefficient of lateral stress from $k_0$ to the active condition $k_a$ and internal shear planes may develop (Chapter 2 and 3). Contraction-driven shear failures may even cause polygonal faults (Shin and Santamarina 2009). The load-cementation-dissolution history is important; the dissolution of the cementing agent in normally loaded cemented sand subjected to constant vertical load increases the $k_0$ to a value similar to that of uncemented soils (Castellanza and Nova 2004).

*Shear resistance.* The response of sediments that experienced dissolution during simple shear was studied numerically in Chapter 2. Results show that the peak shear resistance decreases after dissolution, and sediments become more contractive (Fam et al. 2002 - Chapter 2). The higher contractive tendency increases the vulnerability to seismic-induced settlement and liquefaction. At large strains, all specimens converge to the

critical state line. Effective shear strength parameters c' and Φ' decrease due to leaching of the cementing agent in sands (Ismael and Mollah 1998).

**Penetration resistance – Previous studies**

The most common site characterization tools in geotechnical engineering are based on penetration resistance. Penetration resistance in sands is controlled by relative density, effective stress state, friction angle, and to a lesser degree by soil compressibility, age, and cementation.

*Relative density*. Cone resistance is strongly affected by relative density in sandy soils (Mayne and Kulhawy 1991, Salgado et al. 1997). Consequently, cone penetration is extensively used to assess liquefaction potential (Robertson and Wride 1998, Chang et al. 2006, Mayne et al. 2010).

*Friction angle*. Cone tip resistance is dependent on friction angle as predicted by bearing-capacity equations (Terzaghi 1943, Meyerhof 1963, Hansen 1970). Semi-empirical relationships have been proposed to correlate friction angle and cone tip resistance (Kulhawy and Mayne 1990, Chen and Juang 1996).

*State of stress*. Cone tip resistance is more sensitive to the lateral stress than the vertical effective stress (Houlsby and Hitchman 1988, Salgado et al. 1997, Ahmadi et al. 2005). The proportionality between $q_c$ and $\sigma_h$' depends on the soil friction angle (Houlsby and Hitchman 1988).

*Soil compressibility*. Sands with high compressibility produce lower cone resistance for the same relative density compared to sands with low compressibility. The compressibility of sands is controlled by grain characteristics, such as grain mineralogy

and angularity, e.g., carbonate sands are more compressible than silica sands, and angular silica sands are more compressible than rounded silica sands (Ghafghazi and Shuttle 2008, Robertson 2009).

*Cementation.* Cementation significantly affects the cone tip resistance in cemented soils (Rad and Tumay 1986), where the effects of stress and density are diminished (Lee et al. 2010). Conversely, the effect of increasing confinement gradually overshadows the influence of weak cementation (Puppala et al. 1995).

*Aging*. The cone resistance in sand increases with time after deposition or densification (Mitchell 1986, Mesri et al. 1990, Schmertmann 1991, Baxter and Mitchell 2004, Leon et al. 2006).

*Other parameters*. Other parameters affect the cone resistance including stress history, mineralogy, grain crushing, grain size distribution and angularity. The effect of these parameters is either small or it is already taken into consideration through some of the variables listed above.

### 7.3 Devices and procedure

Calibration chamber tests are typically used to establish relationships between cone resistance and soil properties. The cone resistance measured in a calibration chamber differs from that measured in the field because of boundary effects: In all cases, the difference between chamber and field cone resistance values decreases as the ratio of chamber to cone diameter increases (Mayne and Kulhawy 1991, Salgado et al. 1998). A constant lateral stress condition underestimates field $q_c$-values, while a zero lateral strain condition overestimates field $q_c$-values (Parkin and Lunne 1982, Iwasaki et al. 1988).

Boundary effects increase with soil dilatancy, i.e., dense packing and low effective stress (Been et al. 1988, Mayne and Kulhawy 1991, Schnaid and Houlsby 1991, Salgado et al. 1998, Ahmadi and Robertson 2008).

The zero-lateral strain calibration chamber used for this study is spring-loaded to impose a constant vertical stiffness condition that resembles field situations (ID=191mm, see Figure 7.1a). The spring length (152mm) and stiffness (58N/mm) are selected to accommodate significant deformations with minor changes in vertical stress for an operating vertical effective stress of 100 kPa. The bottom plate is densely grooved to ensure one-dimensional fluid flow.

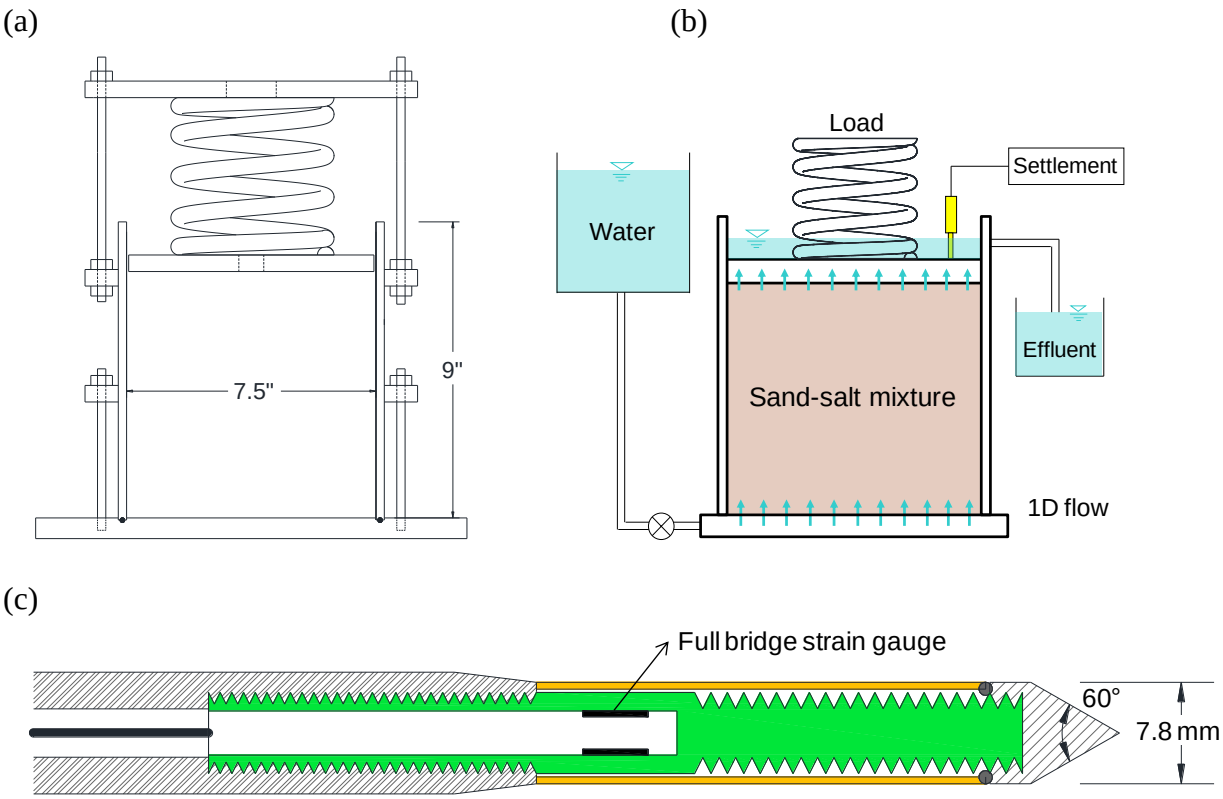


Figure 7.1 Devices. (a) Spring-loaded calibration chamber (b) Mineral dissolution under constant vertical effective stress at zero-lateral conditions (c) Cone instrumented with full-bridge strain gauge to measure tip resistance.

The small-diameter cone (OD=7.8mm) satisfies a 24-to-1 chamber-to-cone diameter ratio to minimize boundary effects (Figure 7.1c). The cone tip (apex angle 60°) is mounted onto a force-sensing stud to effectively determine the tip resistance (force transducer range: 0 to 1200 N). The cone side resistance is mechanically removed by using an outer sleeve so that the tip resistance can be measured reliably (Figure 7.1c).

*Sediment preparation.* The sediment is formed by mixing Ottawa F-110 sand (insoluble grains) and table salt (dissolvable grains); properties are listed in Table 7.1. Mixtures are packed at various densities: first, the mixture is placed inside the chamber by funneling, followed by successive impacts on the chamber walls to achieve the target densities. Mixture dry densities and initial void ratios are listed in Table 7.2. The specific gravities of insoluble ($G_U$=2.65) and dissolvable grains ($G_D$=2.165) are different; their weighted average is used to calculate global void ratios:

$$e = \frac{\gamma_W}{\gamma_{dry}} \frac{G_U G_D}{(1-m)G_D + mG_U} - 1 \tag{7.1}$$

Table 7.1 Materials.

| | Insoluble grains | Dissolvable grains |
|---|---|---|
| Materials | Ottawa F-110 sand | Table salt |
| $D_{50}$ | 0.12 | 0.3 |
| $G_S$ | 2.65 | 2.165 |
| $e_{min}$ | 0.535 | 0.45 |
| $e_{max}$ | 0.848 | 0.78 |
| Roundness | 0.7 | Cubical |
| Sphericity | 0.7 | |

Table 7.2 Specimens – Parametric study.

| | | Before dissolution | | After dissolution | |
|---|---|---|---|---|---|
| | | Dry density $\rho_d$ [g/cm$^3$] | Void ratio | Dry density $\rho_d$ [g/cm$^3$] | Void ratio |
| No salt | Loosest | 1.46 | 0.81 | Same | Same |
| | Interm. 1 | 1.47 | 0.80 | Same | Same |
| | Interm. 2 | 1.55 | 0.71 | Same | Same |
| | Interm. 3 | 1.60 | 0.66 | Same | Same |
| | Interm. 4 | 1.63 | 0.62 | Same | Same |
| | Interm. 5 | 1.65 | 0.60 | Same | Same |
| | Densest | 1.66 | 0.59 | Same | Same |
| 5% salt | Loosest | 1.48 | 0.77 | 1.48 | 0.79 |
| | Interm. 1 | 1.54 | 0.70 | 1.50 | 0.76 |
| | Interm. 2 | 1.63 | 0.61 | 1.56 | 0.70 |
| | Densest | 1.69 | 0.55 | 1.61 | 0.65 |
| 10% salt | Loosest | 1.49 | 0.74 | 1.48 | 0.79 |
| | Interm. 1 | 1.57 | 0.65 | 1.50 | 0.76 |
| | Interm. 2 | 1.65 | 0.57 | 1.53 | 0.73 |
| | Densest | 1.70 | 0.53 | 1.55 | 0.70 |
| 20% salt | Loosest | 1.52 | 0.67 | 1.46 | 0.81 |
| | Interm. 1 | 1.59 | 0.59 | 1.48 | 0.79 |
| | Interm. 2 | 1.66 | 0.53 | 1.49 | 0.78 |
| | Densest | 1.70 | 0.49 | 1.48 | 0.79 |

*Dissolution procedure.* The sediment is loaded to 100 kPa. Then while keeping the vertical stress constant (i.e., continuous adjustment to maintain the spring length constant), the sediment is subject to dissolution by slowly flowing 12 to 15 pore volumes of tap water at a constant hydraulic gradient (Figure 7.1b). The 100% sand specimen sediments without initial salt (Table 7.2) are also flushed with water before penetration.

*Penetration.* The instrumented cone is driven into the sediment at a constant speed of 12.5 mm/min using a multi-purpose loading frame (Humboldt Mfg. Co.). This low penetration velocity is selected to attain drained conditions. The vertical stress is kept constant during penetration.

## 7.4 Results

*Settlement during dissolution*. The sediment settles as it dissolves at constant vertical stress (Figure 7.2). Clearly, sediments that experience more extensive dissolution settle more (SF=20% compared to SF=5%). Furthermore, specimens with lower initial density experience larger settlement for the same fraction of soluble particles (Figure 7.2). This hints to internal changes in void ratio.

*Void ratio*. Changes in void ratio and dry density after dissolution are summarized in Table 7.2 and plotted in Figure 7.3. The void ratio increases and the dry density decreases after dissolution. Denser sediments experience a more pronounced change in density, and the increase in void ratio is higher in mixtures with increased soluble grains. However, post-dissolution void ratios do not exceed the maximum void ratio $e_{max}$ for this sand (Note: the sand-salt mixture is a binary mixture with two different particle sizes -Table 7.1, and thus can have a smaller $e_{min}$ than that of the sand-only sediment as seen in Figure 7.3a~b). At a very high salt fraction (e.g. SF=20%), the sand void ratios after dissolution are independent of the initial density or void ratio (Figure 7.3c). This is the “terminal

density" for dissolution under zero lateral strain (Narsilio and Santamarina 2008): the post-dissolution void ratio cannot be higher than this terminal void ratio regardless of the initial soluble fraction.

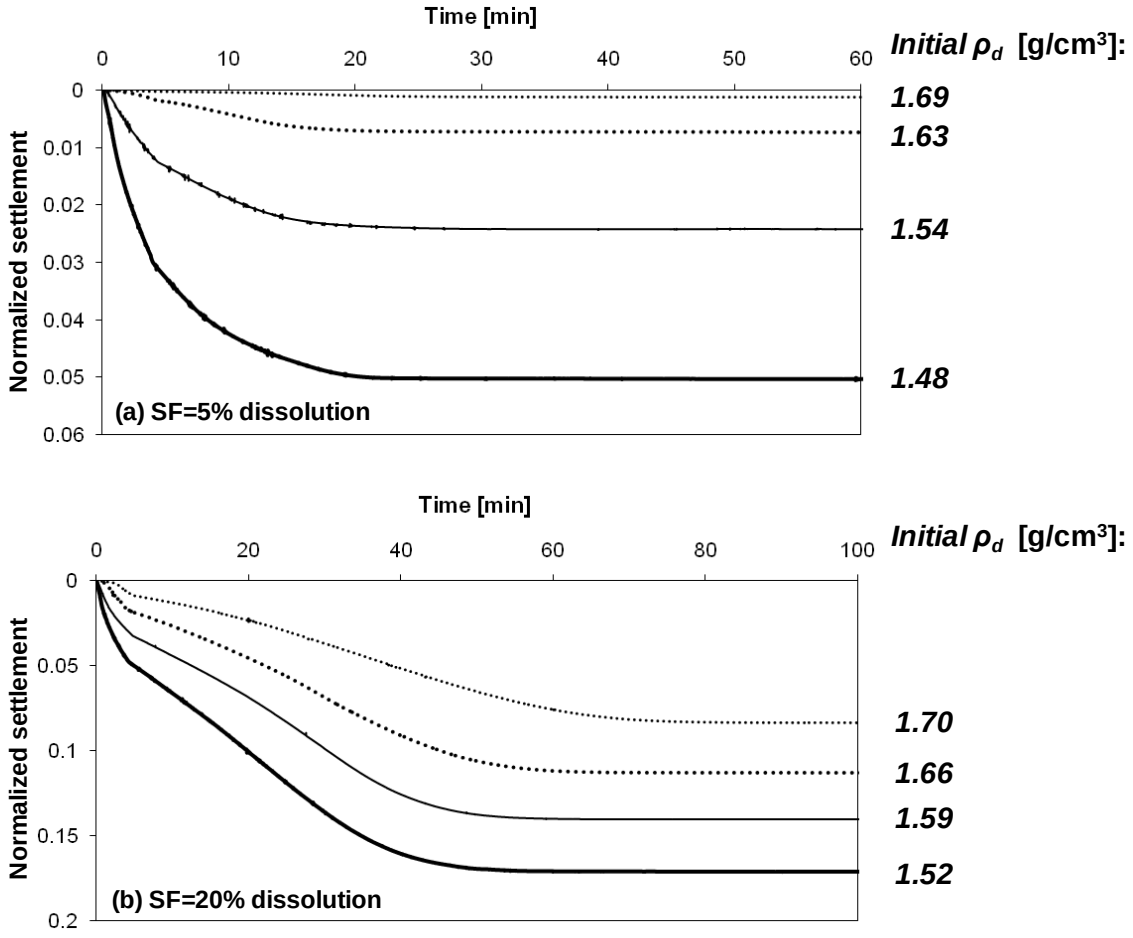


Figure 7.2 Normalized settlement during dissolution. (a) Fraction of soluble particles SF=5%. (b) Fraction of soluble particles SF=20%.

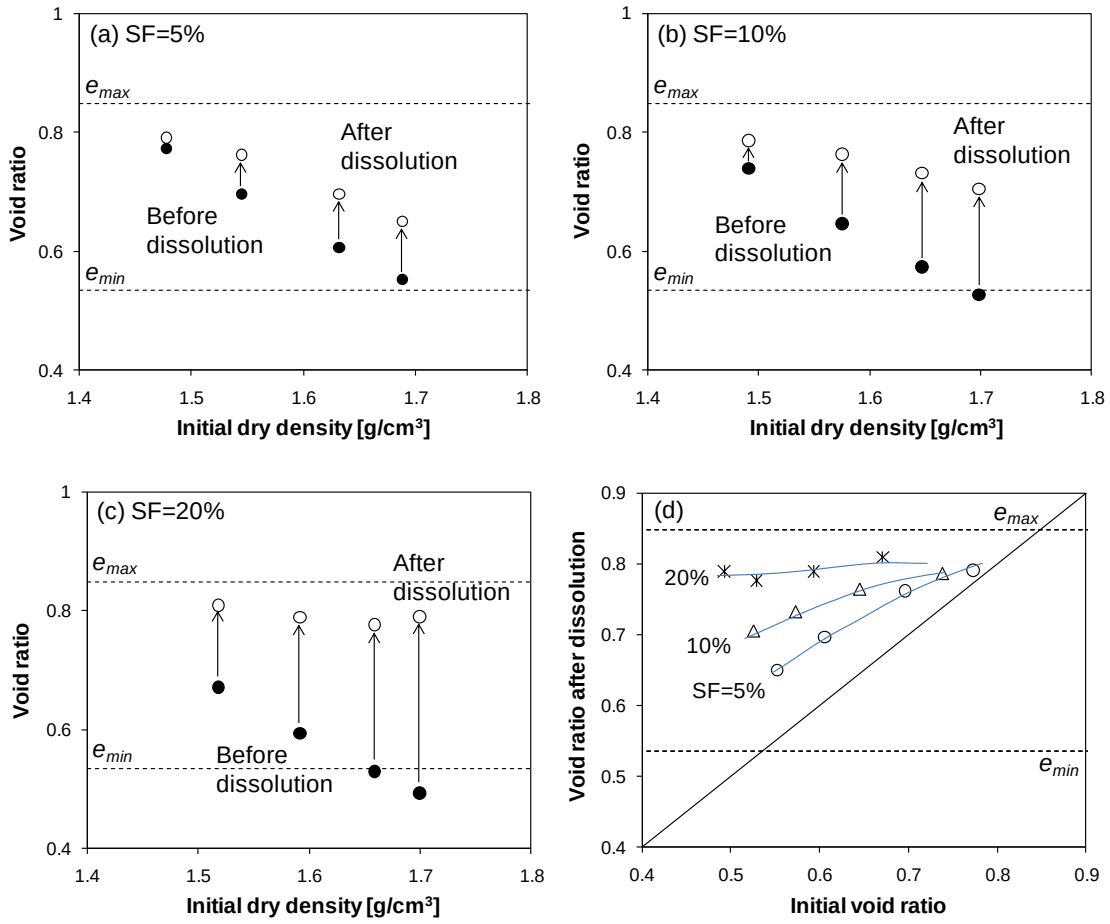


Figure 7.3 Void ratio changes upon dissolution as a function of the initial dry density and initial salt content. Initial salt contents: (a) SF=5%, (b) SF=10%, and (c) SF=20%. (d) Initial void ratio vs. void ratio after dissolution for all cases.

*Tip resistance*. Figure 7.4 shows the cone tip resistance profiles for all 18 specimens. The initial high gradient at shallow depth (z<30mm) results from upper boundary effects around the central orifice. In general, the tip resistance decreases after dissolution (Figure 7.4 - various panes). The tip resistance increases with sediment density (Figure 7.4 – each pane). The drop in tip resistance increases with the extent of dissolution, and it is most pronounced when comparing the penetration resistance in initially dense soils to the penetration resistance in the same soil after dissolution (Figure 7.4 – panes b-c-d compared to a). No appreciable changes in tip resistance are observed after dissolution in initially loose sediments.

The mean values of penetration resistance in the steady lower 2/3 of the profile are plotted together in Figure 7.5a. A single trend is observed when the tip resistance is plotted vs. void ratio at the time of penetration (Figure 7.5b). This suggests that penetration resistance is primarily a measure of density at the time of penetration.

Equations proposed in the literature for penetration resistance as a function of void ratio are superimposed on Figure 7.5b:

$$D_R = 100 \cdot \left[ 0.268 \cdot \ln\left( \frac{q_t / \sigma_{atm}}{\sqrt{\sigma_{vo}' / \sigma_{atm}}} \right) - 0.675 \right] \qquad \text{Jamiolkowski et al. 2001} \qquad (7.2)$$

$$D_R = 100 \cdot \sqrt{\frac{q_t / \sigma_{atm}}{300 \cdot OCR^{0.2} \sqrt{\sigma_{vo}' / \sigma_{atm}}}} \qquad \text{Kulhawy and Mayne 1990} \qquad (7.3)$$

$$D_R = -98 + 66 \cdot \log_{10} \frac{q_c}{\left[\sigma'_{vo}\right]^{0.5}} \quad (q_c \text{ and } \sigma'_{vo} \text{ in t/m}^2) \qquad \text{Jamiolkowski et al. 1985} \qquad (7.4)$$

These trends agree with post-dissolution experimental results obtained in this study and confirm the prevalent effect of void ratio on penetration resistance.

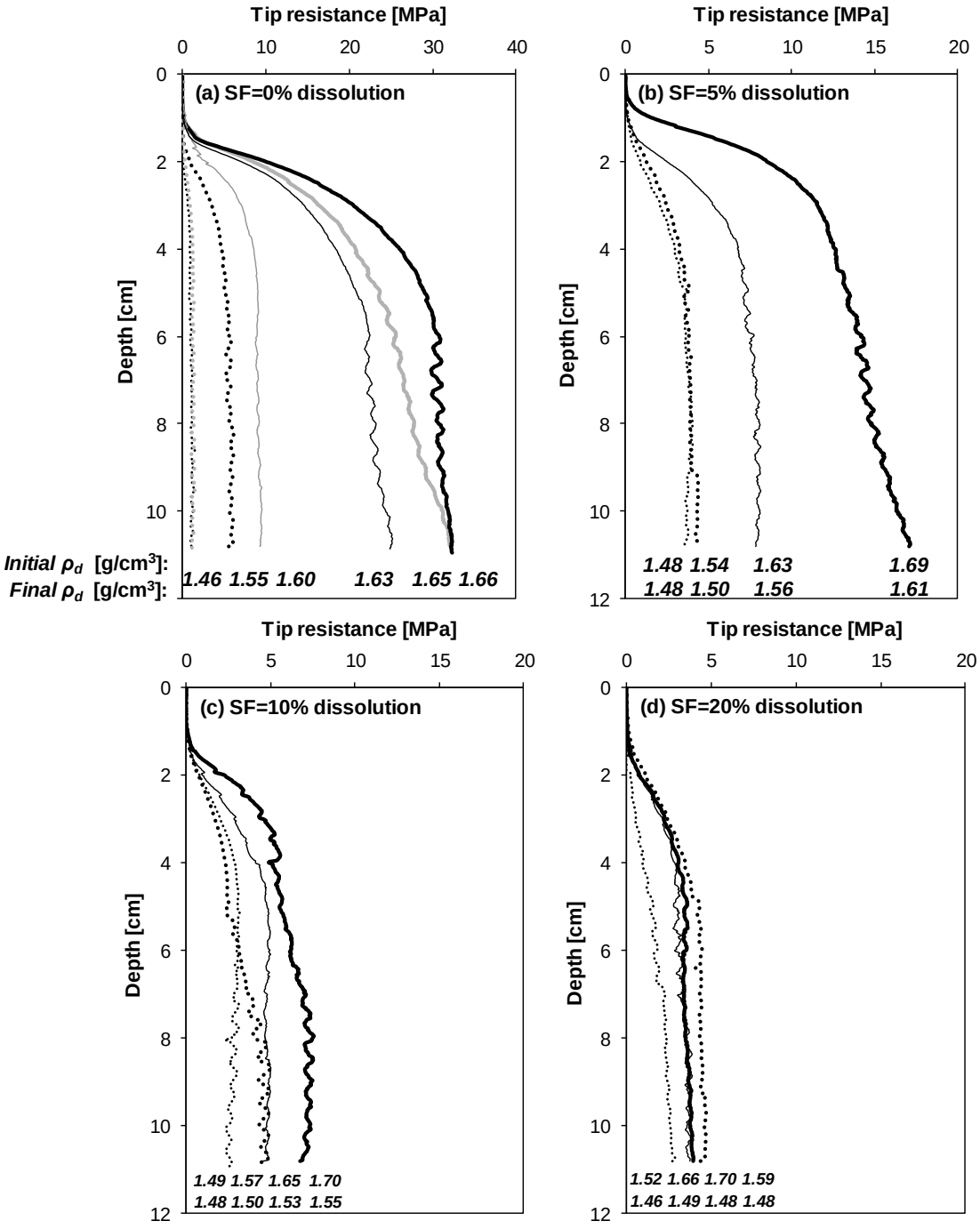


Figure 7.4 Characteristic penetration profiles. Tip resistance vs. depth for different degrees of dissolution and different densities. Initial salt contents: (a) SF=0%, (b) SF=5%, (d) SF=10%, and (d) SF=20%.

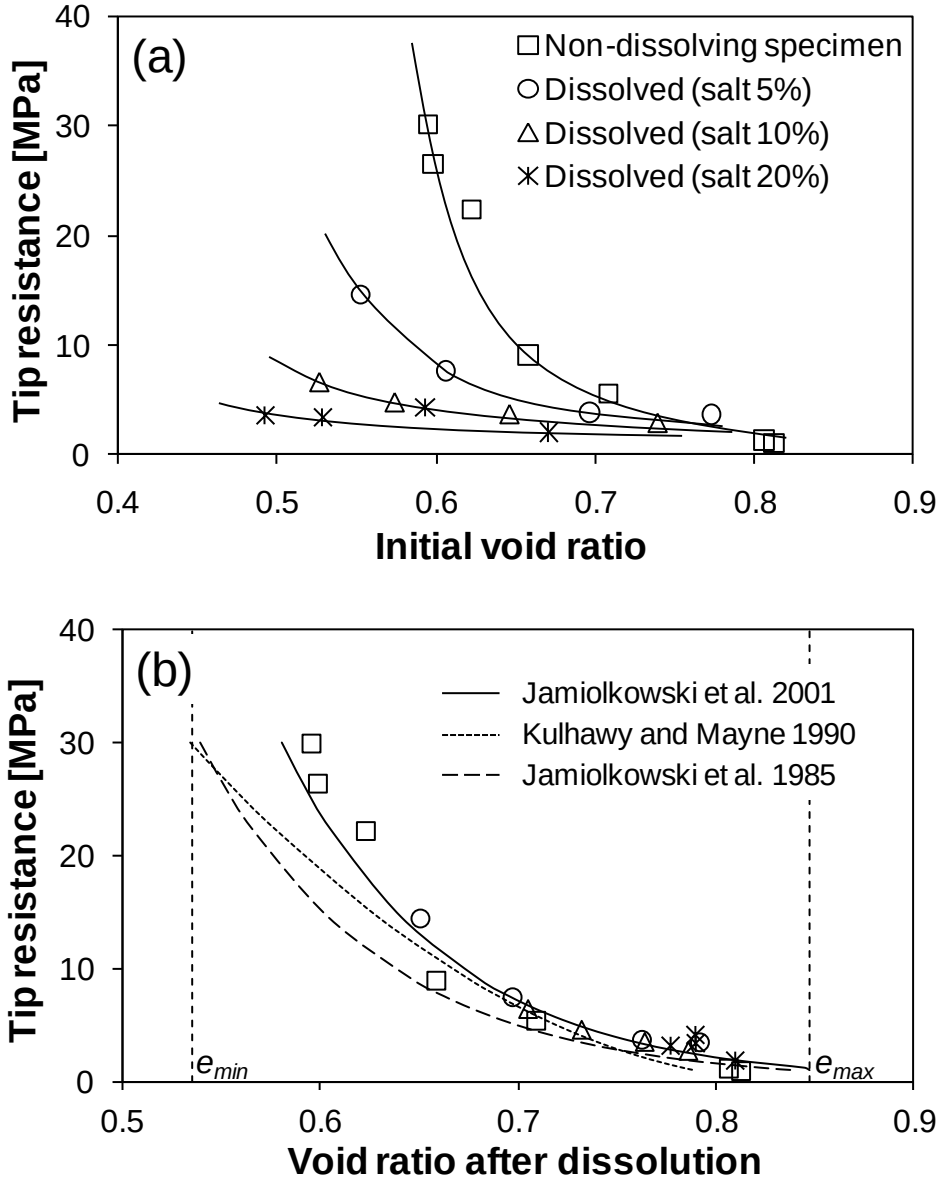


Figure 7.5 Void ratio vs. tip resistance (lower 2/3 depth profile). Resistance plotted versus (a) initial void ratio (b) void ratio after dissolution i.e., at the time of insertion.

## 7.5 Analyses and discussion

*Tip resistance vs. final void ratio.* The single trend between cone resistance and void ratio at the time of penetration indicate that cone resistance is insensitive to other dissolution effects such as changes in soil fabric and in horizontal stress, reported in previous Chapters. In part, this confirms that initial fabric does not significantly affect large-strain shear strength (Chapter 2). While the horizontal stress changes during dissolution (Shin et al. 2008, Shin and Santamarina 2009, Chapter 2), high post-dissolution void ratios minimize the effect of horizontal stress on post-dissolution cone resistance.

*Terminal void ratio*. Every process has its own terminal density or void ratio (Narsilio and Santamarina 2008). These results show that dissolution does too. Void ratios at the end of dissolution are plotted versus the normalized settlement experienced during dissolution in Figure 7.6. Extreme void ratios $e_{max}$ and $e_{min}$ are shown for reference. These results suggest that the terminal void ratio is $e_{term} \approx 0.80 \pm 0.1$ ($Dr \approx 15\%$) for dissolution under the test conditions imposed in this study. Furthermore, the data suggest that a soluble fraction SF>10% is needed to achieve the terminal void ratio; the initial density does not affect the final void ratio in sediments with soluble fractions above this threshold. Apparently, extensive dissolution disrupts force chains and granular arches everywhere. It follows that sediments with a soluble fraction higher than the threshold fraction eventually settle at constant void ratio and proportional to the extent of dissolution. Conversely, when soluble fractions are smaller than the threshold fraction, settlements are small as most of the mass loss causes a gain in porosity.

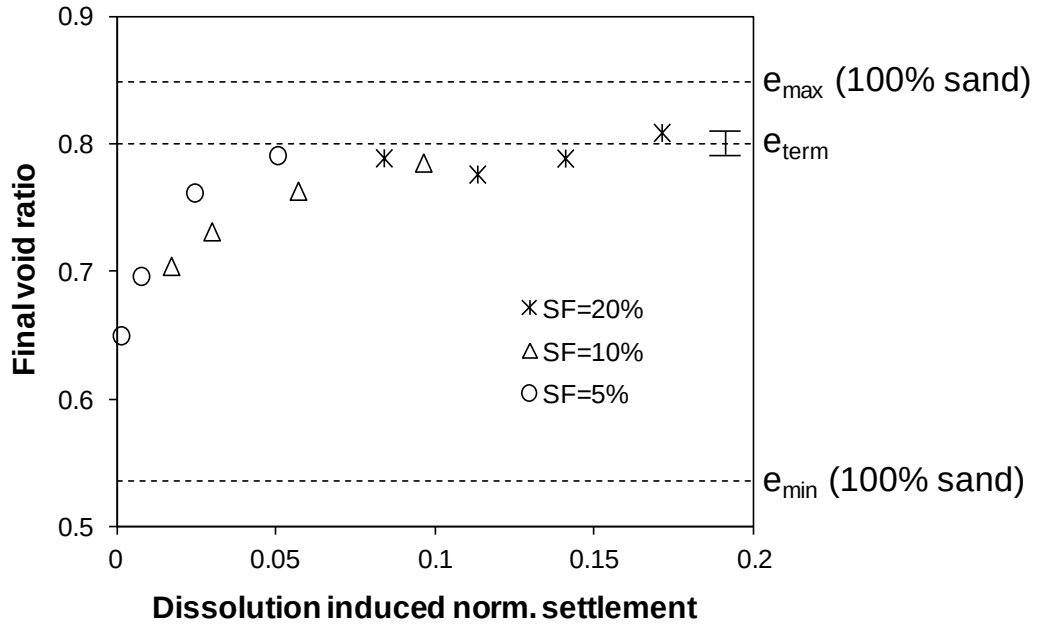


Figure 7.6 Final void ratio vs. normalized settlement: Terminal void ratio.

## 7.6 Conclusions

Mineral dissolution is an ubiquitous diagenetic process. The analysis of pre- and post-dissolution penetration resistance in normally loaded and uncemented clean sands shows that:

- Void ratio increases due to mineral dissolution. The change in void ratio is more pronounced in initially dense sediments. There is a terminal density or void ratio for dissolution; the void ratio after dissolution will not exceed this terminal void ratio regardless of the extent of dissolution. For the conditions of this study, the terminal void ratio for dissolution corresponds to a relative density of Dr ≈15% and is attained when dissolution exceeds a mass fraction loss of 10% (probably closer to 20%).
- Mineral dissolution decreases the cone tip resistance, particularly in initially dense soils. The drop in tip resistance increases with the extent of dissolution.

This effect is most pronounced in dense soils and it is minimal for initially loose soils.

- There is a single trend in penetration resistance vs. the void ratio at the time of penetration. Fabric and changes in lateral stress that accompany mineral dissolution do not affect this trend.

# CHAPTER 8

# EFFECT OF GRAIN DISSOLUTION ON SLOPE BEHAVIOR

## 8.1 Introduction

Mineral dissolution and re-precipitation are prevalent and persistent diagenetic processes. Many natural ground movements involve some form of solid phase loss, albeit not necessarily mineral dissolution. Solifluction is a widespread earth flow mechanism that occurs in slopes in periglacial conditions, where freezing during the cold season causes frost heave, and melting during the warm season causes water saturation in the thawed near surface. These repetitive changes lead to downslope ratcheting movement (Harris et al. 1997a, Matsuoka 2001). Solifluction may have contributed to the failure of Carsington dam along a pre-existing solifluction shear plane within the foundation layer (Potts et al. 1990, Skempton and Vaughan 1993).

Similarly, numerous studies suggest that gas hydrate dissociation is one of the major causes of large-scale submarine landslides (Sultan et al. 2004b, Nixon and Grozic 2007), for example, the Storegga Slide (Bugge et al. 1988, Bouriak et al. 2000) and the Tranaedjupet Slide (Laberg and Vorren 2000, Sultan et al. 2004a). Unlike conventional mineral dissolution, hydrate dissociation can occur in a relatively short time scale and in a progressive manner. A unique feature of hydrates is that the dissociation involves solid mass loss accompanied by gas generation and expansion, which results in excess pore pressure (Sultan et al. 2004b, Kwon et al. 2008). Gas hydrate destabilization can be naturally triggered by sea-level fluctuations (Maslin et al. 2005) and rising ocean temperature (Kvenvolden 1993), unavoidably in the vicinity of platform foundation piles (Kvenvolden 2000, Nixon and Grozic 2007), or purposely for gas production (Vanoudheusden et al. 2004).

The potential for slope instability due to solid phase loss could affect waste disposal, from organic waste to mine tailings and coal ash. Waste is vulnerable to dissolution and degradation over time because its components are suddenly exposed to a new environment outside equilibrium conditions, such as air, rainwater, different pressure and/or temperature. Heavy metals and acid drainage from mine tailings are telltale signals of ongoing dissolution processes (Macklin et al. 2003, Song et al. 2011). Likewise, some components in fly ash are highly soluble, such as CaO and $CaSO_4$ (Dudas 1981), and metals often leach from fly ash (El-Mogazi et al. 1988, Cetin et al. 2012). The dissolution of coal ash grains contributes to instability and collapse (Trivedi and Sud 2004); on the other hand, new minerals can precipitate including zeolite and phillipsite (Murayama et al. 2002, Querol et al. 2002). Dissolution and reprecipitation results in porous yet cemented sediments that are brittle and contractive and vulnerable to liquefaction once perturbed.

The purpose of this research is to explore the stability of sloping ground due to solid phase loss, such as mineral dissolution. The research approach combines experiments and discrete element simulations.

## 8.2 Experimental study

The small scale, 1g laboratory experiment described next was designed to explore the consequences of dissolution under realistic saturated conditions, where dissolution usually occurs.

### Device

The experimental study is implemented in a thin tank made of two parallel acrylic plates (width 18mm, separated by 13mm gap - Figure 8.1). The thick acrylic walls are firmly fixed to the spacer along all edges to minimize the horizontal deformation of walls

(maximum $\delta_h$=0.06mm). Three inlet ports at the bottom are covered with a flow diffuser that runs all along beneath the sediment to promote 1D flow (Figure 8.1).

**Test Procedure**

The sediment is a mixture of 90% sand (insoluble grains) and SF=10% salt (soluble grains). Sand and salt are dry mixed, and pluviated into the tank to form the slope at an initial angle of 30°. The model is slowly flooded with a saturated NaCl brine solution injected from the bottom (5 hrs). Gradual dissolution is controlled by progressively lowering the salt concentration in the injected fluid (duration: 3 days). The deformation of the slope is recorded using time-lapse photography with a 5 min time interval.

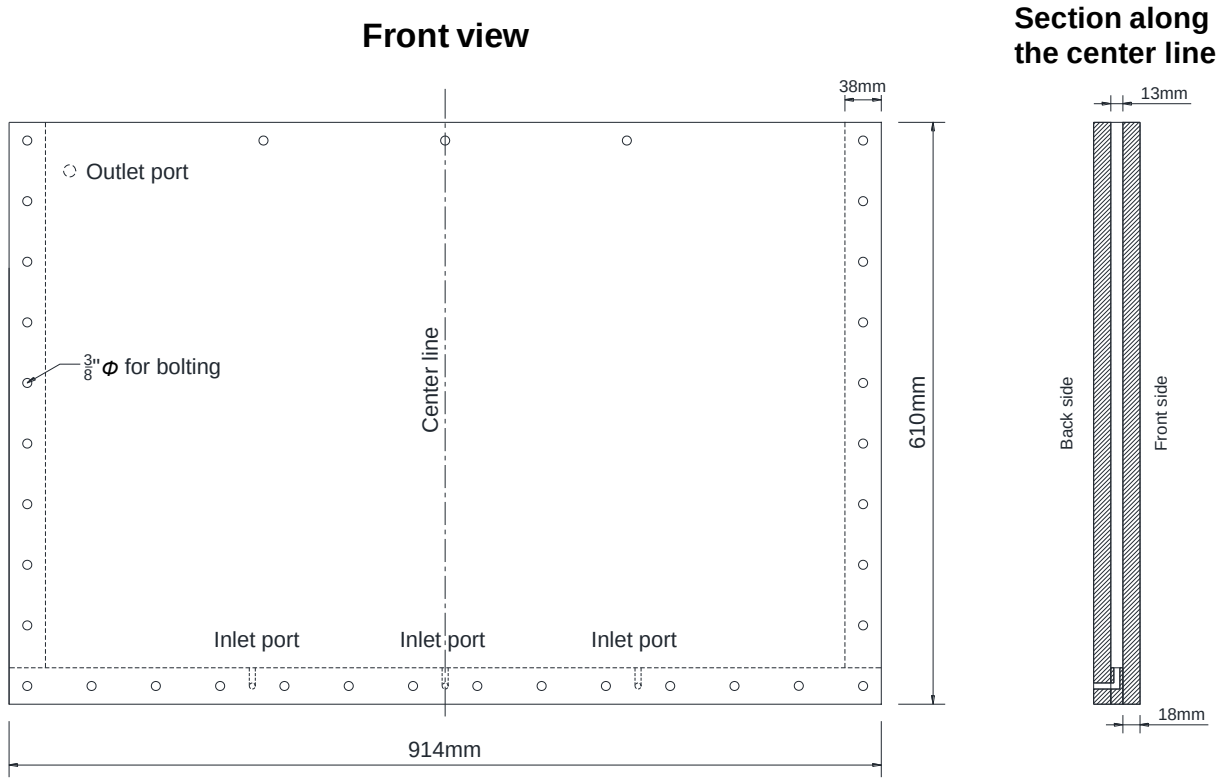


Figure 8.1 Experimental Study: Transparent two-dimensional tank used to explore the effects of dissolution on slope stability.

**Experimental Results**

Digital image correlation fails to provide adequate displacement fields due to lack of contrast. Instead, we manually traced displacements by following visible and persistent impurities detectable in high-resolution images.

Results in Figure 8.2a shows the comparative analysis of photographs gathered before dissolution and at the end of dissolution. Displacement vectors show that global vertical displacements prevails, their magnitude increases almost linearly with elevation, and horizontal displacements are more prominent near the slope surface. A sudden displacement is detectable when all recorded images are projected in a movie-form. The two consecutive images that capture this sudden displacement are compared in Figure 8.2b. Displacement vectors define a shallower failure that occurred within the 5 min picture interval in spite of the significant side friction along the walls.

The maximum possible time for this local failure is the time interval between photographs $\Delta t$=5 min; given a drainage length similar to the slide depth d=10 cm, then the coefficient of consolidation for drained conditions should be higher than $c_v > d^2/\Delta t = 0.333$ cm$^2$/sec, which corresponds to fine sands. Therefore, there is high probability that this local failure took place under undrained assuming that the duration was less than 5 min.

A possible sequence of events could involve (not simulated in the DEM study): dissolution, internal stress states approaches failure, i.e., $k_a$ (as shown in Chapters 2, 3, and 4), increased porosity, granular skeleton collapse, excess pore pressure generation, decreased shear strength and failure.

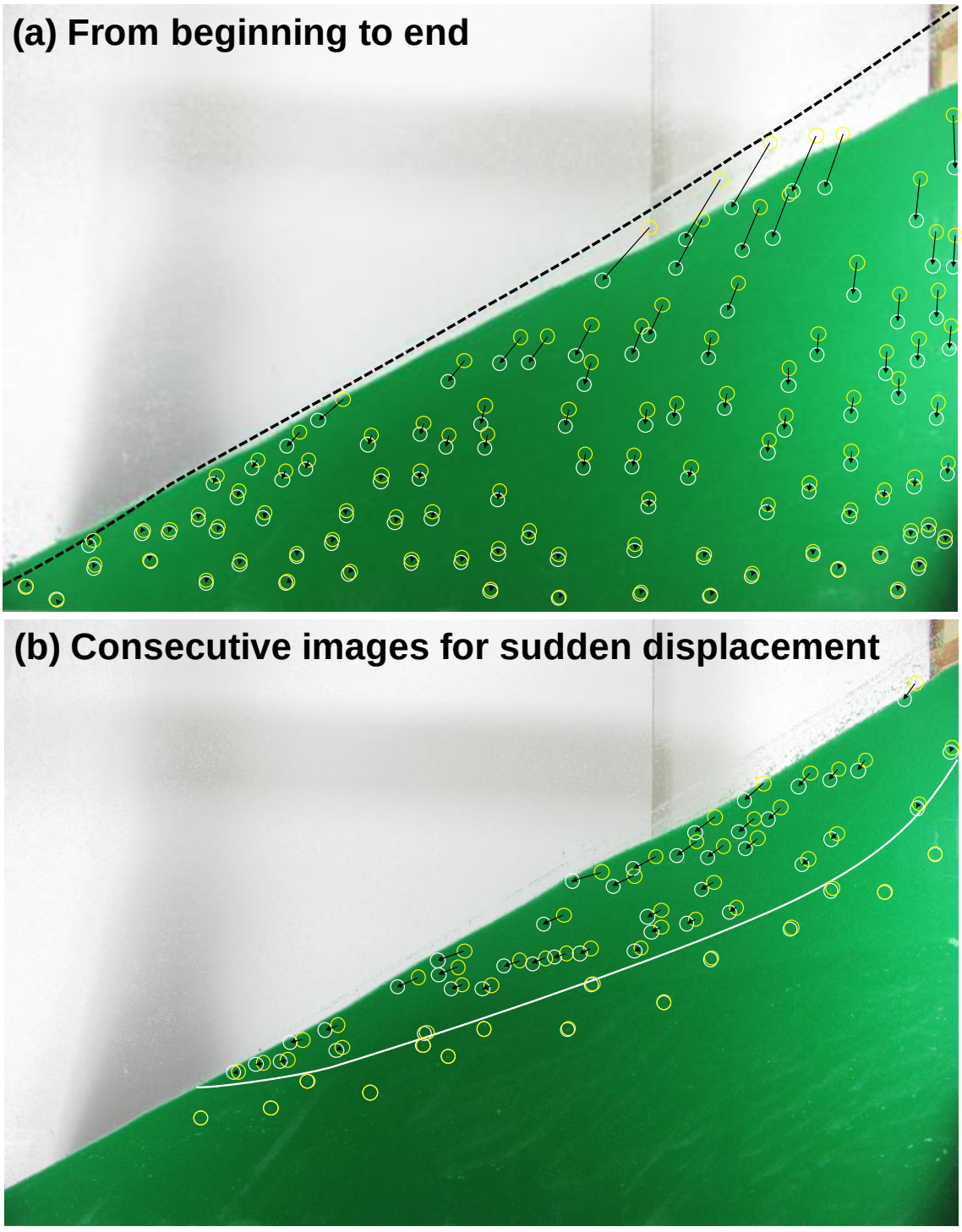


Figure 8.2 Experimental results. Displacement vectors at visually recognizable points (a) from the beginning to the end of dissolution – Note: the dotted line indicates the original slope surface. (b) Sudden shear localization observed during dissolution. The test was conducted with a SF=10% mass fraction of dissolvable particles. Note: displacement vectors are at the same scale in both (a) and (b).

## 8.3 Discrete Element Simulation

**Methodology**

The consequences of dissolution in sloping ground is further simulated using 2D-DEM simulations (PFC 2D – Itasca). Conditions are dry/drained and there are no side effects (i.e., acrylic walls). Table 8.1 shows the basic simulation environment and properties. The linear contact model is used in these 2D simulations. There is no friction between the sediment and the vertical lateral wall (Wall -Figure 8.3), and the friction coefficient is 0.5 between the sediment and the base (Base - Figure 8.3). The sediment is made of disks that are placed at random location within the model geometry and allowed to grow to their final target size (uniform size distribution). We simulate interlocking due to grain angularity by hindering the rotation of a preselected percentage of particles, HR=0%, 40%, and 80%. Soluble particles are homogeneously distributed and account for SF=25% of all particles. Dissolution is simulated by slowly and simultaneously reducing the size of all soluble particles.

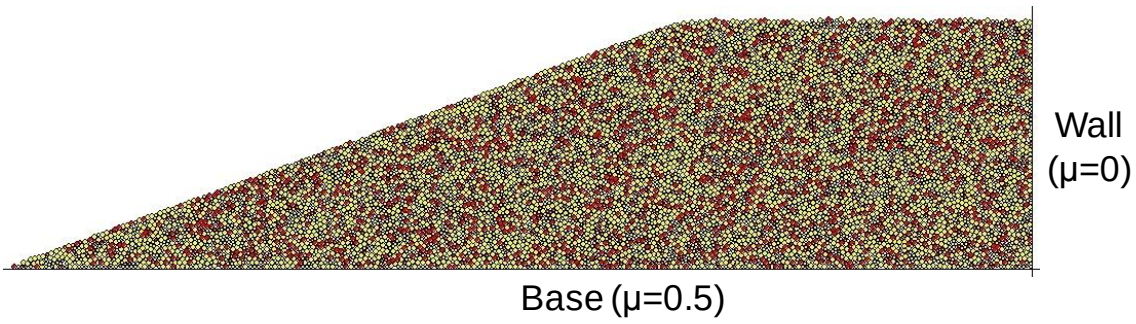


Figure 8.3 DEM Study - Specimen preparation. The case shown corresponds to a slope angle of 20°. Soluble particles are shown in red (SF=25%).

Table 8.1 DEM Simulation environment – PFC 2D. Parametric study.

| | Properties | Values |
|---|---|---|
| Disk | Initial radius of disks | Uniform size distribution ($R_{min}$=0.4mm, $R_{max}$=0.6mm) |
| | Number of disks | 10567 |
| | Mass density of disks | 2650 kg/m$^3$ |
| | Linear contact model | Normal stiffness $k_n$ =10$^8$ N/m |
| | | Shear stiffness $k_s$ = 10$^8$ N/m |
| | Inter-particle friction | 0.5 |
| | Fraction of soluble particles | 25% |
| | Hindered rotation HR | 0%, 40%, 80% |
| Boundary conditions | Initial slope angle | 20°, 30°, and 40° |
| | Particle-to-wall friction | 0.5 for Base and 0 for Wall |

Three initial slope angles are considered β=20°, 30°, and 40°. Figure 8.3 shows the initial geometry for a β=20° slope angle. The angle of repose $\Phi_r$ increases with the percentage of particles with hindered rotation: $\Phi_r$=20° for HR=0%, $\Phi_r$=35° for HR=40%, $\Phi_r$=51° for HR=80%. Therefore, only the slope with β=20° is stable when HR=0%, β=20° and 30° are stable slopes for HR=40%, and the three slopes β=20°, 30°, and 40° are stable when HR=80%.

**DEM Results**

*Contact force and internal fabric*. Contact forces form characteristic "chains" in granular materials. Force chains are shown before and after dissolution in Figure 8.5. A honeycomb-shaped topology characterizes the fabric after dissolution (Figure 8.5). Load-carrying granular arches develop around dissolving particles and the local porosity

increases (Notice that voids are next to strong chains). The honeycomb-shaped force chains are more prominent in sediments with greater interlocking, i.e., higher rotationally hindered particles HR. The final overall porosity increased in all cases. This distinct post-dissolution internal fabric anticipates a different sediment response upon further loading. In particular, the inherent shear loading the slope imposes on the sediment may trigger static liquefaction and flow given the higher contractive tendency in soils that experienced dissolution (Chapter 2).

*Displacement*. In agreement with experimental results, vertical settlement is the prevailing global deformation pattern (Figure 8.6). Sediments with higher soluble fraction SF and lower internal friction/interlocking HR experience more settlement (Note: the surface settlement normalized by the initial height is shown in Figure 8.6).

The horizontal component extracted from displacement vectors and plotted in Figure 8.7 show that horizontal displacements are largest near the slope free surface and decrease away from the slope surface without a sharp transition. Histograms of horizontal displacements after dissolution clearly show the bulk of the medium with mean horizontal displacement near zero, and one or more humps that represent the sliding mass (Figure 8.8). Steeper slopes in sediments with lower hindered rotation and friction angle show higher horizontal displacements following dissolution. The low horizontal displacement observed in sediments with high friction/interlocking reflects the relevance of rolling as a displacement mechanism in sloping ground.

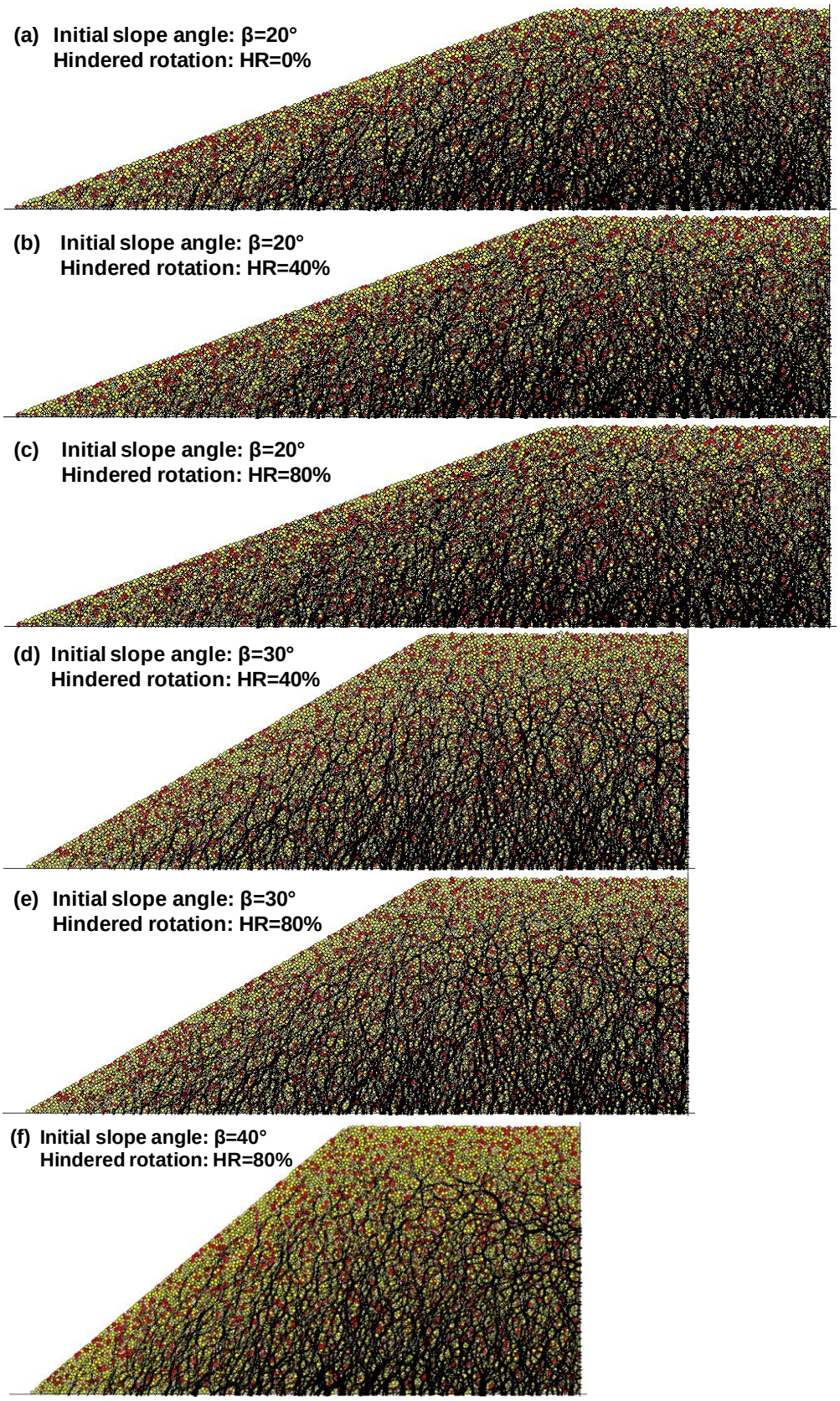


Figure 8.4 Contact force chains before dissolution – All cases shown at the same force scale.

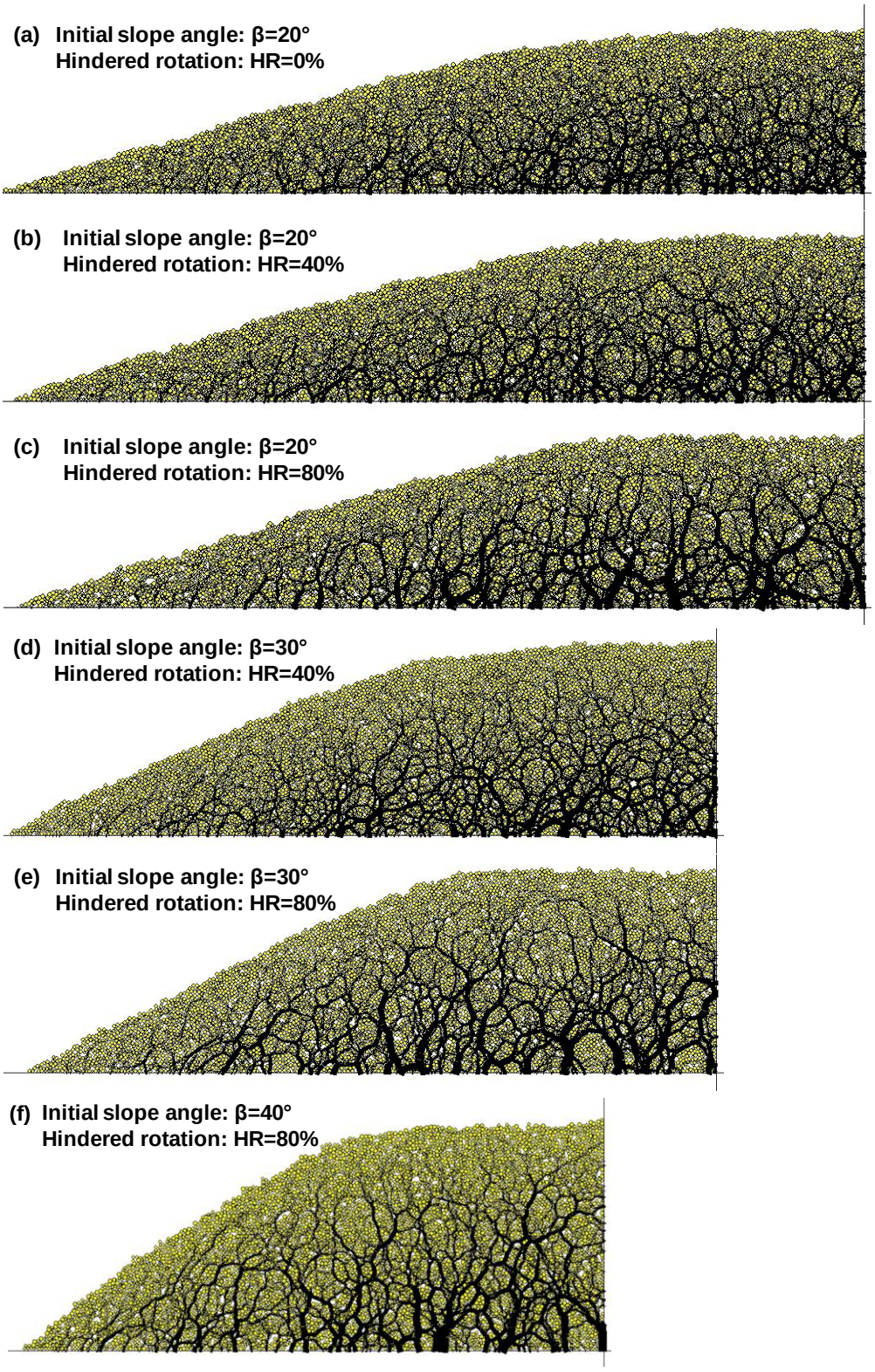


Figure 8.5 Contact force chains at the end of dissolution – All cases shown at the same force scale. Note: compare to Figure 8.4.

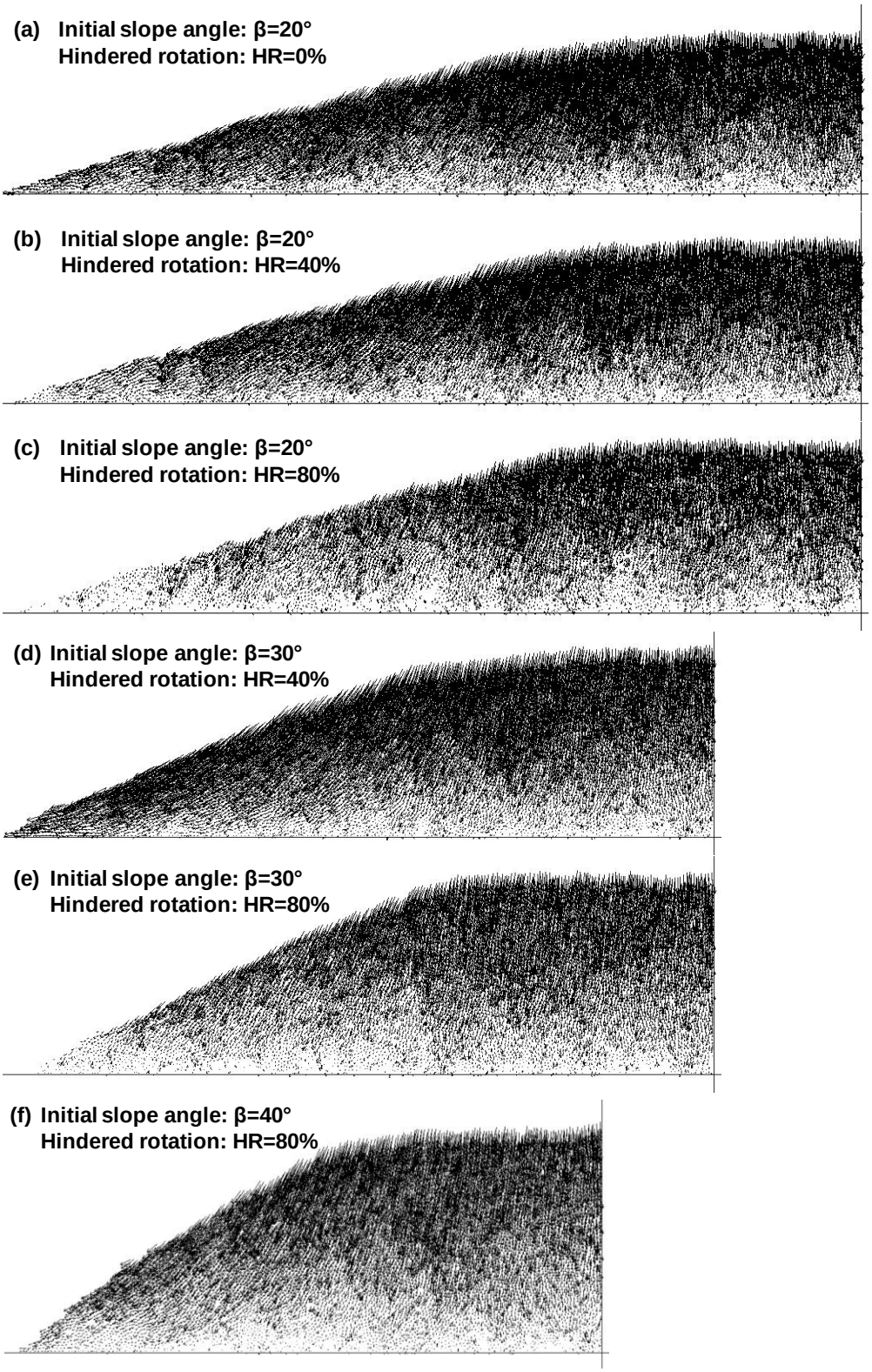


Figure 8.6 Displacement vectors at the end of dissolution - All cases shown at the same displacement vector scale.

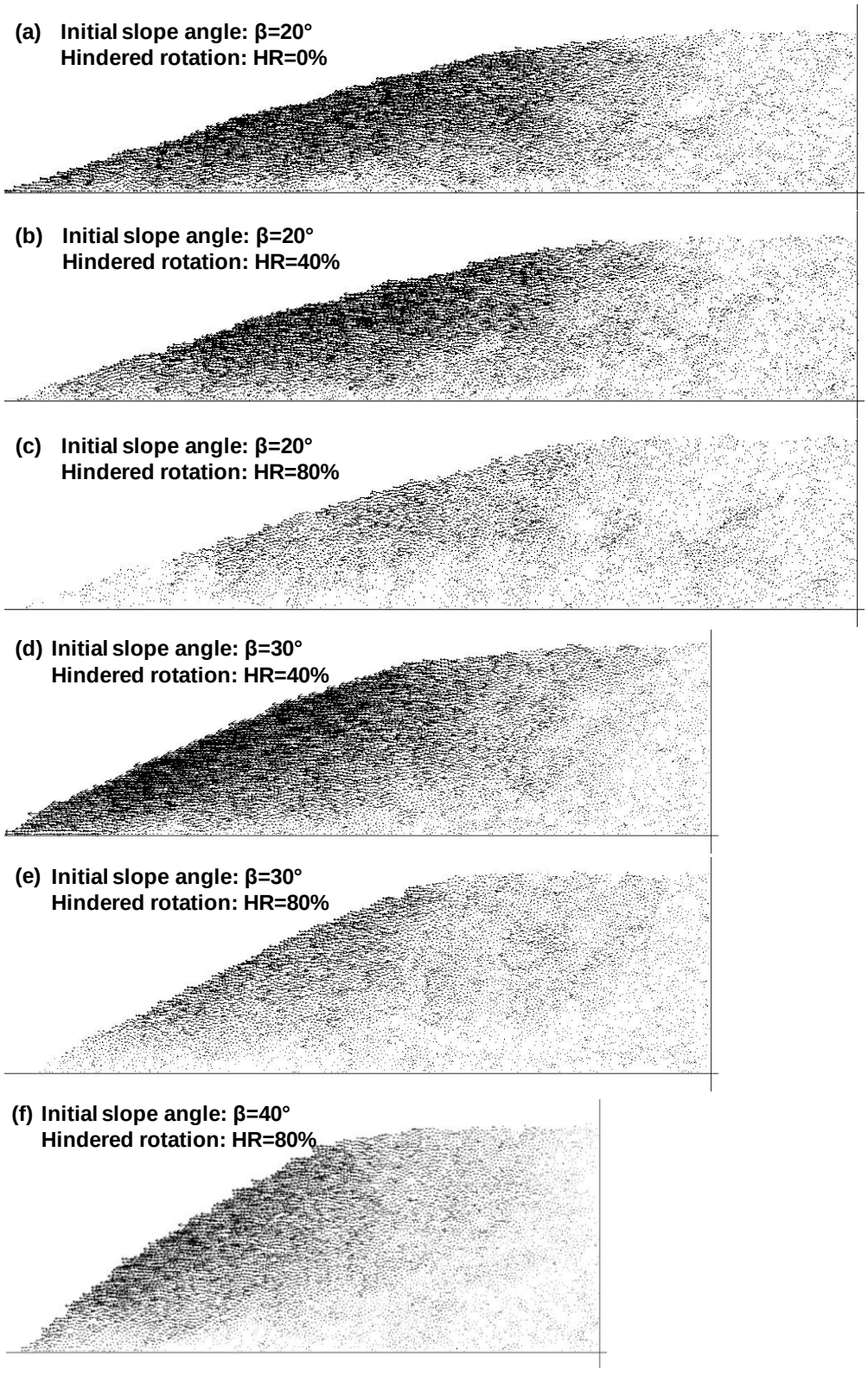


Figure 8.7 Horizontal component of the displacement vectors at the end of dissolution - All cases shown at the same displacement vector scale.

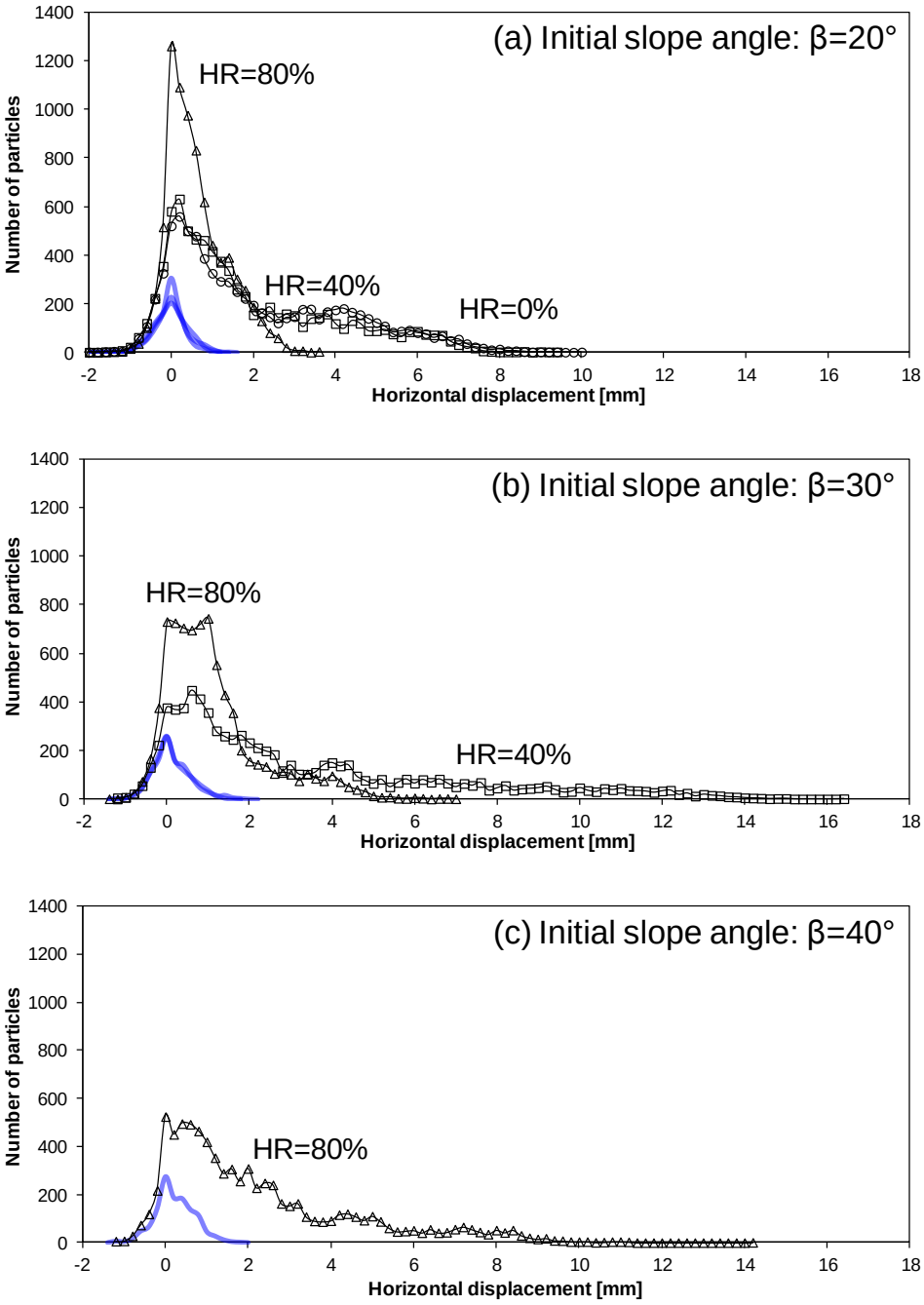


Figure 8.8 Histogram of horizontal displacements experienced by all non-dissolvable particles at the end of dissolution. Gray lines are used to draw histograms for the ~2000 particles closest to the right wall.

*Final slope angles*. Slope angles become smaller as dissolution progresses in all cases (Figure 8.9). Slope flattening is more pronounced in sediments with lower friction angle. The data are normalized by the angle of repose in each case and replotted in Figure 8.9b. A single trend $\beta_{final}/\beta_{repose}= 0.8(\beta_0/\beta_{repose})$ is observed when the lost solid fraction is SF=25%.

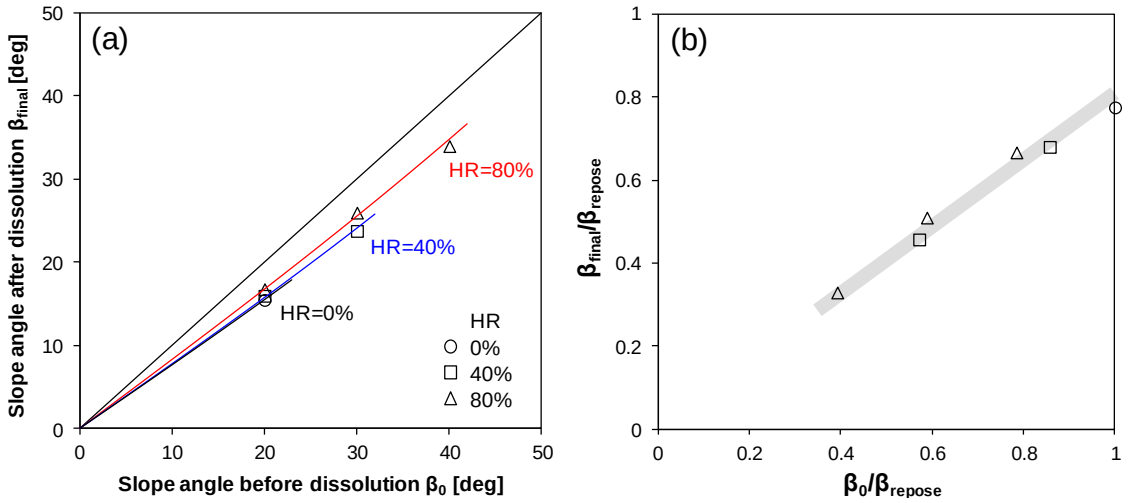


Figure 8.9 Comparison of the initial slope angle and the slope angle after dissolution for all cases (SF=25%). (a) Slope angle after dissolution vs. slope angle before dissolution. (b) Final slope angles normalized by angles of repose vs. initial slope angles normalized by angles of repose.

*Causal link between large remnant voids and force chains*. Careful inspection of images in Figure 8.5 reveals that large remnant voids are aligned near major contact force chains after dissolution, i.e., force arches develop near the dissolving particles. These voids contribute to the post-dissolution contractive behavior. The 2D cross correlation analysis between an image of large voids (Figure 8.10a - Note: grains are grown $\Delta R/R \approx 50\%$ without displacement to close small voids) and an image of contact force chains (Figure 8.10b) confirms that large voids are most developed about one particle diameter away (and typically below) major force chains (Figure 8.10c).

(a) Image of voids

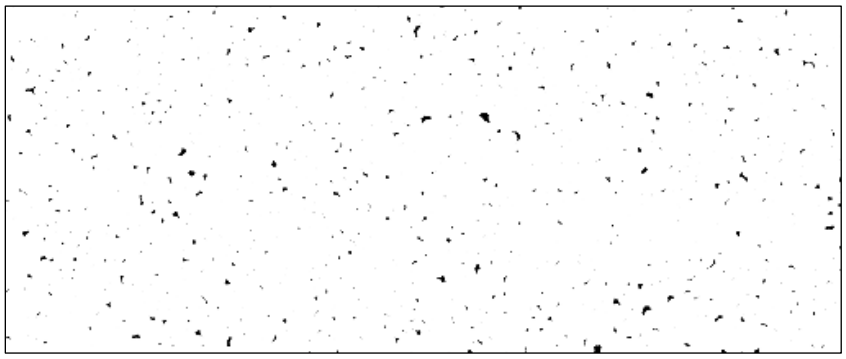

(b) Image of force chains

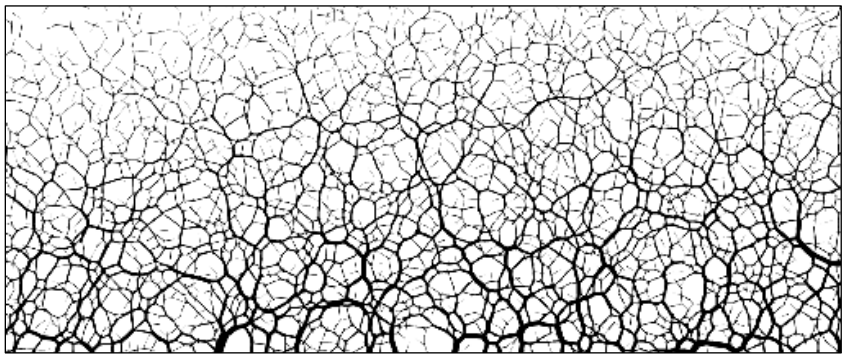

(c) 2D image cross correlation

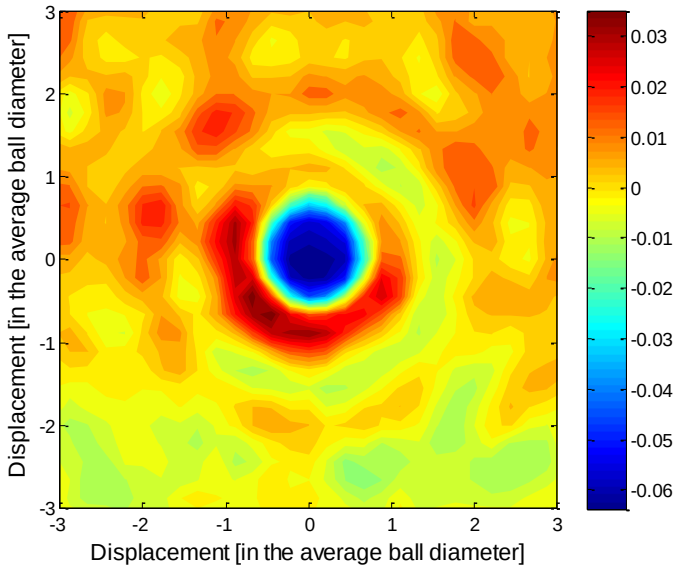


Figure 8.10 Study of the causal link between (a) large remnant voids and (b) force chains. (c) 2D cross-correlation.

## 8.4 Conclusions

We investigated the effect of grain dissolution on slope stability using an experimental study and discrete element simulations. Dissolution leads to significant slope movement. Global vertical settlements are the prevailing deformation pattern. Lateral movements are prominent near the slope free surface. Less interlocked sediments experience more displacements, both vertically and horizontally; during grain rearranging, the higher friction/interlocking minimizes rolling, which is the main mechanism for displacement in sloping ground. Lower initial slope angles induce less horizontal movements.

Slopes become flatter after dissolution; the reduction in slope angle is more pronounced in sediments with lower friction and higher initial slope angle. There is no shear localization or catastrophic failure during dissolution under drained condition. However, sudden undrained shear failure may take place during dissolution. A possible sequence of events could involve: dissolution and increase in porosity, internal stress approaches failure, structural collapse and pore pressure generation leading to static liquefaction.

Upon dissolution, load-carrying grain arches develop around dissolving particles, and a honeycomb-shaped contact force chain characterizes the high-porosity fabric after dissolution. The 2D cross correlation analysis confirms that large voids are aligned near major contact force chains after dissolution. This distinct internal fabric will have a different sediment response upon further loading; in particular, the inherent shear load bias in slopes may trigger liquefaction and flow.

# CHAPTER 9

# EFFECT OF DISSOLUTION ON LOAD-SETTLEMENT BEHAVIOR OF SHALLOW FOUNDATIONS

## 9.1 Introduction

A firm foundation can be compromised by dissolution-induced volume contraction. Examples extend beyond carbonates and karst terrain, and include foundations built in cold regions that are subject to ground thawing, structures sitting on hydrate bearing sediments and mineral dissolution in $CO_2$ geological storage projects. Even low reactivity minerals could affect critical infrastructure designed for a long time horizon, such as nuclear waste repositories.

There are other volume contraction phenomena similar to mineral dissolution in some respects. For example, collapsible soils contract during wetting (Haq and Kibria 1994, Rinaldi et al. 1998, Houston et al. 2001, Rodrigues and de Lollo 2007). While the behavior of foundations on collapsible soils has been extensively studied, there has been no attempt made to understand the effects of gradual mineral dissolution on shallow foundation behavior.

This chapter documents the study of grain dissolution effects on the load-settlement behavior of shallow foundations using the discrete element method. We consider the load-settlement response on a sediment that has already experienced dissolution and the settlement of a pre-loaded footing induced by ongoing dissolution.

## 9.2 Numerical simulation

The research is conducted using the discrete element method. The number of particles is limited by the available computation power. Previous scale effect studies are

used to guide the design of these numerical experiments: (a) the ratio of the footing width B to the soil mean grain size d should exceed B/d>25 (Kusakabe 1995, Lau and Bolton 2011). The depth from the footing to bedrock H should exceed H/B>3~5 to model infinite depth soil media (Cerato and Lutenegger 2006), and (b) the distance to lateral boundaries W should exceed B/W=5 (Davis and Selvadurai 2002).

**Simulation environment**

Figure 9.1 shows the test geometry and boundary conditions; simulation parameters are summarized in Table 9.1. The ratio of the sediment width W to the footing width B is W/B=5 (acknowledgingly marginal), the ratio of the footing width B to the average particle diameter d is B/d=20, and the ratio of the depth to the rigid bottom H to the footing width B is H/B=5. Even with these tight boundaries, this 2D model involves 10567 grains. We do not involve a symmetric geometry along the centerline because the discrete nature of the model causes grain alignment along straight boundaries. There is no friction between the sediment and the walls, or between the sediment and the footing plate.

Randomly positioned frictionless disks are allowed to grow to their target size (uniform size distribution). Then interparticle friction and gravity are turned on and grains experience self-weight under zero-lateral strain boundary conditions. Angularity and interlocking are captured by hindering the rotation of a selected fraction of particles: HR= 40% and 80%. The linear contact model is used in these 2D simulations.

Table 9.1 Simulation Parameters - Two dimensional discrete element code (PFC-2D)

| | | |
|---|---|---|
| Initial cell dimension | Height × Width | 10cm × 10cm |
| Disk | Initial radius of disks | Uniform size distribution ($R_{min}$=0.4mm, $R_{max}$=0.6mm) |
| | Number of disks | 10567 |
| | Mass density of disks | 2650 kg/m$^3$ |
| | Linear contact model | Normal stiffness $k_n$ =10$^8$ N/m |
| | | Shear stiffness $k_s$ = 10$^8$ N/m |
| | Inter-particle friction | 0.5 |
| | Hindered rotation HR | 0%, 80% |
| | Number of dissolvable particles | 1057 (10%) |
| Boundary conditions | Free surface boundary | |
| | Zero lateral strain | |
| | Particle-to-wall friction | 0 |

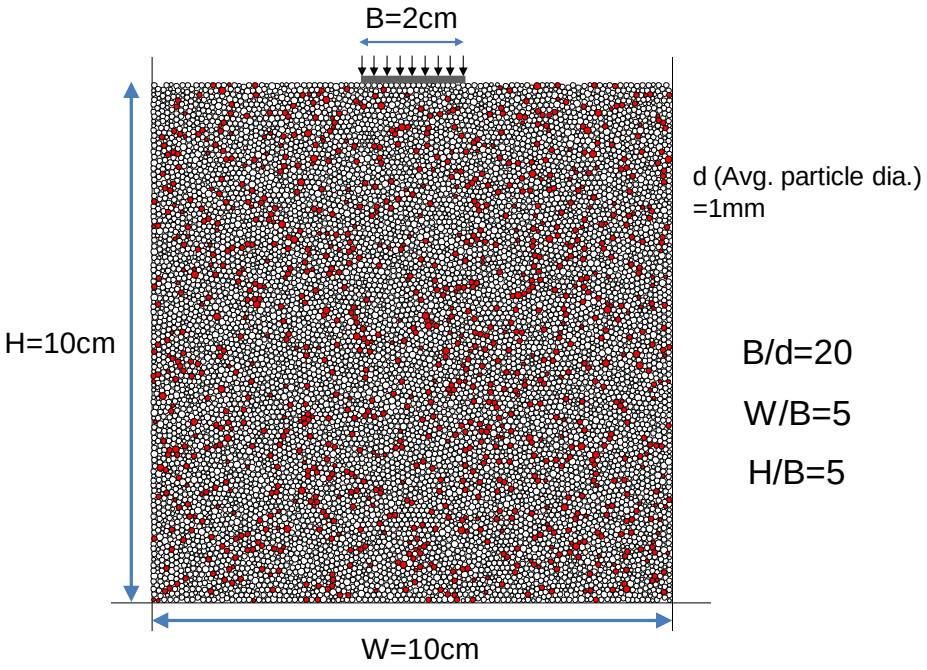


Figure 9.1 DEM Study - Problem geometry and boundary conditions. Note: Soluble particles are shown in red (SF=10%: 1057 out of 10567 disks).

**Procedure**

Load-settlement simulations are done in stress-controlled mode: the load is applied in small steps, and settlements follow.

Soluble particles are randomly selected (SF=10%). Dissolution under zero lateral strain $\varepsilon_h$=0 is simulated by gradually reducing the radius of all the soluble particles at the same rate. The ratio of the mean unbalanced force to the mean contact force is always smaller than 0.001 to ensure stable condition throughout the dissolution processes.

Simulations are performed for three load-dissolution histories: (1) virgin sediments loaded to failure, (2) load-settlement tests on sediments after dissolution, and (3) load to a factor of safety FS~2.5 followed by grain dissolution under constant vertical load.

## 9.3 Results

**Case 1: Virgin sediment: load before dissolution**

The load-deformation results "measured" for footings on soils with different angularity HR are plotted in Figure 9.2. The three cases show high initial stiffness.

Let's consider the footing bearing capacity $q_{ult}$ as the load at a normalized settlement $\delta$/B~20% (Lee and Salgado 2005, Mayne and Illingworth 2010, Loukidis and Salgado 2011). Similar to field tests, resistance continues to increase as the footing settles (Note: grains exert high forces against side boundaries as the footing settles down). Normalized results hide the pronounced effect hindered rotation has on bearing capacity, as anticipated from changes in friction angle (Chapter 2): as compared to free rotation, bearing capacity is ~4 times higher when hindered rotation is HR=40%, and 18 times higher when HR=80%. This result agrees with the exponential increase in analytical bearing capacity formula with increasing friction angle.

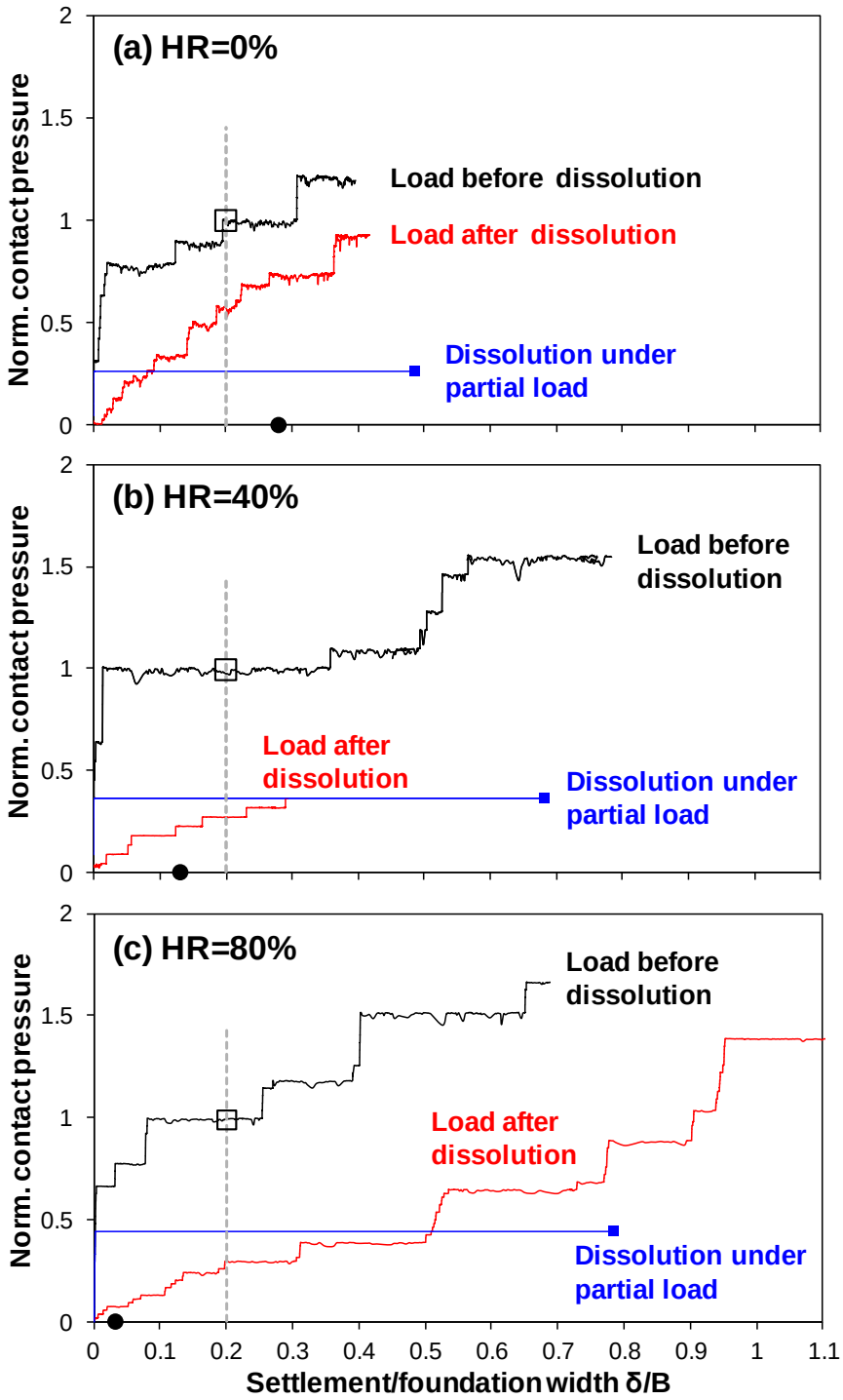


Figure 9.2 Contact pressure normalized by bearing capacity vs. settlement normalized by the foundation width - Stress-controlled Simulation. (a) HR=0%. (b) HR=40%. (c) HR=80%. Note: the filled black circle ● shown on the x-axis indicates the surface settlement in the absence of a footing observed at the end of dissolution, and □ assumes bearing capacities before dissolution at δ/B=0.2.

**Case 2: Load after dissolution**

The load-settlement response on post-dissolution sediments show lower stiffness (in agreement with lower stiffness obtained in Chapter 2), and gradual settlement from the onset of loading (Figure 9.2). While the asymptotic "ultimate capacity" may be similar, loading after dissolution requires much larger settlements to reach capacity than loading before dissolution. Furthermore inherent fabric differences observed in Chapters 4 and 8 may result in different capacities, even at very large settlements.

**Case 3: Dissolution under constant load**

Finally, consider the case when the footing is loaded on a rigid virgin soils (i.e., before dissolution) to a load q equivalent to a factor of safety $FS=q/q_{ult}\sim2.5$, to be later subjected to subsequent dissolution. The dissolution-induced settlement at constant load is shown in Figure 9.3 as a function of the size reduction $\Delta R/R_0$ in soluble particles. The trend is almost linear with size reduction; noticeably, most of the settlement occurs while $\Delta R/R_0 <60\%$.

Results superimposed on Figure 9.2 show that dissolution under an existing foundation load significantly enhances settlements; in fact, the footing settlements are much greater than those the footing experienced for the same load when dissolution took place before loading.

Figure 9.4 shows grain displacement vectors for all three load-dissolution histories, for the case of no hindered rotation HR=0%. Displacements during pre- and post-dissolution loading are concentrated near the footing (Figure 9.4a&b). Particle movements are high in dissolution under a constant load, affect deeper particles and cause significant upward flow at the sides.

The internal fabric in virgin sediments is characterized by low-porosity, densely distributed contact force chains (Figure 9.4a), which contribute to high stiffness and

bearing capacity. On the other hand, the post-dissolution sediments consist of a high-porosity honeycomb-shaped fabric that exhibits low stiffness and high compressibility (Figure 9.4b&c).

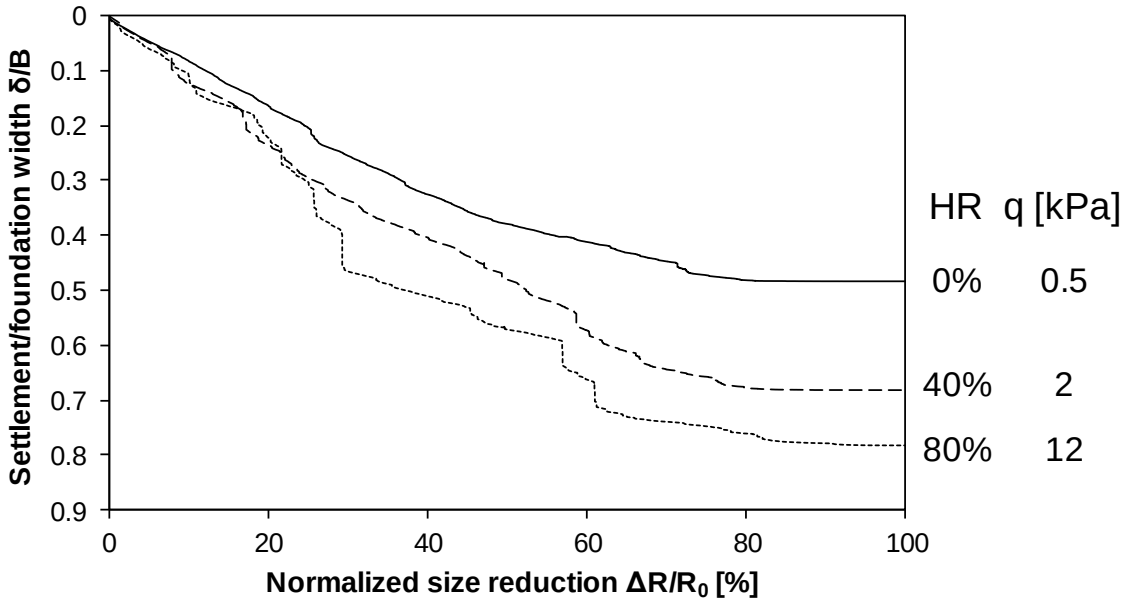


Figure 9.3 Settlement vs. normalized radius change for dissolution under constant loading for all three levels of imposed hindered rotation. Note that the three simulations are run at different loads, but a similar safety factor.

## 9.4 Conclusions

The load-settlement behavior of footings changes due to dissolution. The pre-dissolution sediment can pick up significant stress at relatively small settlement. On the other hand, post-dissolution sediments require higher settlements to mobilize resistance and to reach a bearing capacity. Grain interlocking significantly increases the overall load capacity on sediments either before or after dissolution. Settlement during dissolution under constant footing load is higher than when a foundation load is applied after dissolution.

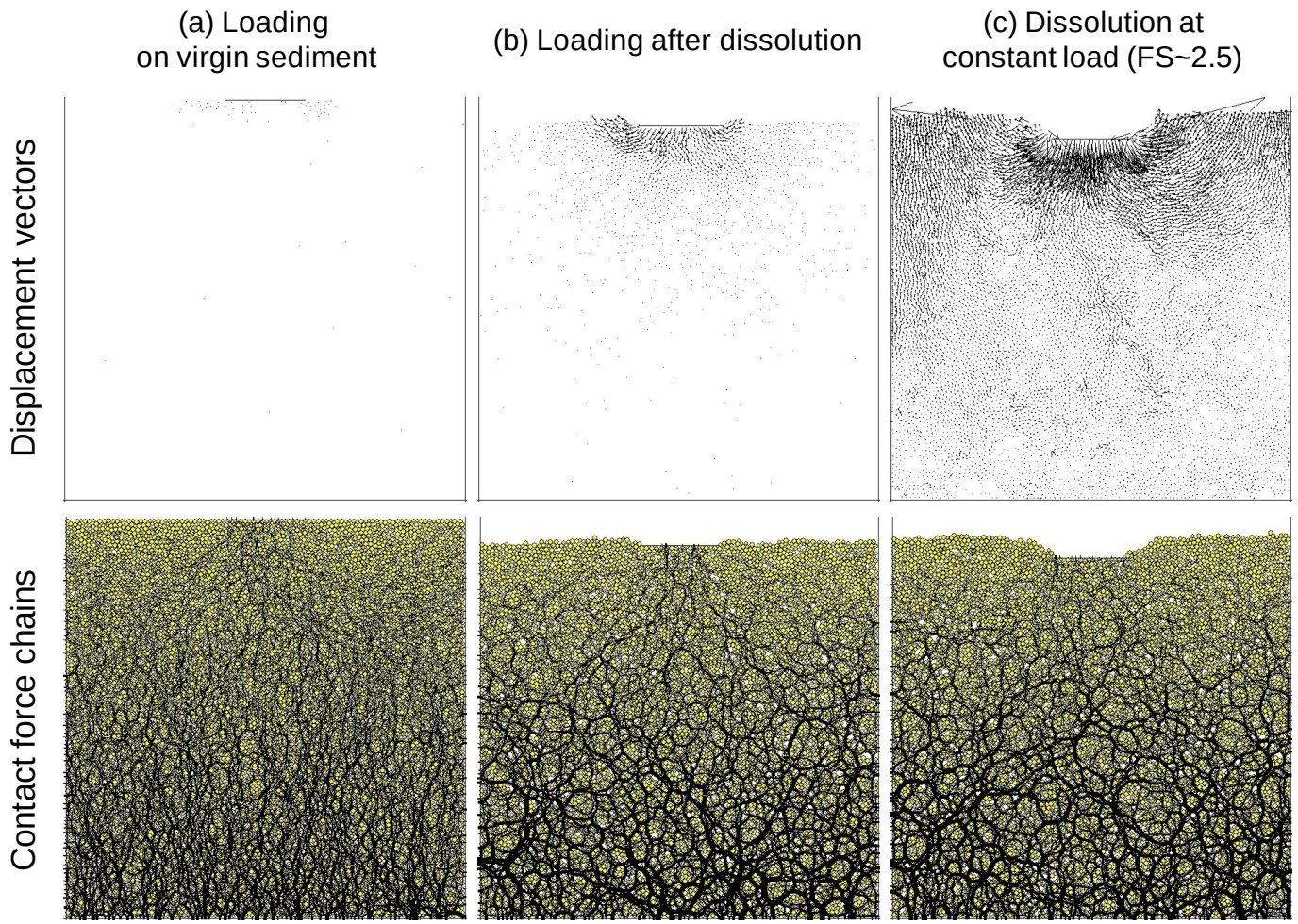


Figure 9.4 Contact force chains and displacement vectors for the three cases at the same foundation load q=0.5kPa (Case: hindered rotation HR=0%). a) Loading on virgin sediment. b) Loading after dissolution. c) Dissolution at constant loading. The displacement vectors and contact force chains are shown at the same scales.

# CHAPTER 10

# CONCLUSIONS

This research investigated the effect of dissolution on sediment behavior, through experimental and numerical methods. We chose to use a discrete element method as a numerical simulator to capture the inherent particle-scale phenomena. We identified five dissolution modes, and investigated sediment behavior for each of these dissolution modes in Chapters 2~6. We then investigated implications in engineering practice, such as in-situ soil characterizations, slope stability, and shallow foundations in Chapters 7~9. The main conclusions from this study follow.

*Dissolution of Randomly Distributed Soluble Grains – Post Dissolution $k_0$-Loading and Shear.*

- Sediment dissolution at zero lateral strain affects the equivalent global stress ratio $k_0$. Its evolution depends on the degree of particle interlocking as well as soluble fraction. While the equivalent global stress ratio $k_0$ increases in rounded particles, the value of $k_0$ may decrease to $k_a$ during mineral dissolution of sediments made of angular particles.
- While there is vertical settlement, there is also increase in porosity during dissolution.
- The coordination number decreases and preponderant interparticle force chains develop in the sediment.
- The post-dissolution sediments are more compressible than the original sediment. The increase in compressibility correlates with the extent of dissolution the sediment has experienced.

- Post-dissolution simple shear loading encounters lower shear stiffness and higher contractive tendency in sediments that have experienced more pronounced dissolution. Therefore, post dissolution sediments will be more vulnerable to liquefaction when sheared under undraind condition.

*Pressure-dependent Mineral Dissolution - Implications on Soil Formation.*

- A spontaneous shear localization is indicated by strong force chain formation/buckling and higher porosity inside the localization band, displacement discontinuities along the band, and temporal $k_0$ drop and recovery.
- A stronger contact force chain along the localization band may lead to more pressure solution along the shear localization.
- In the area outside of the localization zone, a homogeneous fabric of contact force chains begins to form when the shear localization start to be visible.
- The $k_0$ decreases as dissolution progresses. After reaching its lowest value, $k_0$ gradually recovers. Shear localization starts to be visible when $k_0$ starts to recover.
- The grain contacts increase and the mean contact force decreases during pressure solution, which is analogous to natural sediment compaction.

*Hydro-Chemo-Mechanical Coupling: Localized Mineral Dissolution.*

- Shear-waveform changes during dissolution under constant stress indicate significant stress field evolution inside the sediment.
- Localized dissolution is corroborated through post-dissolution tomographic studies and specimen dissection. The number of pipes at a cross section decreases away from inlet port. While calcite is completely dissolved along pipes, virtually no calcite is dissolved in stable parts around pipes.

- Discrete element simulations show that: the vertical displacement is quasi-linear relation with the progress of dissolution. Hindered rotation, i.e., a proxy for angularity and granular interlocking hinders vertical displacement.
- Porosity increases throughout the medium during dissolution, but it is larger in pipes.
- Localized pipe dissolution leads to the initial decrease of horizontal stress followed by a gradual recovery in angular-interlocked sediments.
- Marked force chains are preferentially vertical away from pipes, yet, they are preferentially horizontal within pipes. Horizontal contact forces inside pipes prevent the buckling of granular columns in the stable zones.
- Vertical forces increase rapidly in the host medium when dissolution starts in pipes. In the meantime, there is principal "equivalent" stress rotation in pipes. The peak equivalent global stress ratios reach the Coulomb failure condition in both the pipes and the host medium.

*Effect of Shallow Subsurface Volume Contraction on the Behavior of Overlying Soils.*

- Cavities are readily filled by surrounding grains that flow dominantly from the vertical direction, especially for higher friction/interlocking sediments, while horizontal inflow also becomes also significant for lower friction angle sediments. Sub-surface displacements propagate from the contracted volume to the surface within a fan-shaped region.
- Contact forces arch around the contracted region and the new grains that fill the cavity experience very low contact forces. This "effective void" is an inherent consequence of interparticle friction and rotational frustration; in fact, the force arch is more prominent for higher friction and/or denser sediments. The presence of grains in the effective void contributes to preventing the buckling of the surrounding force arches.

- The maximum surface settlement decreases with the normalized inclusion depth z/D, density and interlocking, yet, the affected width increases with increasing z/D and decreasing grain interlocking.
- The subsurface settlement volume per unit length is smaller than the volume lost in dilative, dense, and more frictional sediments, and porosity increases above the cavity. However, the surface sediment volume may exceed the subsurface volume loss in contractive, loose, and less interlocked sediments. Horizontal flow into the cavity reduces subsurface vertical displacement especially when deeper cavities form in looser and less interlocked sediments.

*Effect of Deep Regional Dissolution on Adjacent Soil Behavior.*

- Vertical contraction and changes in global porosity increase with the size of the contractible zone D/L. On the other hand, while normalized vertical displacement decreases for higher sediment friction angles, the porosity increases.
- The equivalent global stress ratio k0 increases with dissolution to eventually reach a steady value that can be as high as k≈0.7 to 0.8 (lower stress anisotropy for lower interlocking HR). An early drop in $k_0$ is measured for packings with high interlocking (e.g., HR=80%) and large contractible zone (e.g, D/L>0.4). Fluctuations in the equivalent global stress ratio $k_0$ trends hint to successive internal slippages.
- Grains adjacent to the contractible zone flow towards the shrinking volume as particles dissolve and no cavity remains after dissolution in agreement with the cohesionless nature of the sediment. Horizontal displacements prevail along the side of the contractible zone and are mostly responsible for filling the contractible space; vertical displacements are more dominant above and below the zone.
- Boundary forces arch around the dissolved region as a consequence of interparticle friction, rotational frustration, and virtual forces that prevent chain

buckling. Although there are no apparent cavities, the soils that flow into the inclusion carry little load, yet they play a critical role in preventing arch buckling. The area influenced by regional dissolution is significantly larger than the initial inclusion size. This will affect site characterization interpretation, such as penetration resistance data.

*Pre-dissolution and Post-dissolution Penetration Resistance.*

- Void ratio increases due to mineral dissolution. The change in void ratio is more pronounced in initially dense sediments. There is a terminal density or void ratio for dissolution; the void ratio after dissolution will not exceed this terminal void ratio regardless of the extent of dissolution. For the conditions of this study, the terminal void ratio for dissolution corresponds to a relative density of Dr ≈15% and is attained when dissolution exceeds a mass fraction loss of 10% (probably closer to 20%).
- Mineral dissolution decreases the cone tip resistance, particularly in initially dense soils. The drop in tip resistance increases with the extent of dissolution. This effect is most pronounced in dense soils and it is minimal for initially loose soils.
- There is a single trend in penetration resistance vs. the void ratio at the time of penetration. Fabric and changes in lateral stress that accompany mineral dissolution do not affect this trend.

*Effect of Grain Dissolution in Slope Behavior.*

- The honeycomb-shaped contact force chain characterizes the fabric after dissolution. This distinct fabric will have a different sediment response upon further loading, e.g., shear loading on the slope may trigger liquefaction and flow due to the highly contractive tendency.

- Dissolution leads to significant slope movement. While global vertical settlements are the prevailing deformation pattern, lateral movements are also prominent near the slope surface; thus, slopes become flatter after dissolution. Overall mass movement resembles a mass wasting-like behavior in nature.
- Sudden undrained shear along a clear localization plane can occur in saturated sediments, if the pore pressure dissipation time is longer than the collapse time at the point of contractive movement of sediments.

*Effect of Dissolution on Load-settlement Behavior of Shallow Foundations.*

- The pre-dissolution sediment can pick up significant stress at relatively small settlement. On the other hand, post-dissolution sediments require higher settlements to mobilize resistance and to reach a bearing capacity. Grain interlocking significantly increases the overall load capacity on sediments either before or after dissolution.
- Settlement during dissolution under constant footing load is higher than when a foundation load is applied after dissolution.

# APPENDIX A

# COORDINATION NUMBER

Coordination number indicates the average number of contacts per particle. PFC identifies "real" and "virtual" contacts as a function of particle overlap:

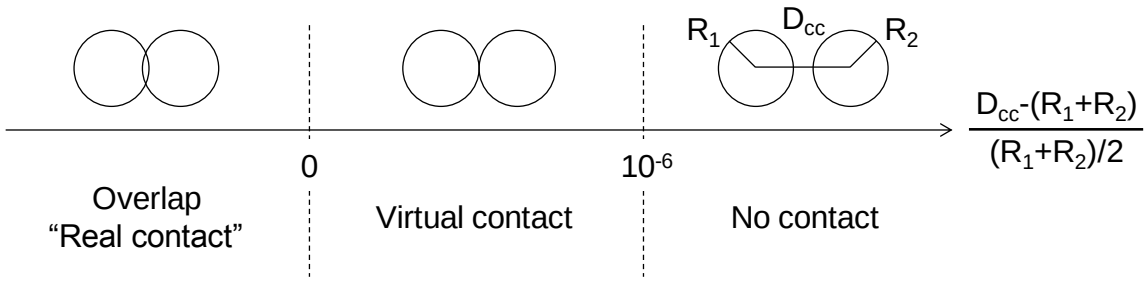


Therefore, two coordination numbers can be computed:

$$\mathbf{CN_{real}} = \frac{\mathbf{2 \cdot (Real\ contact\ number)}}{\mathbf{Number\ of\ particles}}$$

$$\mathbf{CN_{total}} = \frac{\mathbf{2 \cdot (Real\ contact\ number + Virtual\ contact\ number)}}{\mathbf{Number\ of\ particles}}$$

Note that the $CN_{real}$ value may not satisfy the minimum coordination for equilibrium.

# REFERENCES


Abduljauwad, S. N., and Al-Amoudi, O. S. B. (1995). "Geotechnical behaviour of saline sabkha soils." *Geotechnique*, 45(3), 425-445.

Ahmadi, M. M., Byrne, P. M., and Campanella, R. G. (2005). "Cone tip resistance in sand: modeling, verification, and applications." *Canadian Geotechnical Journal*, 42(4), 977-993.

Ahmadi, M. M., and Robertson, P. K. (2008). "A Numerical Study of Chamber Size and Boundary Effects on CPT Tip Resistance in NC Sand." *Scientia Iranica*, 15(5), 541-553.

Ahmed, M., and Iskander, M. (2011). "Analysis of Tunneling-Induced Ground Movements Using Transparent Soil Models." *Journal of Geotechnical and Geoenvironmental Engineering*, 137(5), 525-535.

Ambrozic, T., and Turk, G. (2003). "Prediction of subsidence due to underground mining by artificial neural networks." *Computers & Geosciences*, 29(5), 627-637.

Angevine, C. L., and Turcotte, D. L. (1983). "Porosity reduction by pressure solution - a theoretical-model for quartz arenites." *Geol. Soc. Am. Bull.*, 94(10), 1129-1134.

Angevine, C. L., Turcotte, D. L., and Furnish, M. D. (1982). "Pressure solution lithification as a mechanism for the stick-slip behavior of faults." *Tectonics*, 1(2), 151-160.

Attewell, P. B., and Farmer, I. W. (1974). "Ground Deformations Resulting from Shield Tunnelling in London Clay." *Canadian Geotechnical Journal*, 11(3), 380-395.

Bahuguna, P. P., Srivastava, A. M. C., and Saxena, N. C. (1991). "A critical review of mine subsidence prediction methods." *Mining Science and Technology*, 13(3), 369-382.

Bardet, J. P. (1994). "Observations on the effects of particle rotations on the failure of idealized granular materials." *Mechanics of Materials*, 18(2), 159-182.

Bardet, J. P., and Proubet, J. (1991). "A numerical investigation of the structure of persistent shear bands in granular media." *Geotechnique*, 41(4), 599-613.

Baxter, C. D. P., and Mitchell, J. K. (2004). "Experimental study on the aging of sands." *Journal of Geotechnical and Geoenvironmental Engineering*, 130(10), 1051-1062.

Been, K., Crooks, J. H. A., and Rothenburg, L. "A critical appraisal of CPT calibration chamber tests." *Proc., The 1st International Symposium on Penetration Testing, ISOPT-1*, Orlando, 1, 651-661.

Bell, F. G., Stacey, T. R., and Genske, D. D. (2000). "Mining subsidence and its effect on the environment: some differing examples." *Environmental Geology*, 40(1-2), 135-152.

Berest, P., Brouard, B., Feuga, B., and Karimi-Jafari, M. (2008). "The 1873 collapse of the Saint-Maximilien panel at the Varangeville salt mine." *International Journal of Rock Mechanics and Mining Sciences*, 45(7), 1025-1043.

Bobet, A. (2001). "Analytical solutions for shallow tunnels in saturated ground." *J. Eng. Mech.-ASCE*, 127(12), 1258-1266.

Boggus, M., and Crawfis, R. "Explicit Generation of 3D Models of Solution Caves for Virtual Environments." *Proc., the 2009 International Conference on Computer Graphics and Virtual Reality*, Las Vegas, NV.

Bouriak, S., Vanneste, M., and Saoutkine, A. (2000). "Inferred gas hydrates and clay diapirs near the Storegga Slide on the southern edge of the Voring Plateau, offshore Norway." *Marine Geology*, 163(1-4), 125-148.

Bugge, T., Belderson, R. H., and Kenyon, N. H. (1988). "The Storegga Slide." *Philosophical Transactions of the Royal Society of London Series a-Mathematical Physical and Engineering Sciences*, 325(1586), 357-388.

Buijse, M. A. (2000). "Understanding wormholing mechanisms can improve acid treatments in carbonate formations." *Spe Production & Facilities*, 15(3), 168-175.

Burland, J. B., Standing, J. R., and Jardine, F. M. "Assessing the risk of building damage due to tunnelling - Lessons from the Jubilee Line Extension, London." *Proc., 14th Southeast Asian Geotechnical Conference* Hong Kong, A A Balkema Publishers, 17-44.

Cartwright, J. (2011). "Diagenetically induced shear failure of fine-grained sediments and the development of polygonal fault systems." *Marine and Petroleum Geology*, 28(9), 1593-1610.

Cartwright, J., James, D., and Bolton, A. (2003). "The genesis of polygonal fault systems; a review." *Geological Society, London, Special Publications*, 216(1), 223-243.

Cartwright, J. A., and Dewhurst, D. N. (1998). "Layer-bound compaction faults in fine-grained sediments." *Geol. Soc. Am. Bull.*, 110(10), 1242-1257.

Castellanza, R., and Nova, R. (2004). "Oedometric tests on artificially weathered carbonatic soft rocks." *Journal of Geotechnical and Geoenvironmental Engineering*, 130(7), 728-739.

Cerato, A. B., and Lutenegger, A. J. (2006). "Bearing capacity of square and circular footings on a finite layer of granular soil underlain by a rigid base." *Journal of Geotechnical and Geoenvironmental Engineering*, 132(11), 1496-1501.

Cetin, B., Aydilek, A. H., and Li, L. (2012). "Experimental and numerical analysis of metal leaching from fly ash-amended highway bases." *Waste management (New York, N.Y.)*, 32(5), 965-978.

Chang, M. F., Yu, G., Na, Y. M., and Choa, V. (2006). "Evaluation of relative density profiles of sand fill at a reclaimed site." *Canadian Geotechnical Journal*, 43(9), 903-914.

Chen, J. W., and Juang, C. H. (1996). "Determination of Drained Friction Angle of Sands from CPT." *Journal of Geotechnical Engineering*, 122(5), 374.

Chen, L. T., Poulos, H. G., and Loganathan, N. (1999). "Pile responses caused by tunneling." *Journal of Geotechnical and Geoenvironmental Engineering*, 125(3), 207-215.

Cohen, C. E., Ding, D., Quintard, M., and Bazin, B. (2008). "From pore scale to wellbore scale: Impact of geometry on wormhole growth in carbonate acidization." *Chem. Eng. Sci.*, 63(12), 3088-3099.

Cooper, M. L., Chapman, D. N., Chan, A. H. C., and Rogers, C. D. F. "Tunnel-induced ground movements and their effects on existing tunnels." *Proc., The fifteenth International Conference on Soil Mechanics and Geotechnical Engineering Vols 1-3*, Istanbul, Turkey, A A Balkema Publishers, 1483-1486.

Cooper, M. L., Chapman, D. N., Rogers, C. D. F., and Chan, A. H. C. (2002). "Movements in the Piccadilly Line tunnels due to the Heathrow Express construction." *Geotechnique*, 52(4), 243-257.

Cowan, J. C., and Weintritt, D. J. (1976). *Water-Formed Scale Deposits*, Gulf Publishing, Houston, Texas, 596 pages.

Craft, D. (2005). "Seepage chemistry manual." US Department of the Interior, Bureau of Reclamation, Dam Safety Technology Development Program., Denver, Colorado, 164 pages.

Craft, D., Cain, C., and Sullivan, C. (2006). "Seepage geochemistry and mineral dissolution at Clark Canyon dam, Pick-Sloan Missouri Basin Project, East Bench Unit, Montana.", US Department of the Interior, Bureau of Reclamation, Denver, Colorado, 48 pages.

Criss, E. M., Criss, R. E., and Osburn, G. R. (2008). "Effects of stress on cave passage shape in karst terranes." *Rock Mechanics and Rock Engineering*, 41(3), 499-505.

Croize, D., Bjorlykke, K., Jahren, J., and Renard, F. (2010). "Experimental mechanical and chemical compaction of carbonate sand." *J. Geophys. Res.-Solid Earth*, 115.

Cui, X., Miao, X., Wang, J. a., Yang, S., Liu, H., Song, Y., Liu, H., and Hu, X. (2000). "Improved prediction of differential subsidence caused by underground mining." *International Journal of Rock Mechanics and Mining Sciences*, 37(4), 615-627.

Cundall, P. A., and Strack, O. D. L. (1979). "Discrete numerical-model for granular assemblies." *Geotechnique*, 29(1), 47-65.

Daccord, G., Lenormand, R., and Lietard, O. (1993). "Chemical dissolution of a porous-medium by a reactive fluid .1. Model for the wormholing phenomenon." *Chem. Eng. Sci.*, 48(1), 169-178.

Davis, R. O., and Selvadurai, A. P. S. (2002). *Plasticity and geomechanics*, Cambridge University Press, Cambridge, UK; New York, 287 pages.

De Boer, R. B. (1977). "On the thermodynamics of pressure solution--interaction between chemical and mechanical forces." *Geochimica et Cosmochimica Acta*, 41(2), 249-256.

De Boer, R. B., Nagtegaal, P. J. C., and Duyvis, E. M. (1977). "Pressure solution experiments on quartz sand." *Geochimica et Cosmochimica Acta*, 41(2), 257-264.

Dewers, T., and Hajash, A. (1995). "Rate laws for water-assisted compaction and stress-induced water-rock interaction in sandstones." *J. Geophys. Res.-Solid Earth*, 100(B7), 13093-13112.

Dreybrodt, Romanov, and Gabrovsek (2002). "Karstification below dam sites: a model of increasing leakage from reservoirs." *Environmental Geology*, 42(5), 518-524.

Dudas, M. J. (1981). "Long-term leachability of selected elements from fly ash." *Environmental Science & Technology*, 15(7), 840-843.

Durelli, A. J., Parks, V. J., and Feng, H. C. (1966). "Stresses around an elliptical hole in a finite plate subjected to axial loading." *Journal of Applied Mechanics*, 33(1), 192-195.

Durney, D. W. (1972). "Solution-transfer, an important geological deformation mechanism." *Nature*, 235(5337), 315-317.

Eggleton, R. A., Foudoulis, C., and Varkevisser, D. (1987). "Weathering of basalt - changes in rock chemistry and mineralogy." *Clay Clay Min.*, 35(3), 161-169.

El-Mogazi, D., Lisk, D. J., and Weinstein, L. H. (1988). "A review of physical, chemical, and biological properties of fly ash and effects on agricultural ecosystems." *Sci. Total Environ.*, 74(0), 1-37.

Elliott, D. (1973). "Diffusion flow laws in metamorphic rocks." *Geol. Soc. Am. Bull.*, 84(8), 2645-2664.

Espinoza, D., Kim, S., and Santamarina, J. (2011). "CO2 geological storage - Geotechnical implications." *KSCE Journal of Civil Engineering*, 15(4), 707-719.

Espinoza, D. N., and Santamarina, J. C. (2011). "P-wave monitoring of hydrate-bearing sand during $CH_4$-$CO_2$ replacement." *Int. J. Greenh. Gas Control*, 5(4), 1031-1038.

Etheridge, M. A., Wall, V. J., Cox, S. F., and Vernon, R. H. (1984). "High fluid pressures during regional metamorphism and deformation: implications for mass-transport and deformation mechanisms." *J. Geophys. Res.*, 89(NB6), 4344-4358.

Fam, M. A., Cascante, G., and Dusseault, M. B. (2002). "Large and small strain properties of sands subjected to local void increase." *Journal of Geotechnical and Geoenvironmental Engineering*, 128(12), 1018-1025.

Fang, Y. S., Lin, J. S., and Su, C. S. (1994). "An estimation of ground settlement due to shield tunneling by the Peck-Fujita method." *Canadian Geotechnical Journal*, 31(3), 431-443.

Fares, N. F. (1987). "Green's functions for plane-layered elastostatic and viscoelastic regions with application to 3-D crack analysis." Ph.D., Massachusetts Institute of Technology.

Ford, D., and Williams, P. W. (2007). *Karst hydrogeology and geomorphology*, Wiley, Chichester, West Sussex, England, 562.

Fowler, A. C., and Yang, X. S. (1999). "Pressure solution and viscous compaction in sedimentary basins." *J. Geophys. Res.-Solid Earth*, 104(B6), 12989-12997.

Fredd, C. N., and Fogler, H. S. (1998). "Influence of transport and reaction on wormhole formation in porous media." *AIChE Journal*, 44(9), 1933-1949.

Freij-Ayoub, R., Tan, C., Clennell, B., Tohidi, B., and Yang, J. H. (2007). "A wellbore stability model for hydrate bearing sediments." *Journal of Petroleum Science and Engineering*, 57(1-2), 209-220.

Ghafghazi, M., and Shuttle, D. (2008). "Interpretation of sand state from cone penetration resistance." *Geotechnique*, 58(8), 623-634.

Gillieson, D. S. (1996). *Caves : processes, development, and management*, Blackwell Publishers, Oxford, 324.

Goldich, S. S. (1938). "A Study in Rock-Weathering." *The Journal of Geology*, 46(1), 17-58.

Golfier, F., Zarcone, C., Bazin, B., Lenormand, R., Lasseux, D., and Quintard, M. (2002). "On the ability of a Darcy-scale model to capture wormhole formation during the dissolution of a porous medium." *J. Fluid Mech.*, 457, 213-254.

Goodman, R. E. (1989). *Introduction to rock mechanics*, John Wiley & Sons, New York, 562.

Gratier, J. P., Guiguet, R., Renard, F., Jenatton, L., and Bernard, D. (2009). "A pressure solution creep law for quartz from indentation experiments." *J. Geophys. Res.-Solid Earth*, 114.

Groshong, R. H. (1975). "Strain, fractures, and pressure solution in natural single-layer folds." *Geol. Soc. Am. Bull.*, 86(10), 1363-1376.

Gutiérrez, F., Desir, G., and Gutiérrez, M. (2003). "Causes of the catastrophic failure of an earth dam built on gypsiferous alluvium and dispersive clays (Altorricón, Huesca Province, NE Spain)." *Environmental Geology*, 43(7), 842-851.

Hansen, J. B. (1970). "A revised and extended formula for bearing capacity." *Danish Geotechnical Institute, Copenhagen*, Bul. No. 28, 21 pp.

Haq, B. U., Hardenbol, J., and Vail, P. R. (1987). "Chronology of Fluctuating Sea Levels since the Triassic." *Science*, 235(4793), 1156-1167.

Haq, I. U., and Kibria, S. "Engineering characteristics of arid soils." *Proc., 1st International Symposium on Engineering Characteristics of Arid Soils* London, England, A A Balkema, 91-93.

Harris, C., Davies, M. C. R., and Coutard, J. P. (1997a). "Rates and processes of periglacial solifluction: An experimental approach." *Earth Surf. Process. Landf.*, 22(9), 849-868.

Harris, M. K., Thayer, P. A., and Amidon, M. B. (1997b). "Sedimentology and depositional environments of middle Eocene terrigenous-carbonate strata, southeastern Atlantic Coastal Plain, USA." *Sedimentary Geology*, 108(1-4), 141-161.

He, W. W., Hajash, A., and Sparks, D. (2003). "Creep compaction of quartz aggregates: Effects of pore-fluid flow - A combined experimental and theoretical study." *Am. J. Sci.*, 303(2), 73-93.

Hellmann, R., Gratier, J. P., and Chen, T. "Mineral-water interactions and stress: pressure solution of halite aggregates." *Proc., Water-Rock Interaction, Arehart & Hulston (eds)*, Rotterdam, Balkema, 873-878.

Herrera, M. C., Lizcano, A., and Santamarina, J. C. (2007). "Colombian volcanic ash soils, Characterization and Engineering Properties of Natural Soils." Taylor & Francis, Singapore, 2385-2409.

Hibsch, C., Cartwright, J., Hansen, D. M., Gaviglio, P., Andre, G., Cushing, M., Bracq, P., Juignet, P., Benoit, P., and Allouc, J. (2003). "Normal faulting in chalk: tectonic stresses vs. compaction-related polygonal faulting." *Subsurface Sediment Mobilization*, P. VanRensbergen, R. R. Hillis, A. J. Maltman, and C. K. Morley, eds., Geological Soc Publishing House, Bath, 291-308.

Hoefner, M. L., and Fogler, H. S. (1988). "Pore evolution and channel formation during flow and reaction in porous media." *AIChE Journal*, 34(1), 45-54.

Holtzman, R., Silin, D. B., and Patzek, T. W. (2008). "Micromechanics of Hydrate Dissociation in Marine Sediments by Grain-Scale Simulations." *SPE Western Regional and Pacific Section AAPG Joint Meeting, 29 March-2 April 2008*, Society of Petroleum Engineers, Bakersfield, California, USA, 7 pages.

Houlsby, G. T., and Hitchman, R. (1988). "Calibration chamber tests of a cone penetrometer in sand." *Geotechnique*, 38(1), 39-44.

Houston, S. L., Houston, W. N., Zapata, C. E., and Lawrence, C. (2001). "Geotechnical engineering practice for collapsible soils." *Geotechnical and Geological Engineering*, 19(3), 333-355.

Huang, M. S., Zhang, C. R., and Li, Z. (2009). "A simplified analysis method for the influence of tunneling on grouped piles." *Tunn. Undergr. Space Technol.*, 24(4), 410-422.

Hunt, R. E. (2007). *Geologic hazards: a field guide for geotechnical engineers*, CRC Press Boca Raton, USA, 323

Ismael, N. F., and Mollah, M. A. (1998). "Leaching effects on properties of cemented sands in Kuwait." *Journal of Geotechnical and Geoenvironmental Engineering*, 124(10), 997-1004.

Iwasaki, K., Tanizawa, F., and Zhou, S. "Cone resistance and liquefaction strength of sand." *Proc., The 1st International Symposium on Penetration Testing.*, Orlando, 785-791.

Iwashita, K., and Oda, M. (1998). "Rolling resistance at contacts in simulation of shear band development by DEM." *J. Eng. Mech.-ASCE*, 124(3), 285-292.

Iwashita, K., and Oda, M. (2000). "Micro-deformation mechanism of shear banding process based on modified distinct element method." *Powder Technology*, 109(1-3), 192-205.

Jacobsz, S. W., Standing, J. R., Mair, R. J., Hagiwara, T., and Sugiyama, T. (2004). "Centrifuge modelling of tunnelling near driven piles." *Soils Found.*, 44(1), 49-56.

Jamiolkowski, M., Ladd, C. C., Germaine, J. T., and Lancellotta, R. (1985). "New developments in field and laboratory testing of soils." *Proc., the 11th International Conference on Soil Mechanics and Foundation Engineering*, San Francisco, Balkema Pub., Rotterdam, 1, 57-153.

Jamiolkowski, M., Lo Presti, D. C. F., and Manassero, M. (2003). "Evaluation of relative density and shear strength of sands from CPT and DMT." *Soil Behavior and Soft Ground Construction*, J. T. Germaine, T. C. Sheahan, and R. V. Whitman, eds., Amer Soc Civil Engineers, New York, 201-238.

Jang, J., Narsilio, G. A., and Santamarina, J. C. (2011). "Hydraulic conductivity in spatially varying media—a pore-scale investigation." *Geophys. J. Int.*, 184(3), 1167-1179.

Jarvis, T. (2003). "The money pit: karst failure of Anchor Dam." *Evaporite karst and engineering/environmental problems in the United States*, K. S. Johnson, and J. T. Neal, eds., Okla Geol Surv Circ 109:271–278.

Johnson, K. (2008). "Gypsum-karst problems in constructing dams in the USA." *Environmental Geology*, 53(5), 945-950.

Johnson, K. S. (2003a). "Evaporite-karst problems in the United States." *Evaporite karst and engineering/environmental problems in the United States*, K. S. Johnson, and J. T. Neal, eds., Okla Geol Surv Circ 109:1–20.

Johnson, K. S. (2003b). "Gypsum karst and abandonment of the Upper Mangum Damsite in southwestern Oklahoma." *Evaporite karst and engineering/environmental problems in the United States*, K. S. Johnson, and J. T. Neal, eds., Okla Geol Surv Circ 109:85–94.

Jung, J. W., Santamarina, J. C., and Soga, K. (2012). "Stress-strain response of hydrate-bearing sands: Numerical study using discrete element method simulations." *J. Geophys. Res.-Solid Earth*, 117.

Kim, C. Y., Bae, G. J., Hong, S. W., Park, C. H., Moon, H. K., and Shin, H. S. (2001). "Neural network based prediction of ground surface settlements due to tunnelling." *Comput. Geotech.*, 28(6-7), 517-547.

Klar, A., Marshall, A. M., Soga, K., and Mair, R. J. (2008). "Tunneling effects on jointed pipelines." *Canadian Geotechnical Journal*, 45(1), 131-139.

Klar, A., Vorster, T. E. B., Soga, K., and Mair, R. J. (2005). "Soil-pipe interaction due to tunnelling: comparison between Winkler and elastic continuum solutions." *Geotechnique*, 55(6), 461-466.

Kruyt, N. P., and Rothenburg, L. (2006). "Shear strength, dilatancy, energy and dissipation in quasi-static deformation of granular materials." *J. Stat. Mech.-Theory Exp.*, 7, 1-13.

Kuhn, M. R., and Mitchell, J. K. (1993). "New perspectives on soil-creep." *J. Geotech. Eng.-ASCE*, 119(3), 507-524.

Kulhawy, F. H., and Mayne, P. W. (1990). "Manual on Estimating Soil Properties for Foundation Design." *Report EPRI EL-6800*, Electric Power Research Institute, Palo Alto, 306 pp.

Kusakabe, O. (1995). "Chapter 6: Foundations." *Geotechnical centrifuge technology*, R. N. Taylor, ed., Blackie Academic & Professional, London, 118–167.

Kvenvolden, K. A. (1993). "Gas Hydrates - Geological Perspective and Global Change." *Reviews of Geophysics*, 31(2), 173-187.

Kvenvolden, K. A. (2000). "Gas Hydrate and Humans." *Annals of the New York Academy of Sciences*, 912(1), 17-22.

Kwon, T. H., Cho, G. C., and Santamarina, J. C. (2008). "Gas hydrate dissociation in sediments: Pressure-temperature evolution." *Geochem. Geophys. Geosyst.*, 9.

Laberg, J. S., and Vorren, T. O. (2000). "The Traenadjupet Slide, offshore Norway - morphology, evacuation and triggering mechanisms." *Marine Geology*, 171(1-4), 95-114.

Lau, C. K., and Bolton, M. D. (2011). "The bearing capacity of footings on granular soils. II: Experimental evidence." *Geotechnique*, 61(8), 639-650.

Lawrence, G. W. M., and Cartwright, J. A. (2009). "The initiation of sliding on the mid Norway margin in the Møre Basin." *Marine Geology*, 259(1–4), 21-35.

Le Guen, Y., Renard, F., Hellmann, R., Brosse, E., Collombet, M., Tisserand, D., and Gratier, J. P. (2007). "Enhanced deformation of limestone and sandstone in the presence of high P-co2 fluids." *J. Geophys. Res.-Solid Earth*, 112(B5).

Lee, J., and Salgado, R. (2005). "Estimation of bearing capacity of circular footings on sands based on cone penetration test." *Journal of Geotechnical and Geoenvironmental Engineering*, 131(4), 442-452.

Lee, K. M., Rowe, R. K., and Lo, K. Y. (1992). "Subsidence owing to tunnelling. I. Estimating the gap parameter." *Canadian Geotechnical Journal*, 29(6), 929-940.

Lee, M.-J., Choo, H., Kim, J., and Lee, W. (2010). "Effect of artificial cementation on cone tip resistance and small strain shear modulus of sand." *Bulletin of Engineering Geology and the Environment*, 1-9.

Lee, R. G., Turner, A. J., and Whitworth, L. J. "Deformations caused by tunneling beneath a piled structure." *Proc., Thirteenth International Conference on Soil Mechanics and Foundation Engineering, Proceedings, Vol 2*, 873-878.

Leeman, E. R. (1971). "The CSIR "doorstopper" and triaxial rock stress measuring instruments." *Rock Mechanics and Rock Engineering*, 3(1), 25-50.

Lehner, F. K. (1990). "Thermodynamics of rock deformation by pressure solution." *Deformation Process in Minerals, Ceramics, and Rocks*, D. J. Barber, and P. G. Meredith, eds., Unwin-Hyman, Boston, 296-333.

Lehner, F. K. (1995). "A model for intergranular pressure solution in open systems." *Tectonophysics*, 245(3-4), 153-170.

Leon, E., Gassman, S. L., and Talwani, P. (2006). "Accounting for soil aging when assessing liquefaction potential." *Journal of Geotechnical and Geoenvironmental Engineering*, 132(3), 363-377.

Li, W. (2008). "Prediction of surface settlement due to the displacement of soft zones." *Proc., The Fourth International conference on Deformation Characterixtics of Geomaterials in Atlanta*, Atlanta, I O S Press, 413-419.

Lin, S., Whittaker, B. N., and Reddish, D. J. (1992). "Application of asymmetrical influence functions for subsidence prediction of gently inclined seam extractions." *Int. J. Rock Mech. Min. Sci.*, 29(5), 479-490.

Loganathan, N., and Poulos, H. G. (1998). "Analytical prediction for tunneling-induced ground movements in clays." *Journal of Geotechnical and Geoenvironmental Engineering*, 124(9), 846-856.

Loukidis, D., and Salgado, R. (2011). "Effect of relative density and stress level on the bearing capacity of footings on sand." *Geotechnique*, 61(2), 107-119.

Macklin, M. G., Brewer, P. A., Balteanu, D., Coulthard, T. J., Driga, B., Howard, A. J., and Zaharia, S. (2003). "The long term fate and environmental significance of contaminant metals released by the January and March 2000 mining tailings dam failures in Maramures County, upper Tisa Basin, Romania." *Applied Geochemistry*, 18(2), 241-257.

Mair, R. J., Taylor, R. N., and Bracegirdle, A. (1993). "Subsurface settlement profiles above tunnels in clays." *Geotechnique*, 43(2), 315-320.

Mansour, Z., Chik, Z., and Taha, M. R. "On Soil Collapse Potential Evaluation." *Proc., International Conference on Construction and Building Technology 2008*, 21-32.

Mansour, Z. M., Taha, M. R., Chik, Z., and Kasa, A. (2009). "Leaching of Lisan Marl and its consequences on the engineering behavior of dikes, studied by finite elements modeling." *Environ. Earth Sci.*, 59(4), 891-900.

Marcus, R., Feldman, D., Nelson, D., and Rosen, C. J. (2009). "Fundamentals of Osteoporosis." Elsevier, Burlington, 552.

Marshall, A. M., Klar, A., and Mair, R. J. (2010). "Tunneling beneath Buried Pipes: View of Soil Strain and Its Effect on Pipeline Behavior." *Journal of Geotechnical and Geoenvironmental Engineering*, 136(12), 1664-1672.

Maslin, M., Vilela, C., Mikkelsen, N., and Grootes, P. (2005). "Causes of catastrophic sediment failures of the Amazon Fan." *Quat. Sci. Rev.*, 24(20-21), 2180-2193.

Matsuoka, N. (2001). "Solifluction rates, processes and landforms: a global review." *Earth-Sci. Rev.*, 55(1-2), 107-134.

Mayne, P. W., and Illingworth, F. (2010). "Direct CPT method for footing response in sands using a database approach." *2nd International Symposium on Cone Penetration Testing.* Huntington Beach, CA, USA.

Mayne, P. W., and Kulhawy, F. H. "Calibration chamber database and boundary effects correction for CPT data." *Proc., The 1st Int. Symp. on Calibration Chamber Testing (ISOCCTI).* Potsdam, New York, Elsevier, 257-264.

Mayne, P. W., Peuchen, J., and Bouwmeester, D. "Estimation of soil unit weight from CPTs." *Proc., Proc. 2nd International Symposium on Cone Penetration Testing, (CPT'10, Huntington Beach, CA)*, 2, 169-176.

McDowell, G. R., and Khan, J. J. (2003). "Creep of granular materials." *Granular Matter*, 5(3), 115-120.

Mesri, G., Feng, T. W., and Benak, J. M. (1990). "Postdensification penetration resistance of clean sands." *J. Geotech. Eng.-ASCE*, 116(7), 1095-1115.

Meyerhof, G. G. (1963). "Some recent research on the bearing capacity of foundations." *Canadian Geotechnical Journal* 1(1), pp. 16-26.

Mirghasemi, A. A., Rothenburg, L., and Matyas, E. L. (2002). "Influence of particle shape on engineering properties of assemblies of two-dimensional polygon-shaped particles." *Geotechnique*, 52(3), 209-217.

Mitchell, J. K. (1986). "Practical problems from surprising soil behavior." *J. Geotech. Eng.-ASCE*, 112(3), 255-289.

Mohamed, A., and Gutierrez, M. (2010). "Comprehensive study of the effects of rolling resistance on the stress-strain and strain localization behavior of granular materials." *Granular Matter*, 12(5), 527-541.

Montes-Hernandez, G., Renard, F., Geoffroy, N., Charlet, L., and Pironon, J. (2007). "Calcite precipitation from CO2-H2O-Ca(OH)(2) slurry under high pressure of CO2." *J. Cryst. Growth*, 308(1), 228-236.

Murayama, N., Yamamoto, H., and Shibata, J. (2002). "Mechanism of zeolite synthesis from coal fly ash by alkali hydrothermal reaction." *International Journal of Mineral Processing*, 64(1), 1-17.

Narsilio, G. A., and Santamarina, J. C. (2008). "Terminal densities." *Geotechnique*, 58(8), 669-674.

Neaupane, K. M., and Adhikari, N. R. (2006). "Prediction of tunneling-induced ground movement with the multi-layer perceptron." *Tunn. Undergr. Space Technol.*, 21(2), 151-159.

Niemeijer, A., Elsworth, D., and Marone, C. (2009). "Significant effect of grain size distribution on compaction rates in granular aggregates." *Earth and Planetary Science Letters*, 284(3-4), 386-391.

Niemeijer, A., Marone, C., and Elsworth, D. (2008). "Healing of simulated fault gouges aided by pressure solution: Results from rock analogue experiments." *J. Geophys. Res.-Solid Earth*, 113(B4).

Nixon, M. F., and Grozic, J. L. H. (2007). "Submarine slope failure due to gas hydrate dissociation: a preliminary quantification." *Canadian Geotechnical Journal*, 44(3), 314-325.

Nystrom, P. G., Willoughby, R. H., and Price, L. K. (1991). "Cretaceous and Tertiary stratigraphy of the upper Coastal Plain, South Carolina." University of Tennessee Press, Knoxville, Tenn., p. 221–240.

Okochi, H., Kameda, H., Hasegawa, S.-i., Saito, N., Kubota, K., and Igawa, M. (2000). "Deterioration of concrete structures by acid deposition -- an assessment of the role of rainwater on deterioration by laboratory and field exposure experiments using mortar specimens." *Atmospheric Environment*, 34(18), 2937-2945.

Park, K. H. (2005). "Analytical solution for tunnelling-induced ground movement in clays." *Tunn. Undergr. Space Technol.*, 20(3), 249-261.

Parkin, A. K., and Lunne, T. (1982). "Boundary effects in the laboratory calibration of a cone penetrometer for sand." *Proc., The 2nd European Symposium of Penetration Testing*, Amsterdam, Norwegian Geotechnical Institute, vol 2, 761-768.

Payton, C. C., and Hansen, M. N. (2003). "Gypsum karst in southwestern Utah: failure and reconstruction of Quail Creek Dike." *Evaporite karst and engineering/environmental problems in the United States*, K. S. Johnson, and J. T. Neal, eds., Okla Geol Surv Circ 109:293–303.

Pearson, R. M. (2002). "Gypsum karst of the Lykins Formation and effects for Colorado Front Range water projects; Horsetooth and Carter Lake Reservoirs." *Geol Soc Am Abstr Programs*, 34(6), 216.

Peck, R. B. (1969). "Deep Excavations and Tunneling in Soft Ground." *Proc., 7th International Conference on Soil Mechanics and Foundation Engineering, Mexico City, Mexico, State-of-the-Art*, Mexico City, Mexico, 225-290.

Polyak, V. J., and Güven, N. (2000). "Clays in caves of the Guadalupe Mountains, New Mexico." *Journal of Cave and Karst Studies*, 62(2), 120-126.

Potts, D. M., Dounias, G. T., and Vaughan, P. R. (1990). "Finite-element analysis of progressive failure of Carsington embankment." *Geotechnique*, 40(1), 79-101.

Puppala, A. J., Acar, Y. B., and Tumay, M. T. (1995). "Cone Penetration in Very Weakly Cemented Sand." *Journal of Geotechnical Engineering*, 121(8), 589-600.

Querol, X., Moreno, N., Umaña, J. C., Alastuey, A., Hernández, E., López-Soler, A., and Plana, F. (2002). "Synthesis of zeolites from coal fly ash: an overview." *International Journal of Coal Geology*, 50(1–4), 413-423.

Rad, N., and Tumay, M. (1986). "Effect of Cementation on the Cone Penetration Resistance of Sand: A Model Study." *Geotech. Test. J.*, 9(3), 117-125.

Raj, R. (1982). "Creep in polycrystalline aggregates by matter transport through a liquid-phase." *J. Geophys. Res.*, 87(NB6), 4731-4739.

Ren, G., Reddish, D. J., and Whittaker, B. N. (1987). "Mining subsidence and displacement prediction using influence function methods." *Mining Science and Technology*, 5(1), 89-104.

Renard, F., Gundersen, E., Hellmann, R., Collombet, M., and Le Guen, Y. (2005). "Numerical modeling of the effect of carbon dioxide sequestration on the rate of pressure solution creep in limestone: Preliminary results." *Oil Gas Sci. Technol.*, 60(2), 381-399.

Rinaldi, V. A., Redolfi, E. R., and Santamarina, J. C. "Characterization of collapsible soils with combined geophysical and penetration testing." *Proc., 1st International Conference on Site Characterization (ISC 98)*, Atlanta, GA, A A Balkema Publishers, 581-588.

Robertson, P. K. (2009). "Interpretation of cone penetration tests - a unified approach." *Canadian Geotechnical Journal*, 46(11), 1337-1355.

Robertson, P. K., and Wride, C. E. (1998). "Evaluating cyclic liquefaction potential using the cone penetration test." *Canadian Geotechnical Journal*, 35(3), 442-459.

Rodrigues, R., and de Lollo, J. (2007). "Influence of domestic sewage leakage on the collapse of tropical soils." *Bulletin of Engineering Geology and the Environment*, 66(2), 215-223.

Rodriguez-Roa, F. (2002). "Ground subsidence due to a shallow tunnel in dense sandy gravel." *Journal of Geotechnical and Geoenvironmental Engineering*, 128(5), 426-434.

Rothenburg, L., and Bathurst, R. J. (1993). "Influence of particle eccentricity on micromechanical behavior of granular-materials." *Mechanics of Materials*, 16(1-2), 141-152.

Rothwell, R. G., Thomson, J., and Kahler, G. (1998). "Low-sea-level emplacement of a very large Late Pleistocene 'megaturbidite' in the western Mediterranean Sea." *Nature*, 392(6674), 377-380.

Rowe, P. W. (1969). "Relation between shear strength of sands in triaxial compression plane strain and direct shear." *Geotechnique*, 19(1), 75-86.

Rowe, R. K., Lo, K. Y., and Kack, G. J. (1983). "A method of estimating surface settlement above tunnels constructed in soft ground." *Canadian Geotechnical Journal*, 20(1), 11-22.

Rutter, E. H. (1983). "Pressure solution in nature, theory and experiment." *J. Geol. Soc.*, 140(SEP), 725-740.

Salgado, R., Mitchell, J. K., and Jamiolkowski, M. (1997). "Cavity expansion and penetration resistance in sand." *Journal of Geotechnical and Geoenvironmental Engineering*, 123(4), 344-354.

Salgado, R., Mitchell, J. K., and Jamiolkowski, M. (1998). "Calibration chamber size effects on penetration resistance in sand." *Journal of Geotechnical and Geoenvironmental Engineering*, 124(9), 878-888.

Santamarina, J. C., Klein, K. A., and Fam, M. A. (2001). *Soils and waves - Particulate materials behavior, characterization and process monitoring*, Wiley, Chichester, England, 488.

Schlesinger, W. H. (1991). *Biogeochemistry: an analysis of global change*, XI+443P.

Schmertmann, J. H. (1991). "The mechanical aging of soils." *J. Geotech. Eng.-ASCE*, 117(9), 1288-1330.

Schnaid, F., and Houlsby, G. T. (1991). "An assessment of chamber size effects in the calibration of in situ tests in sand." *Geotechnique*, 41(3), 437-445.

Sheorey, P. R., Loui, J. P., Singh, K. B., and Singh, S. K. (2000). "Ground subsidence observations and a modified influence function method for complete subsidence prediction." *International Journal of Rock Mechanics and Mining Sciences*, 37(5), 801-818.

Shimizu, I. (1995). "Kinetics of pressure solution creep in quartz - theoretical considerations." *Tectonophysics*, 245(3-4), 121-134.

Shin, H., and Santamarina, J. C. (2009). "Mineral Dissolution and the Evolution of $k_0$." *Journal of Geotechnical & Geoenvironmental Engineering*, 135(8), 1141-1147.

Shin, H., Santamarina, J. C., and Cartwright, J. A. (2008). "Contraction-driven shear failure in compacting uncemented sediments." *Geology*, 36(12), 931-934.

Shin, H., Santamarina, J. C., and Cartwright, J. A. (2010). "Displacement field in contraction-driven faults." *J. Geophys. Res.-Solid Earth*, 115.

Sibson, R. H. (1986). "Earthquakes and rock deformation in crustal fault zones." *Annual Review of Earth and Planetary Sciences*, 14(1), 149-175.

Skempton, A. W., and Vaughan, P. R. (1993). "The failure of Carsington dam." *Geotechnique*, 43(1), 151-173.

Skinner, A. E. (1969). "A note on influence of interparticle friction on shearing strength of a ramdom assembly of spherical particles." *Geotechnique*, 19(1), 150-177.

Song, C. W., Yu, G. M., and Xue, B. F. "A Huge Source of Pollution Hazard - Disaster and Cure of Tailings Pond." *Proc., 2011 International Conference on Electronics, Communications and Control*, New York, IEEE, 3486-3489.

Sprunt, E. S., and Nur, A. (1977). "Destruction of porosity through pressure solution." *Geophysics*, 42(4), 726-741.

Stumm, W., and Morgan, J. J. (1996). *Aquatic chemistry : chemical equilibria and rates in natural waters*, Wiley, New York, 1022.

Suiker, A. S. J., and Fleck, N. A. (2004). "Frictional Collapse of Granular Assemblies." *Journal of Applied Mechanics*, 71(3), 350-358.

Sultan, N., Cochonat, P., Canals, M., Cattaneo, A., Dennielou, B., Haflidason, H., Laberg, J. S., Long, D., Mienert, J., Trincardi, F., Urgeles, R., Vorren, T. O., and Wilson, C. (2004a). "Triggering mechanisms of slope instability processes and sediment failures on continental margins: a geotechnical approach." *Marine Geology*, 213(1-4), 291-321.

Sultan, N., Cochonat, P., Foucher, J. P., and Mienert, J. (2004b). "Effect of gas hydrates melting on seafloor slope instability." *Marine Geology*, 213(1-4), 379-401.

Tada, R., and Siever, R. (1989). "Pressure Solution During Diagenesis." *Annual Review of Earth and Planetary Sciences*, 17(1), 89-118.

Terzaghi, K. (1943). *Theoretical soil mechanics*, John Wiley & Sons, New York, 510 pages.

Thomas, P. A., and Bray, J. D. (1999). "Capturing Nonspherical Shape of Granular Media with Disk Clusters." *Journal of Geotechnical and Geoenvironmental Engineering*, 125(3), 169-178.

Thornton, C. (2000). "Numerical simulations of deviatoric shear deformation of granular media." *Geotechnique*, 50(1), 43-53.

Trivedi, A., and Sud, V. K. (2004). "Collapse behavior of coal ash." *Journal of Geotechnical and Geoenvironmental Engineering*, 130(4), 403-415.

Truong, Q. H., Eom, Y. H., and Lee, J. S. (2010). "Stiffness characteristics of soluble mixtures." *Géotechnique*, 60(4), 293 –297.

Unay, G., Ertunc, A., Bulutlar, E., and Akdogan, E. (1982). "Karstic limestone problem at Kavsak dam site and reservoird area." *Bulletin of Engineering Geology and the Environment*, 25(1), 143-150.

Vanoudheusden, E., Sultan, N., and Cochonat, P. (2004). "Mechanical behaviour of unsaturated marine sediments: experimental and theoretical approaches." *Marine Geology*, 213(1-4), 323-342.

Veni, G., DuChene, H., Crawford, N. C., Groves, C. G., Huppert, G. N., Kastning, E. H., Olson, R., and Wheeler, B. J. (2001). *Living With Karst: A Fragile Foundation*, American Geological Institute 64 pages.

Verruijt, A., and Booker, J. R. (1996). "Surface settlements due to deformation of a tunnel in an elastic half plane." *Geotechnique*, 46(4), 753-756.

Vogt, P. R., and Jung, W. Y. (2002). "Holocene mass wasting on upper non-Polar continental slopes - due to post-Glacial ocean warming and hydrate dissociation?" *Geophys. Res. Lett.*, 29(15).

Vorster, T. E. B., Klar, A., Soga, K., and Mair, R. J. (2005). "Estimating the effects of tunneling on existing pipelines." *Journal of Geotechnical and Geoenvironmental Engineering*, 131(11), 1399-1410.

Waltham, T. (2009). *Foundations of Engineering Geology*, Spon Press, 98.

Waltham, T., Bell, F., and Culshaw, M. (2005). *Sinkholes and Subsidence: Karst and Cavernous Rocks in Engineering and Construction*, Springer, Chichester, UK, 382

Waltham, T., Park, H. D., Suh, J., Yu, M. H., Kwon, H. H., and Bang, K. M. (2011). "Collapses of old mines in Korea." *Engineering Geology*, 118(1-2), 29-36.

Wang, Y., Shi, J. W., and Ng, C. W. W. (2011). "Numerical modeling of tunneling effect on buried pipelines." *Canadian Geotechnical Journal*, 48(7), 1125-1137.

Watson, M. N. (2004). "Carbon dioxide and carbonate cements in the Otway Basin: Implications for geological storage of carbon dioxide." *APPEA Journal*, 44, 703-720.

Xie, S., Qi, L., and Zhou, D. (2004). "Investigation of the effects of acid rain on the deterioration of cement concrete using accelerated tests established in laboratory." *Atmospheric Environment*, 38(27), 4457-4466.

Yasuhara, H., Marone, C., and Elsworth, D. (2005). "Fault zone restrengthening and frictional healing: The role of pressure solution." *J. Geophys. Res.-Solid Earth*, 110(B6).

Yoo, C., and Kim, J.-H. (2003). "A web-based tunneling-induced building/utility damage assessment system: TURISK." *Tunn. Undergr. Space Technol.*, 18(5), 497-511.

Zhu, C., and Lu, P. (2009). "Alkali feldspar dissolution and secondary mineral precipitation in batch systems: 3. Saturation states of product minerals and reaction paths." *Geochimica et Cosmochimica Acta*, 73(11), 3171-3200.

# VITA

## MINSU CHA

Minsu Cha was born on April 30, 1978 in Yangsan, Korea. He received his Bachelor's of Science degree in Civil Engineering from Pusan National University, Korea in February 2004, his Master's of Science degree in Civil Engineering from KAIST, Daejeon, Korea in February 2006. In August 2008, he started research towards this doctoral dissertation at the Georgia Institute of Technology, and will receive his Ph.D. degree in Civil Engineering (Geosystems Engineering Group) in December 2012.